Ben-Gurion University of the Negev
Engineering Faculty
Mechanical Engineering Department

Anisotropization of Quasi-Static Magnetohydrodynamic Turbulence under the Action of a Static Magnetic Field

THESIS SUBMITTED IN PARTIAL FULFILLMENT
OF THE REQUIREMENTS FOR THE DEGREE OF
"DOCTOR OF PHILOSOPHY"

by

Eli Barami

Submitted to the senate of Ben-Gurion university of the Negev

October 2021

Ben-Gurion University of the Negev
Engineering Faculty
Mechanical Engineering Department

Anisotropization of Quasi-Static Magnetohydrodynamic Turbulence under the Action of a Static Magnetic Field

THESIS SUBMITTED IN PARTIAL FULFILLMENT
OF THE REQUIREMENTS FOR THE DEGREE OF
"DOCTOR OF PHILOSOPHY"

by

Eli Barami

Submitted to the senate of Ben-Gurion university of the Negev

Approved by the advisors

October 2021

This work was carried out under the supervision of

Prof. Semion Sukoriansky, Dr. Yuri Feldman and Dr. Efi Zemach

In the Department of Mechanical Engineering

Faculty of Engineering Sciences.

Prof. Semion Sukoriansky

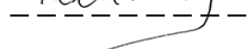

Dr. Yuri Feldman

Dr. Efi Zemach

I Eli Barami, whose signature appears below, hereby declare that:

- I have written this Thesis by myself, except for the help and guidance offered by my thesis advisors.
- The scientific materials included in this thesis are products of my own research, culled from the period during which I was a research student.

Date: 10.10.2021

Student's name: Eli Barami

Signature: 

Acknowledgements

First and foremost, I would like to express my sincere gratitude and appreciation to my supervisor Prof. Sukoriansky Semion for his guidance, support, encouragement, and patience over the years. His guidance helped me with my research, including the writing of this thesis. Semion, thank you so much about being me a teacher. Second, I would like to thank my supervisors, Dr. Feldman Yuri and Dr. Zemach Efi, for the help with the numerical and computational guidance, fruitful discussions, and encouragement over the years.

Finally, I would like to thank my family who supported me over the years and, especially, my dear wife for unlimited support and love throughout this research.

Abstract

Magnetohydrodynamic (MHD) flows of liquid metals are used in many industrial applications. Typically, in such systems, a strong external magnetic field affects the flow, modifies the turbulent properties, and causes flow anisotropization. Flows of this type are not only essential for different engineering applications but also provide an appealing framework for studies of quasi-two-dimensional turbulence with strongly modified transport properties.

Although this subject has been studied extensively for more than a half-century, understanding the phenomenon is far from being completed. Recently, a novel description of quasi-static MHD turbulence was developed for small interaction parameters by application of the quasi-normal scale elimination (QNSE) theory (Sukoriansky and Zemach, 2016).

In this work, we studied the anisotropization of homogeneous MHD turbulence at low magnetic Reynolds numbers using large-scale forced, high-resolution direct numerical simulations (DNSs) with up to 1024^3 grid points. The DNS results are compared with those obtained with the QNSE theory. The simulations validated the theoretical predictions for a weak magnetic field, including the generation of the $k^{-7/3}$ range of the energy spectra and its propagation toward higher wavenumbers with increasing magnetic field strength.

In a strong magnetic field, the turbulence attains a quasi-two-dimensional state with an enstrophy cascade inertial range of the normal flow components in the normal plane and a passive scalar inertial-convective range of the parallel component. The corresponding energy spectra are in good agreement with Kraichnan's logarithmically corrected k^{-3} and k^{-1} theoretical predictions. Furthermore, analysis

of the skewness of the longitudinal velocity derivative and second and third-order longitudinal velocity structure functions for the normal plane components indicate that the turbulence attains a quasi-2D state.

With increasing Reynolds number at constant magnetic field, the enstrophy cascade becomes unstable and is replaced by helicity cascade with $k^{-7/3}$ energy spectrum. The enstrophy cascade is restored with an increasing magnetic field strength.

An investigation of the energy injection mechanism into the parallel component in a strong magnetic field revealed that the energy is supplied directly by an external force. The spectrum of the parallel component depends on the isotropy of external forcing and is, thus, not universal.

Table of Contents

List of Figures

List of Tables

Chapter 1

Introduction

Turbulent flows in the atmosphere, in the oceans, and in engineering devices are often affected by external body forces, which render them anisotropic. Buoyancy, the Coriolis force, and the Earth's curvature are the primary factors leading to anisotropization of large-scale atmospheric and oceanic flows and subsequent significant modification of turbulence dynamics. Another important example of anisotropic turbulence is the turbulent flow of an electrically conducting fluid placed in a permanent external magnetic field. In particular, magnetohydrodynamic (MHD) flows of liquid metals are vital for many engineering applications, including liquid metal heat exchangers, MHD pumps, and metallurgy applications. Apart from that, it is well-known that the effect of a strong enough magnetic field on liquid metals causes turbulence two-dimensionalization. Over the last half-century, scientists have conducted experiments with liquid metal flows under a permanent magnetic field to study quasi-two-dimensional turbulence. While these experiments significantly contributed to our knowledge of turbulence anisotropization, analytical and numerical studies of liquid metal MHD turbulence are essential for in-depth understanding of this phenomenon.

Despite the extensive study of liquid metal flows under the impact of a permanent magnetic field, questions related to MHD turbulence, such as: How does the magnetic field affect the transport properties of MHD turbulence? How does the

anisotropization develop with increasing the magnetic field strength, and how does it affect different turbulent scales, remain open. This thesis aims to shed light upon the effect of a permanent magnetic field on turbulence and to answer the questions stated above. For this purpose, high-resolution direct numerical simulations were used.

Additional goal of the current research is to compare the numerical results with those derived analytically. One of the analytical theories, the quasi-normal scale elimination (QNSE) theory was developed recently for study of MHD turbulence with high hydrodynamic and low magnetic Reynolds numbers (Sukoriansky and Zemach, 2016). This theory proposes a novel description of the turbulence anisotropization in the region of weak magnetic fields. The results obtained from the QNSE theory will be compared with those from the simulations.

This chapter aims to give a concise description and the governing equations of MHD turbulence and specifically of the quasi-static MHD approximation typical for liquid metal flows. In addition, a literature review of quasi-static MHD is presented. Finally, the QNSE theory and its results are briefly described.

1.1 Quasi two-dimensional turbulence

Quasi two-dimensional turbulence is one of the strongly anisotropic regimes obtained in turbulent flows subjected to external body force. Quasi-static MHD turbulence is one of typical examples of such a regime. Another example is a turbulent flow affected by a strong Coriolis force. The nature of two-dimensional turbulent flow is different from the isotropic three-dimensional one. Its behavior can be explained

using the vorticity equation. For three-dimensional isotropic turbulent flow, the vorticity equation is:

$$\frac{\partial \boldsymbol{\omega}}{\partial t} + \left(\mathrm{u} \cdot \nabla\right)\boldsymbol{\omega} = \left(\boldsymbol{\omega} \cdot \nabla\right)\mathrm{u} + \nu\Delta\boldsymbol{\omega}, \tag{1.1}$$

where u is the velocity field, $\boldsymbol{\omega}$ is the vorticity defined as $\boldsymbol{\omega} = \nabla \times \mathrm{u}$, and ν is the kinematic viscosity. This equation is derived by applying the curl operator to the Navier-Stokes equation. The first term on the right-hand side (RHS) is the vortex stretching, which is a source of the vorticity. In two-dimensional flows, the vorticity and the velocity are orthogonal, $\mathrm{u} \perp \boldsymbol{\omega}$; hence, there is no vortex stretching in such flows, and the viscous term balances the inertia term. Multiplying the above equation by the vorticity, for two-dimensional (2D) flow, one gets:

$$\frac{D\left(\frac{\boldsymbol{\omega}^2}{2}\right)}{Dt} = \nu\left[\nabla\left(\boldsymbol{\omega}\nabla\boldsymbol{\omega}\right) - \left(\nabla\boldsymbol{\omega}\right)^2\right]. \tag{1.2}$$

Averaging the above equation, and considering that the first (divergence) term in the RHS becomes zero due to the boundary conditions, we obtain:

$$\frac{D\Omega}{Dt} = -\nu\left(\nabla\boldsymbol{\omega}\right)^2, \tag{1.3}$$

where $\boldsymbol{\Omega}$ is the enstrophy defined as $\Omega = 1/2\left\langle\boldsymbol{\omega}^2\right\rangle$. Equation (1.3) shows that if there is no external source of enstrophy then the total enstrophy of the system can only decrease with time due to viscose enstrophy dissipation, η_ν. By simple mathematical operations, it can be seen that the rate of the turbulence kinetic energy dissipation linearly depends on the enstrophy:

$$\varepsilon = 2\int \nu k^2 E(k) dk = 2\nu\Omega. \tag{1.4}$$

No assumptions were taken to derive the above relation; therefore, it is valid for both three and two-dimensional flows, and it can be used for qualitative discussion on the differences between three- and two-dimensional turbulent flows. For this purpose, imagine a case of fully developed isotropic three-dimensional turbulent flow with a very high Reynolds number. At the large scales where the energy is injected, the viscosity effect is negligible, but, as follows from conservation of energy, the rate of the turbulent kinetic energy injection is balanced by the rate of dissipation. A short gaze at equation (1.4) shows that for finite dissipation and decreasing viscosity, the balance between the energy input and the dissipation can be sustained only by increasing the enstrophy. The enstrophy increase means vorticity production by the vortex stretching term. In two-dimensional turbulent flow, at large Reynolds number where the viscosity tends to zero, this equation still holds. However, the vortex stretching term vanishes, and no production of vorticity or enstrophy is possible. Therefore, in two-dimensional flows with high Re and very small viscosity, the rate of turbulent kinetic energy dissipation is very small. Consequently, the energy injected at some forcing scale cannot cascade downscale to the dissipation scale rather than go in the opposite direction, i.e., upscale. Thus, two dynamical constraints existing simultaneously in 2D – energy and enstrophy conservations – force the vortices to merge and enlarge, which means that in two-dimensional turbulence the energy flux is transferred in inverse cascade. The inverse energy cascade still dictates the -5/3 spectrum power law, like in isotropic three-dimensional (3D) turbulence, but with the opposite direction of the energy flux. In 2D turbulent flows, the enstrophy is injected by the external force, propagates in a forward cascade to smaller scales, and finally dissipates by viscosity, balancing the input of enstrophy. Unlike in 3D, the energy spectrum in the forward enstrophy

cascade range obeys the -3 spectrum power law (derived by dimensional analysis), as seen in Figure 1.1.

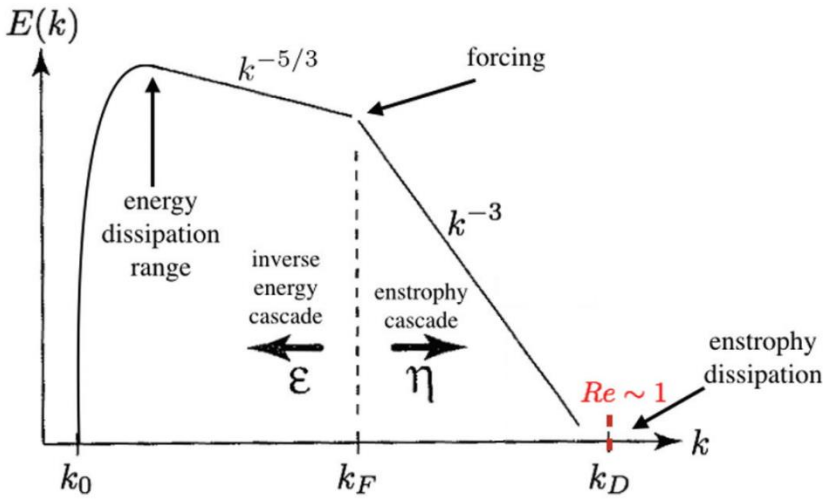

Figure 1.1. Qualitative picture of the double cascade of forced two-dimensional turbulence (reproduced from Fox-Kemper *et al.* (2014)).

1.2 Magnetohydrodynamics

Solar winds, sunspots, the Earth's core motion, and more are phenomena related to magnetohydrodynamics (MHD). MHD is the science that deals with the interaction between electrically conducting fluids and magnetic fields. The word "Magnetohydrodynamics" was first coined in 1942 by H. Alfvén, who related the MHD phenomenon to the transfer of momentum from the sun to the planets. However, there were some earlier works related to MHD, such as the well-known experiment of M. Faraday that tried to measure the voltage across the Thames River by its motion through the earth's magnetic field. He failed, unfortunately, because the current was too small to measure with the equipment at his time. In addition, J. Hartmann invented the first electromagnetic pump that has been in common use until these days (Branover, 1978; Davidson, 2002).

Today, MHD is widely used. For instance, plasma physicists use it to confine plasma and to control thermonuclear fusion reactions, MHD pumps provide circulation of liquid metal for the cooling of nuclear reactors, metallurgists use MHD to control the processes of industrial casting, and more (Blumenau *et al.,* 1986; Bourgoin *et al.,* 2002; Claessens, 2020). Furthermore, the importance of controlling heat and mass transfer in the metallurgical and semiconductor industries yields different methods to generate the required MHD flow by using various magnetic fields, such as static, traveling, and rotating magnetic fields (Dold and Benz, 1999; Barami *et al.,* 2017).

The MHD phenomenon is governed by a set of equations, which are a combination of Maxwell's equations of electromagnetism and the Navier-Stokes equations of fluid dynamics. We first consider Ampère's law. This law relates magnetic fields to electric currents; namely, the presence of an imposed magnetic field induces an electrical current, or the presence of electrical currents induces magnetic fields. Ampère's law states:

$$\mu_0 \mathbf{J} = \nabla \times \mathbf{B}, \tag{1.5}$$

where μ_0 is the magnetic permeability, J is the electrical current density, and B is the magnetic field. For MHD flow, the displacement currents are neglected in applying Ampère's law, due to the high electrical conductivity of the fluids. The divergence of the above equation yields the charge conservation equation:

$$\nabla \cdot \mathbf{J} = 0. \tag{1.6}$$

Faraday's law states that an electric field, E, always accompanies the time varying magnetic field, B:

$$\nabla \times \mathbf{E} = -\frac{\partial \mathbf{B}}{\partial t}. \tag{1.7}$$

Gauss's law for magnetism states that the magnetic field is a solenoidal vector field (magnetic monopoles do not exist). This means that the divergence of the magnetic field B is equal to zero:

$$\nabla \cdot \mathbf{B} = 0. \tag{1.8}$$

Another significant equation to consider in MHD is Ohm's law. In a stationary conductor, the current density, J, is proportional to the electric field $\mathbf{J} = \sigma \mathbf{E}$, where σ is the electrical conductivity. The movement of a conducting fluid in a magnetic field, B induces an extra electrical current, and Ohm's law takes the form:

$$\mathbf{J} = \sigma\left(\mathbf{E} + \mathbf{u} \times \mathbf{B}\right). \tag{1.9}$$

Applying the curl operator to both sides of Ohm's law (1.9) and using Ampère's law (1.5) and Faraday's law (1.7), as well as utilizing the fact that the magnetic field is solenoidal (1.8), we obtain:

$$\frac{\partial \mathbf{B}}{\partial t} = \nabla \times \left(\mathbf{u} \times \mathbf{B}\right) + \frac{1}{\mu_0 \sigma} \nabla^2 \mathbf{B}. \tag{1.10}$$

The above equation is known as the magnetic induction equation. A few different forms of this equation are found in the literature. In this equation, the coupling between the magnetic field, B, and the velocity field, u, is clearly seen. The last key fact related to this coupling is that the Lorentz force acts as a body force on each unit volume:

$$\mathbf{F} = \mathbf{J} \times \mathbf{B}. \tag{1.11}$$

This force is an additional MHD term in the Navier-Stokes equation. The Navier-Stokes equation describes the motion of a fluid due to inertia, pressure gradients, viscous forces, and body forces. The body force acting on a conducting fluid moving

in a magnetic field is the Lorentz force (1.11). Thus, the MHD momentum equation reads:

$$\frac{\partial \mathbf{u}}{\partial t} + \mathbf{u} \cdot \left(\nabla \mathbf{u}\right) = -\frac{1}{\rho}\nabla p + \nu \nabla^2 \mathbf{u} + \frac{1}{\rho}\mathbf{J} \times \mathbf{B}\,, \tag{1.12}$$

where p is the pressure, and ρ is the fluid density. An additional important equation in fluid mechanics is the continuity equation, which expresses the conservation of mass. The continuity equation for incompressible fluid reads:

$$\nabla \cdot \mathbf{u} = 0\,. \tag{1.13}$$

The full MHD problem is governed by the closed set of equations (1.10), (1.12), and (1.13). In general, since these equations are coupled, they need to be solved simultaneously. However, as we will see in the following, the quasi-static approximation enables to decouple the equations.

1.3 Quasi-Static MHD approximation

In the present work, we limit the study to the case of MHD flows of liquid metals. A characteristic feature of liquid metals is their low magnetic Prandtl number, $\mathrm{Pr}_m = \nu_0 / \kappa << 1$, where $\kappa = (\mu_0 \sigma)^{-1}$ is the magnetic diffusivity. Thus, liquid metal flows are typically fully turbulent with large hydrodynamic Reynolds number, and small magnetic Reynolds number, $\mathrm{Re}_m = u_0 l_0 / \kappa$ (where u_0 and l_0 are the characteristic velocity and length scale of the flow). Recalling the induction equation (1.10), by using mathematical identity, the first term on the RHS can be replaced by:

$$\nabla \times \left(\mathbf{u} \times \mathbf{B}\right) = \mathbf{u}\left(\nabla \cdot \mathbf{B}\right) - \mathbf{B}\left(\nabla \cdot \mathbf{u}\right) + \left(\mathbf{B} \cdot \nabla\right)\mathbf{u} - \left(\mathbf{u} \cdot \nabla\right)\mathbf{B}\,. \tag{1.14}$$

From the continuity equation (1.13) and the solenoidality of magnetic fields (1.8), equation (1.14) reduces to:

$$\nabla \times \left(\mathbf{u} \times \mathbf{B} \right) = \left(\mathbf{B} \cdot \nabla \right) \mathbf{u} - \left(\mathbf{u} \cdot \nabla \right) \mathbf{B}, \tag{1.15}$$

substituting this into equation (1.10) yields:

$$\frac{\partial \mathbf{B}}{\partial t} = \left(\mathbf{B} \cdot \nabla \right) \mathbf{u} - \left(\mathbf{u} \cdot \nabla \right) \mathbf{B} + \kappa \nabla^2 \mathbf{B}. \tag{1.16}$$

Note that the magnetic field B can be decomposed into an impose (B_0) and induced (b) magnetic field, $B = B_0 + b$, and substituting it into equation (1.16) yields:

$$\frac{\partial \left(\mathbf{B}_0 + \mathbf{b} \right)}{\partial t} = \left(\left(\mathbf{B}_0 + \mathbf{b} \right) \cdot \nabla \right) \mathbf{u} - \left(\mathbf{u} \cdot \nabla \right) \left(\mathbf{B}_0 + \mathbf{b} \right) + \kappa \nabla^2 \left(\mathbf{B}_0 + \mathbf{b} \right). \tag{1.17}$$

The above equation gets simplified considerably under the assumption of low Re_m, since $|b| << |B_0|$ and B_0 is constant ($\partial_t \mathbf{B}_0, \nabla \mathbf{B}_0 = 0$), equation (1.17) becomes:

$$\frac{\partial \mathbf{b}}{\partial t} = \left(\mathbf{B}_0 \cdot \nabla \right) \mathbf{u} + \kappa \nabla^2 \mathbf{b}. \tag{1.18}$$

Furthermore, since Re_m is defined by the ratio between the time scale for the diffusion of the magnetic field, $\tau_\kappa = l_0^2 / \kappa$, to the eddy turnover time, $\tau_{tu} = l_0 / u_0$, the time derivative term can be neglected. Rewrite equation (1.18) under the above results yields:

$$\kappa \Delta \mathbf{b} = -\left(\mathbf{B}_0 \cdot \nabla \right) \mathbf{u}. \tag{1.19}$$

Under the assumption that the magnetic diffusivity is constant, the induced field can be formally solved:

$$\mathbf{b} = -\frac{1}{\kappa} \Delta^{-1} \left(\mathbf{B}_0 \cdot \nabla \right) \mathbf{u}, \tag{1.20}$$

where Δ^{-1} is the inverse Laplacian operator. Equation (1.19) is the Poisson equation which is used to obtain the induced magnetic field. This approximation is known as the quasi-static approximation for low magnetic Reynolds number. Equation (1.20)

enables the decoupling between the Navier-Stokes and the induction equations, as we will see in the following.

The current density in the Lorentz force, $\mathrm{J}\times\mathrm{B}$, can be eliminated using the Ampère's law (1.5) as follows:

$$\mu_0\left(\mathrm{B}\times\mathrm{J}\right)=\mathrm{B}\times(\nabla\times\mathrm{B})\,. \tag{1.21}$$

The RHS term can be replaced by using the following identity:

$$\mathrm{B}\times(\nabla\times\mathrm{B})=\nabla\left(\mathrm{B}\cdot\mathrm{B}/2\right)-\left(\mathrm{B}\cdot\nabla\right)\mathrm{B}\,, \tag{1.22}$$

and thus, the Lorentz force term in the Navier-Stokes equation becomes:

$$\frac{1}{\rho}\mathrm{J}\times\mathrm{B}=\frac{1}{\mu_0\rho}\left(\left(\mathrm{B}\cdot\nabla\right)\mathrm{B}-\nabla\left(\left|\mathrm{B}\right|^2/2\right)\right), \tag{1.23}$$

and again, since $\mathrm{B}=\mathrm{B}_0+\mathrm{b}$, and $|\mathrm{B}_0|>>|\mathrm{b}|$, and B_0 is constant, the first term in the RHS of the above equation becomes:

$$\left(\left(\mathrm{B}_0+\mathrm{b}\right)\cdot\nabla\right)\left(\mathrm{B}_0+\mathrm{b}\right)=\left(\mathrm{B}_0\cdot\nabla\right)\mathrm{b}\,. \tag{1.24}$$

The second term on the RHS of equation (1.23) has the form of the pressure term in the Navier-Stokes equation. Thus, it can be eliminated by merging it into the pressure gradient term. Substitution of (1.24) into the Navier-Stokes equation (1.12) yields:

$$\frac{\partial\mathrm{u}}{\partial t}+\mathrm{u}\cdot\left(\nabla\mathrm{u}\right)=-\frac{1}{\rho}\nabla p+\nu\nabla^2\mathrm{u}+\frac{1}{\rho\mu_0}\left(\mathrm{B}_0\cdot\nabla\right)\mathrm{b}\,. \tag{1.25}$$

Substituting the equation of the induction field (1.19) into the above equation, we obtain:

$$\frac{\partial\mathrm{u}}{\partial t}+\mathrm{u}\cdot\left(\nabla\mathrm{u}\right)=-\frac{1}{\rho}\nabla p+\nu\nabla^2\mathrm{u}-\frac{1}{\rho\mu_0}\left(\mathrm{B}_0\cdot\nabla\right)\frac{1}{\kappa}\Delta^{-1}\left(\mathrm{B}_0\cdot\nabla\right)\mathrm{u}\,. \tag{1.26}$$

In our study, we consider a constant imposed magnetic field in the *z*-direction, $\mathrm{B}_0 = B_0\hat{z}$. Thus, the above equation is simplified to:

$$\frac{\partial \mathrm{u}}{\partial t} + \mathrm{u}\cdot\left(\nabla \mathrm{u}\right) = -\frac{1}{\rho}\nabla p + \nu\nabla^2 \mathrm{u} - \frac{\sigma B_0^{\,2}}{\rho}\Delta^{-1}\frac{\partial^2 \mathrm{u}}{\partial z^2}. \qquad (1.27)$$

The above equation governs the MHD phenomenon under the assumption of small Re_m. The ensuing approximation is known as quasi-static (QS)-MHD (Roberts, 1967; Alemany *et al.,* 1979). The "new" term in the RHS of the above equation is the magnetic friction, also known in the literature as the anisotropic ohmic (Joule) dissipation, with a characteristic dissipation time $\tau_J = \rho / \left(\sigma B_0^{\,2}\right)$.

When a sufficiently strong magnetic field is applied, the turbulence becomes anisotropic and tends to become two-dimensional (in the plane perpendicular to the field) due to Joule damping. Nonlinear interactions disrupt this process by transferring energy between the Fourier modes in an attempt to restore isotropy. The parameter governing this process is the interaction parameter, $N_0 = \tau_{tu} / \tau_J$, which characterizes the relative strengths between the Joule dissipation and the nonlinear effects. The effect of the Joule dissipation term on the velocity fluctuations can be clearly seen in Fourier space, where the diffusion coefficient in front of this term converts to $1/(\tau_J k^2)$. Thus, while τ_J is scale independent, the dissipation strength decreases with decreasing scales. The relative strength of the Joule dissipation at any given Fourier mode is characterized by the scale-dependent interaction parameter $N(k) = \tau_{tu}(k) / \tau_J$. The turnover time of a mode *k*, $\tau_{tu}(k)$, can be computed using the kinetic energy spectrum $E(k)$, as $\tau_{tu}(k) = 1/\sqrt{k^3 E(k)}$, which shows that, for a spectrum shallower than k^{-3}, $N(k)$ decreases with increasing *k*. It is reasonable to expect that scales with $N(k) > 1$ are strongly affected by the magnetic

field, while those with $N(k) < 1$ are weakly affected and remain nearly isotropic. A transitional wavenumber k_{tr} that separates these domains is located in a region where $N(k) \approx 1$. It has been shown experimentally that in strong magnetic fields the spectrum of liquid metal MHD turbulence scales as k^{-3} at wavenumbers larger than the forcing wavenumber (Kolesnikov and Tsinober, 1972; Kolesnikov and Tsinober, 1974; Alemany *et al.,* 1979). On these scales, the local interaction parameter is constant, and thus a transitional wavenumber would not exist. Nonetheless, several open questions remain: Is there a transitional wavenumber at weak fields, and how does it depend on the magnetic field strength? Can the Kolmogorov $k^{-5/3}$ spectrum at $k > k_{tr}$ coexist with a steeper MHD spectrum at smaller wavenumbers? What would be the spectral power of such a spectrum? The answers to these questions are given by the QNSE analyses of QS-MHD turbulence (Sukoriansky and Zemach, 2016), as detailed in section 1.5.

1.4 Literature review – Quasi-Static MHD

In the past few decades, a great deal of effort has been invested in studying the effect of a permanent magnetic field on QS-MHD turbulence. It has been found experimentally that if the magnetic field is sufficiently strong, the wall friction and the drop in the channel flow pressure approach the laminar limit, while the velocity fluctuations in the direction normal to the field remain strong (Kit and Tsinober, 1971; Kolesnikov and Tsinober, 1974; Branover, 1978; Branover and Gershon, 1979). These phenomena – together with the experimentally observed increase of the velocity correlation length in the direction of the field (Votsish and Kolesnikov, 1976), the suppression of vortices with axes perpendicular to the field, and the

stabilization of vortices with axes parallel to the field (Sukoriansky and Branover, 1985) – indicate the tendency of liquid metal turbulence to attain a quasi-two-dimensional (2D) state under the action of a permanent magnetic field (Kit and Tsinober, 1971; Kolesnikov and Tsinober, 1974; Sommeria and Moreau, 1982; Caperan and Alemany, 1985; Sukoriansky *et al.,* 1986). Liquid metal MHD flows (which can be replicated under controllable laboratory experiments) provide a convenient framework for studies of quasi-2D turbulence with anisotropic transport properties (Branover *et al.,* 1986; Sukoriansky *et al.,* 1986; Sukoriansky *et al.,* 1989) and of the mechanism of transition from an isotropic three-dimensional (3D) state to a quasi-2D state. The peculiar features of anisotropic turbulence, such as an inverse energy cascade typical of forced 2D turbulence (Kraichnan, 1967), have been observed experimentally (Sommeria, 1986).

The lack of transparency of liquid metals precludes the use of laboratory measurements for obtaining a complete description of the turbulent field in these media. Direct numerical simulation (DNS) is therefore applied to close the knowledge gap. Major experimental findings have been replicated and confirmed by DNS, among them the tendency of QS-MHD turbulence to attain a quasi-2D state in sufficiently strong magnetic fields (Zikanov and Thess, 1998; Burattini *et al.,* 2008a; Favier *et al.,* 2010; Reddy *et al.,* 2014; Reddy and Verma, 2014). Moreover, DNS can provide comprehensive description of the turbulent field and its modification under the impact of a magnetic field. For example, the simulations by Zikanov *et al*. (2019) replicated all the complicated conditions of the laboratory experiment of Sukoriansky *et al*. (1986), thereby throwing light on the mechanisms leading to the anomalous high-amplitude velocity fluctuations detected in the experiment. The simulation results were in good qualitative agreement with the experimental data,

and the computed spatial structure and statistical properties of the flow did indeed provide an explanation for the experimental observations.

Although MHD flows at low Re_m have been studied extensively, most numerical studies to date were limited to high interaction parameters and turbulence two-dimensionalization. Several investigations did, however, consider the range of weak to moderate magnetic fields, and three of these studies are reviewed in brief. Zikanov and Thess (1998) studied the effect of a permanent magnetic field over a wide range of interaction parameters at relatively low resolution (up to 128^3 grid points). Steady state was achieved by keeping the energy of Fourier modes with $k < 2.5$ at a constant level. At high interaction parameters, $N_0 >> 1$, the kinetic energy spectrum approached k^{-3} scaling typical of 2D turbulence. At an intermediate interaction parameter, $N_0 = 0.4$, computed with a lower resolution of 64^3 grid points, the system exhibited intermittent behavior, characterized by long periods of quasi-2D dynamics, interrupted by erratic bursts of 3D turbulence. This strongly intermittent behavior was not fully understood, but it was thought that the low computational resolution or the specific way of maintaining a statistically steady state might have played a considerable role. Thus, according to Zikanov and Thess (1998), the turbulence behavior at moderate interaction parameters was well worth further detailed investigation. Reddy (2015) performed DNS in a periodic box with a resolution of up to 512^3 grid points. His simulations performed with 256^3 grid points showed steepening of the energy spectrum as the interaction parameter increased. For $N_0 = 1.7$ and $N_0 = 5.5$, power laws of -3.2 and -3.8, respectively, were observed. These simulations indicated that – unlike in 2D turbulence – vertical structures developed. The field became two-dimensional at larger values of the interaction parameters, $11 \leq N_0 \leq 18$, with most of the energy being concentrated in the horizontal

(perpendicular to the magnetic field) components of the velocity. With a further increasing field, the spectral power continued to decrease, and for a very large interaction parameter, $N_0 = 130$, exponential behavior was observed. Reddy (2015) reported that at such a magnetic field the magnitudes of the horizontal and vertical flow components were comparable, and the flow behaved as 2D three-componential (2D-3C) turbulence as found by Favier *et al*. (2010). Burattini *et al*. (2008a) studied the anisotropy induced by a magnetic field. They performed DNS in a periodic box with a low-resolution of 256^3 grid points and examined the traditional 3D and the longitudinal 1D energy spectra. The 3D spectrum of the velocity component parallel to the field was found to be more energetic than that of the perpendicular component, similarly to the findings reported in (Favier *et al.,* 2010; Reddy and Verma, 2014), while the longitudinal 1D spectrum of the parallel component was attenuated at all scales.

Notwithstanding extensive experimental and numerical studies, fundamental questions related to the anisotropization of QS-MHD turbulence remain: How does an external uniform magnetic field modify the transport properties of MHD turbulence with small Re_m? How does the anisotropization of different turbulent scales develop? What are the criteria for transition to quasi-2D dynamics? Analytical theories supported and complemented by DNS are needed to answer these questions. This is precisely the purpose of the present work, i.e., verification of the analytical predictions obtained using the QNSE theory (Sukoriansky and Zemach, 2016) with those of high-resolution DNS, extension of the DNS into the high interaction parameter region not covered by the theory, and computation of turbulence parameters not derived from the QNSE theory. The theoretical underpinnings of the QNSE theory and the QNSE results as applied to QS-MHD will be briefly explained

in the next section. Immediately below we present a brief account of analytical results obtained using other theories.

A relatively simple approach to studying the development of anisotropy is to consider initially isotropic turbulence suddenly subjected to a uniform magnetic field and to neglect the viscous and nonlinear terms in the flow equations. This theory, known as the rapid distortion theory (RDT) (Hunt, 1992; Cambon, 1993; Sagaut and Cambon, 2008), gives a qualitative picture of the initial stage of the turbulence reorganization. The Fourier modes located close to the axis parallel to the magnetic field (the so-called Joule cone) are damped most rapidly, and thus this part of the cone becomes depleted of energy first. As time progresses, energy removal affects modes at increasing angles, leading to an energy flux in the angular direction from the region outside the cone towards the cone axis (Moreau and Alemany, 1976; Knaepen and Moreau, 2008). A linear mechanism controls the evolution of turbulence over short times, but for longer times, nonlinearity has a cumulative effect that modifies the evolution of turbulence beyond a linear response.

The drawback of the RDT is that it has only limited predictive skills. More accurate theories describe nonlinear interactions explicitly, using a spectral approach and certain closure hypotheses. One of these closures, the eddy damped quasi-normal Markovian (EDQNM) theory (Orszag, 1977), has been applied to MHD turbulence (Cambon, 1993; Cambon and Godeferd, 1994; Favier *et al.,* 2011). The basic closure assumption of this theory is that the fourth-order spectral moments appearing in the equations for the third-order moments can be approximated as if the velocity fluctuations were Gaussian. The theory predicts transition from 3D turbulent flow to a 'two-and-a-half-dimensional' flow (Montgomery and Turner, 1982) as a result of the combined effects of a short-term linear Joule dissipation and a longer-term

nonlinear creation of polarization anisotropy. The transition is characterized by the elongation of turbulent structures along the applied magnetic field and by strong anisotropization of the directional two-point correlation spectra.

The QNSE theory complements the EDQNM approach, as it allows for the calculation of eddy viscosities and eddy diffusivities, while the EDQNM computations yield energy transfers. The QNSE theory offers a novel description of QS-MHD turbulence (Sukoriansky and Zemach, 2016), and although it was developed for weak magnetic fields, it can be extended to moderate fields beyond its small interaction parameter limit. One of the main goals of the present work is to examine the QNSE theory and to determine at which magnetic fields it is still valid by comparing the energy spectra predicted by the QNSE theory to those obtained by DNS. High-resolution DNS with up to 1024^3 grid points was employed to study the transition from isotropic to anisotropic turbulence at weak, moderate, and strong magnetic fields. The QNSE theory predicts that with increasing the magnetic field strength, the range of scales affected by the field will extend to smaller scales, but to clearly see the field effect at large Re, higher resolution is needed. For this reason, instead of going to very high, computationally prohibited resolutions, we chose to extend the inertial range of the turbulence by utilizing analytically derived two-parametric subgrid-scale parameterization (Kraichnan, 1976b), as will be discussed in the next chapter.

1.5 The QNSE theory for QS-MHD

1.5.1 A brief description of the QNSE theory

A detailed derivation of the QNSE equations has been given in previous studies (Sukoriansky *et al.,* 2005; Sukoriansky and Zemach, 2016; Sukoriansky and Galperin, 2016), and only a summary is presented here. The governing equations are space-time Fourier transformed. They are strongly nonlinear, as the Reynolds number is large on large scales. However, on small scales, near the dissipation cut-off, viscous processes prevail, and Re = $O(1)$. The smallness of the Re facilitates the exploration of a renormalized perturbation methodology by employing 'dressed' eddy viscosity and eddy diffusivity rather than their 'bare' molecular values (McComb, 1990; McComb, 1995). This methodology allows one to gradually coarse-grain the flow domain by recursive elimination of small shells of small-scale modes and to calculate compensating corrections to the effective eddy viscosity and eddy diffusivity, thereby accounting for turbulent transport on the eliminated scales. Technically, this approach follows the renormalization group (RNG) procedure of successive scale elimination (Yakhot and Orszag, 1986) but differs from it in some important details. Unlike RNG, the QNSE procedure (i) does not employ fixed-point arguments, and (ii) uses a self-substitution method (Sukoriansky *et al.,* 2003) to evaluate the product of slow and fast modes, i.e., the "cross-term," in the expansion series. Without going into detail, we present some of the most relevant cornerstones of the QNSE theory as applied to anisotropic turbulent flows affected by an external body force.

By applying the continuity equation, the pressure term may be eliminated from the space-time Fourier transformed momentum equation to give:

$$u_\alpha(\hat{k}) = G_{\alpha\beta}(\hat{k})\left[-\frac{i}{2} P_{\beta\gamma\sigma}(\mathrm{k}) \int u_\gamma(\hat{q}) u_\sigma(\hat{k}-\hat{q}) \frac{d\hat{q}}{(2\pi)^4} \right], \tag{1.28}$$

where $u_\alpha(\hat{k})$ is the Fourier transformed velocity; $\hat{k} = (\mathrm{k}, \omega)$ is a four-dimensional vector in Fourier wavenumber-frequency space, and

$$P_{\alpha\beta\gamma}(\mathrm{k}) = k_\beta P_{\alpha\gamma}(\mathrm{k}) + k_\gamma P_{\alpha\beta}(\mathrm{k}), \tag{1.29}$$

where

$$P_{\alpha\beta}(\mathrm{k}) = \delta_{\alpha\beta} - k_\alpha k_\beta \, / \, k^2 \tag{1.30}$$

is the operator that projects any vector on the plane normal to k; and $G_{\alpha\beta}(\hat{k})$ is the Green function containing all linear terms, including those caused by the external body force. At the start of the scale elimination process, the viscosity in the Green function is isotropic. It becomes anisotropic, acting differently on different velocity components and in different directions, when some of the turbulent scales are eliminated.

Equation (1.28) has the form of a Langevin equation with the stochastic forcing determined by the convolution integral in (1.28):

$$u_\alpha(\hat{k}) = G_{\alpha\beta}(\hat{k}) f_\beta(\hat{k}) . \tag{1.31}$$

Mapping of the small shell of velocity modes $\Delta\Lambda$, which is subject to elimination, to the Langevin equation is an important element of the QNSE procedure. Physically, the Langevin equation represents the balance between nonlinear steering of a given mode by all other modes and damping by the renormalized viscosities. Numerous attempts to derive the stirring force $f_\beta(\hat{k})$ from first principles have so far been unsuccessful (McComb, 1990; Canuto and Dubovikov, 1996), but some of its properties follow readily from the conditions of a stochastic steady state, and flow

incompressibility and homogeneity. An important requirement for the force is that $\left\langle f_\alpha(\mathrm{p}) f_\beta(\mathrm{q}) f_\gamma(\mathrm{k}-\mathrm{p}-\mathrm{q})\right\rangle = 0$ for vector triads such that p, q, and k—p—q belong in the shell $\Delta\Lambda$ subject to elimination, where Λ is the effective dissipation wave number. This property alone suffices to develop a rigorous self-contained mathematical procedure for successive averaging. The force does not have to be Gaussian, although a Gaussian field would meet the above requirement. Generally, $f_\beta(\hat{k})$ may be characterized as quasi-normal. The combination of the quasi-normal forcing and eddy damping represented by the eddy viscosities and eddy diffusivities places the QNSE theory in the class of quasi-normal eddy-damped theories of turbulence.

Scale elimination is achieved by ensemble averaging over the modes in the shell $\Delta\Lambda$, yielding a small, $O(\Delta\Lambda)$, correction to the viscosity. Along with the increase of the effective viscosity, the effective dissipation wave number, Λ, decreases. Hence, the effective Re built upon the scales pertinent to the new value of Λ is again $O(1)$, and the procedure can be repeated. At any step of the scale elimination, the correction to the inverse Green function is given by the following integral:

$$\Delta G^{-1}_{\alpha\beta}(\hat{k}) = P_{\alpha\gamma\delta}(\mathrm{k})\int^{>} P_{\lambda\mu\beta}(\mathrm{k}-\mathrm{q}) U_{\gamma\mu}(\Omega,\mathrm{q}) G_{\delta\lambda}(\omega-\Omega)\frac{d\hat{q}}{(2\pi)^4}, \qquad (1.32)$$

where $\int^{>} d\hat{q} = \int_{\Delta\Lambda} d^3q \int_{-\infty}^{\infty} d\Omega$. The integral contains the velocity correlation tensor $U_{\gamma\mu}(\Omega,\mathrm{q})$, which can be evaluated using the Langevin equation (1.31) and the energy balance equation, which determines the forcing amplitude. Taking the limit $\Delta\Lambda \to 0$, we obtain a differential equation, relating the effective viscosity to the current value of the "moving dissipation cut-off" Λ.

The concept of viscosity implies a spectral gap between the eliminated scales, $k > \Lambda$, and resolvable (explicit) scales, $k < \Lambda$, but such a gap does not appear in the

process of scale elimination. As a result, the effect of the eliminated scales on the explicit scales in the vicinity of the dissipation cutoff Λ differs from that away from it. Kraichnan (1976) has shown that to obtain an adequate description of the physics, the dependence of the eddy viscosity on both the local explicit wavenumber k and the dissipation cutoff Λ must be taken into account. This two-parametric viscosity is denoted by $\nu(k \mid \Lambda)$. The QNSE theory employs an important simplification, known as the distant interaction or spectral gap approximation, in which the limit $k / \Lambda \to 0$ is taken, and only the terms up to $O(k^2)$ are retained. Essentially, this approximation enforces a spectral gap between the resolvable and eliminated scales, and accordingly renormalized viscosities and diffusivities are taken only as functions of Λ. Although this approach introduces a certain inaccuracy, it gives reliable subgrid scale parameterization in 3D flows featuring a direct energy cascade. The distant interaction approximation is problematic for flows with an inverse energy cascade because the eddy viscosity $\nu(k \mid \Lambda)$ becomes negative at $k \to 0$ (Kraichnan, 1976). This problem arises in MHD flow, which, under the action of a strong magnetic field, becomes quasi-2D with an inverse energy cascade. Thus, the scale-elimination procedure can be used only for a weak magnetic field or on scales where the effect of Joule dissipation is weak. We give additional details on the two-parametric viscosity and its use in DNS in the following chapter.

The QNSE methodology has been applied to various turbulent flows, such as isotropic homogeneous turbulence with no extra strains (Sukoriansky *et al.,* 2003), and to stably stratified (Sukoriansky *et al.,* 2005), rotating (Sukoriansky and Galperin, 2016) and QS-MHD flows (Sukoriansky and Zemach, 2016). The QNSE apparatus for dealing with all these cases is similar, but the form of the Green function differs significantly. The theory provides analytical expressions for the scale-

dependent eddy viscosities and eddy diffusivities in the directions parallel and normal to the external magnetic field. Other turbulence properties, such as 1D and 3D energy spectra, are also analytically derived, thereby shedding light on the modification of the Kolmogorov $k^{-5/3}$ spectrum by anisotropic Joule dissipation. In particular, it is shown that a weak magnetic field generates $k^{-7/3}$ corrections to all 1D spectra. Some details of the QNSE results are given directly below.

1.5.2 Results of the QNSE analyses for quasi-static MHD

In the process of scale elimination, there emerge two types of anisotropization—directional and componential. The Green function $G_{\alpha\beta}(\hat{k})$ becomes an anisotropic tensor that contains renormalized (effective) viscosities. For the horizontal (perpendicular to B) velocity components, the effective viscosities in the horizontal and the vertical (parallel to B) directions are, respectively, ν_h and ν_z. For the vertical velocity component u_3, the effective viscosities are ν_{3h} and ν_{3z}.

$$G_{\alpha\beta}(\hat{k}) = g(\hat{k})[\delta_{\alpha\beta} + A(\hat{k})P_{3\alpha}(\mathbf{k})P_{3\beta}(\mathbf{k})], \tag{1.33}$$

where

$$A(\hat{k}) = \frac{(\nu_z - \nu_{3z})k^2}{g^{-1}(\hat{k}) - (\nu_z - \nu_{3z})k^2 P_{33}(\mathbf{k})}, \tag{1.34}$$

and the inverse auxiliary Green function $g^{-1}(\hat{k})$ is:

$$g^{-1}(\hat{k}) = -\mathrm{i}\omega^2 + \nu_h(k_1^2 + k_2^2) + \nu_z k_3^2 + \frac{\sigma {B_0}^2}{\rho}\frac{k_3^2}{k^2}. \tag{1.35}$$

It is convenient to present the scale-dependent eddy viscosities in a non-dimensional form by dividing the QNSE results by the corresponding value of the eddy viscosity in the non-magnetic case,

$$\nu_n(k) \approx 0.5\varepsilon^{1/3}k^{-2/3}, \tag{1.36}$$

where ε is the viscous energy dissipation rate. It has previously been shown (Sukoriansky and Zemach, 2016) that $\nu_{3z} = \nu_{3h} \equiv \nu_3$. Other scale-dependent eddy viscosities are:

$$\begin{aligned}
\frac{\nu_h(k)}{\nu_n(k)} &= 1 - 0.695\left(\frac{k_J}{k}\right)^{2/3} \\
\frac{\nu_z(k)}{\nu_n(k)} &= 1 - 0.666\left(\frac{k_J}{k}\right)^{2/3} \\
\frac{\nu_3(k)}{\nu_n(k)} &= 1 - 0.106\left(\frac{k_J}{k}\right)^{2/3},
\end{aligned} \tag{1.37}$$

where $k_J = 1/\sqrt{\tau_J^3\varepsilon}$ is the wavenumber at which the Joule dissipation time is comparable with the eddy turnover time.

With the eddy viscosities known (1.37), the derivation of the renormalized Green function is completed and can be used for computation of velocity correlator and kinetic energy spectra. According to the QNSE results, the 3D energy spectrum in a weak magnetic field is:

$$E(k) = C_K\varepsilon^{2/3}k^{-5/3}[1 + 0.97(k/k_J)^{-2/3}], \tag{1.38}$$

where $C_K \approx 1.6$ is the Kolmogorov constant. Thus, the first-order correction to the Kolmogorov spectrum is proportional to $k^{-7/3}$. The next-order correction, which becomes dominant at a stronger magnetic field, is proportional to k^{-3}. The magnetic field causes turbulence anisotropization, but the 3D spectrum provides only limited information on the magnetic field effect. A better description of the anisotropy is given by the one-dimensional (1D) longitudinal and transverse energy spectra. In a weak magnetic field, the 1D spectra obtained from the QNSE are (Sukoriansky and Zemach, 2016):

$$
\begin{aligned}
E_1(k_1) &= \frac{18}{55} C_K \varepsilon^{2/3} k_1^{-5/3} [1 + 0.66(k_1 / k_J)^{-2/3}] \\
E_1(k_2) &= \frac{24}{55} C_K \varepsilon^{2/3} k_2^{-5/3} [1 + 0.99(k_2 / k_J)^{-2/3}] \\
E_1(k_3) &= \frac{24}{55} C_K \varepsilon^{2/3} k_3^{-5/3} [1 + 0.41(k_3 / k_J)^{-2/3}] \\
E_3(k_1) &= \frac{24}{55} C_K \varepsilon^{2/3} k_1^{-5/3} [1 + 0.8(k_1 / k_J)^{-2/3}] \\
E_3(k_3) &= \frac{18}{55} C_K \varepsilon^{2/3} k_3^{-5/3} [1 + 0.43(k_3 / k_J)^{-2/3}],
\end{aligned}
\tag{1.39}
$$

where $E_i(k_j)$ is the 1D spectrum of the velocity component u_i as a function of k_j. A simple way to estimate the transitional wavenumber is to equate the Kolmogorov part of the spectrum with the MHD-induced $k^{-7/3}$ part. The result varies from $k_{tr} \approx k_J$ to $k_{tr} \approx 3k_J$, depending on the particular 3D or 1D spectrum used for this purpose. Both k_J and k_{tr} are proportional to $B_0^3 \varepsilon^{-1/2}$. These analytical predictions were compared with the DNS results, as detailed in the results chapter.

Chapter 2

The Numerical Code

In this chapter, a detailed description of the numerical code is given. It includes the QS-MHD equation solved within the code, the temporal and spatial numerical methods used to solve the QS-MHD equation, and the description of forcing used to keep the turbulence in a statistically steady state. Then, some of the turbulence properties which were computed during the simulations, such as energy spectra, viscous energy dissipation rate, etc., are presented. In addition, verification of the code for isotropic homogenous turbulence was done by comparing our simulations to the theory and numerical results taken from the literature. Finally, the two-parametric eddy viscosity, which was used to extend the inertial range at the weak magnetic field region, is described.

2.1 Details of the DNS scheme

We consider fully three-dimensional, incompressible, homogenous QS-MHD turbulent flow. It is well-known that in turbulence studies, the use of periodic boundary conditions allows employing highly accurate pseudo-spectral code (Rogallo, 1981). Thus, the domain is determined to be an unbounded cubic box. The flow is governed by the momentum equation with the Lorentz force (1.27) and the continuity equation (1.13).

By using mathematical identity, the nonlinear term in (1.27) can be formed as follows:

$$\mathrm{u}\cdot\left(\nabla\mathrm{u}\right)=\frac{1}{2}\nabla\left(\mathrm{u}\cdot\mathrm{u}\right)-\mathrm{u}\left(\nabla\times\mathrm{u}\right)=\nabla\left(\frac{u^2}{2}\right)-\mathrm{u}\times\boldsymbol{\omega}. \tag{2.1}$$

The first term in the RHS of the above equation can be added to the pressure gradient term of equation (1.27):

$$-\nabla\tilde{p}=-\nabla\left(\frac{p}{\rho}+\frac{u^2}{2}\right). \tag{2.2}$$

By substituting (2.1) and (2.2) into equation (1.27), and utilizing the continuity equation (1.13) to eliminate the pressure term, equation (1.27) in Fourier space can be written in the form:

$$\left(\frac{\partial}{\partial t}+\nu k^2+\frac{\sigma B_0^{\,2}}{\rho}\frac{k_z^{\,2}}{k^2}\right)u_i(\mathrm{k})=P_{ij}(\mathrm{k})\mathcal{F}[\mathrm{u}\times\boldsymbol{\omega}]_{\mathrm{j}}(\mathrm{k})+\xi_i(\mathrm{k}), \tag{2.3}$$

where $P_{ij}(\mathrm{k})$ is the projection operator on the plane normal to k (see (1.30)), which emerges from the elimination of the pressure term in the momentum equation and ensures the flow incompressibility, and $\mathcal{F}$ is the Fourier transform operator. The external forcing $\xi_i(\mathrm{k})$ maintains turbulence in a statistically steady state. It is a solenoidal, white in time Gaussian random force with correlator:

$$\left\langle\xi_i(t,\mathrm{k})\xi_j(t',\text{-k})\right\rangle=P_{ij}(\mathrm{k})\frac{F(k)}{4\pi k^2}\delta(t-t'). \tag{2.4}$$

The forcing spectrum $F(k)$ is constant over the low wave number band and zero otherwise (Eswaran and Pope, 1988). In all simulations, except for those with low 128^3 and 256^3 resolution, the forcing was placed in the range of scales $1\le k\le\sqrt{6}$. At the low resolution, the forcing occupied the modes $\sqrt{3}\le k\le\sqrt{12}$. In such a way

of forcing injection, the inertial range should be independent to the forcing applied at the large scales if it is random.

All linear terms in equation (2.3) were computed in Fourier space, whereas the nonlinear term, $u \times \omega$, was computed in physical space and then Fourier transformed. This computations method in "hybrid space" is known as the pseudo-spectral method (Rogallo, 1981) and it allows to reduce the computational time. The nonlinear term turns into a convolution term in Fourier space, which requires $O(M^2)$ operations (where M is the total number of grid points), while the Fourier transformation of the nonlinear term computed in physical space requires only $O(M\log(M))$ operations. Thus, periodic boundary conditions were applied in all three directions. The fourth order Runge-Kutta-Gill (RKG) method was employed for the time stepping. This method reduces the overall round-off error (Gill, 1951), and thus is more accurate than the standard Runge-Kuta method. The mathematical formalism of the RKG method is as follows:

$$
\begin{aligned}
&\frac{\partial u_i}{\partial t} = f\left(t, u_i\left(t\right)\right) \\
&k_{1,i} = \Delta t \cdot f\left(t, u_i\right) \\
&k_{2,i} = \Delta t \cdot f\left(t + \frac{1}{2}\Delta t, u_i + \frac{1}{2}k_{1,i}\right) \\
&k_{3,i} = \Delta t \cdot f\left(t + \frac{1}{2}\Delta t, u_i + \left(\frac{1}{\sqrt{2}} - \frac{1}{2}\right)k_{1,i} + \left(1 - \frac{1}{\sqrt{2}}\right)k_{2,i}\right) \\
&k_{4,i} = \Delta t \cdot f\left(t + \Delta t, u_i - \frac{1}{\sqrt{2}}k_{2,i} + \left(1 + \frac{1}{\sqrt{2}}\right)k_{3,i}\right) \\
&u_i^{m+1} = u_i^m + \frac{1}{6}\left(k_{1,i} + \left(2 - \sqrt{2}\right)k_{2,i} + \left(2 + \sqrt{2}\right)k_{3,i} + k_{4,i}\right) + O\left(\Delta t^5\right)
\end{aligned}
\tag{2.5}
$$

where u_i is the velocity of the i component, m denotes the stage of the time step, and Δt is the time step. Due to (2.3), the function $f\left(t, u_i\left(t\right)\right)$ is:

$$f\left(t,u_i\left(t\right)\right)=P_{ij}(\mathrm{k})\mathcal{F}[\mathrm{u}\times\boldsymbol{\omega}]_j(\mathrm{k})+\xi_i(\mathrm{k})-\left(\nu k^2+\frac{\sigma B_0^{\,2}}{\rho}\frac{k_z^{\,2}}{k^2}\right)u_i(\mathrm{k}). \qquad (2.6)$$

The fourth order RKG method requires 9×4 Fourier transformations for each time step. Factor 9 is due to the 3 backward and 6 forward Fourier transforms performed for each of the four RKG iterations. To remove the aliasing error produced due to the mixture of spectral and physical space computations, we used a truncation method (Patterson and Orszag, 1971) with $k_{max}=\sqrt{2}n/3$, where $n^3=M$. At the highest (viscous) end of the spectrum, the condition $k_{max}/k_{diss}>1$ was satisfied, where $k_{diss}=(\varepsilon/\nu^3)^{1/4}$ is the Kolmogorov dissipation wavenumber. More specifically, in the non-magnetic case, the values of k_{max}/k_{diss} were 3.26, 1.1, and 1.26, for resolution 256^3, 512^3, and 1024^3, respectively. A maximal Taylor micro-scale Reynolds number of $\mathrm{Re}_\lambda=407$ was achieved in the non-magnetic simulations. The initial condition was taken from a fully developed lower resolution result interpolated to a high-resolution grid to reduce the computational time. A statistically steady state was verified by observing the time evolution of the energy, $E(t)$. After the steady state was reached, all the computed turbulence properties were averaged in time.

The computed properties include the total turbulent energy:

$$E=\frac{3}{2}U^2=\frac{1}{2}\left\langle u_i\cdot u_i\right\rangle=\int_0^\infty E(k)dk\,, \qquad (2.7)$$

the viscous energy dissipation rate:

$$\varepsilon=2\nu\int_0^\infty k^2E(k)dk\,. \qquad (2.8)$$

the Taylor microscale (computed only in the non-magnetic simulations):

$$\lambda = \left(15\nu U^2 \,/\, \varepsilon\right)^{0.5}, \tag{2.9}$$

the rate of energy dissipation by magnetic friction:

$$\varepsilon_J = \tau_J^{-1} \left\langle \iiint \left|\mathrm{u(k)}\right|^2 \frac{k_3^2}{k^2} \frac{d\mathrm{k}}{(2\pi)^3} \right\rangle, \tag{2.10}$$

and other turbulence characteristics that will be defined before their first use. The symbol $\langle\cdot\rangle$ denotes ensemble averaging, and $E(k)$ is the three-dimensional (3D) energy spectrum that presents the energy of all modes in each spherical shell $S(k)$ of radius k and is defined as follows:

$$E(k) = \frac{1}{2} \left\langle \iint_{S(k)} \left|\mathrm{u(k)}\right|^2 \frac{d\sigma}{(2\pi)^3} \right\rangle. \tag{2.11}$$

The large-scale interaction parameter $N_0 = \tau_{tu} \,/\, \tau_J$ was computed using the following estimation of the large-scale eddy turnover time:

$$\tau_{tu} = (L_0^2 \,/\, \varepsilon_{inj})^{1/3}, \tag{2.12}$$

where $L_0 = \pi \,/\, k_f$, ε_{inj} and k_f are the total energy injection rate and the forcing wavenumber, respectively. The forcing wavenumber $k_f = \sqrt{6}$ was set at the end of the forcing range. The energy injection rate was computed using the energy balance equation:

$$\varepsilon_{inj} = \varepsilon + \varepsilon_J. \tag{2.13}$$

This pseudo-spectral code was written in Fortran language and parallelized with the Intel MPI (message passing interface) library. Most of the computational time was taken by the Fourier transform operations. Thus, the efficient parallel library, the FFTW (fastest Fourier transform in the west) library (Frigo and Johnson, 2005), was chosen to implement the FFT operations. The simulations were

performed on the BGU-HPC (Ben-Gurion university cluster) with up to 512 threads (11 nodes with 2XIntel Xeon E5-2697 V2 processor and 128 GB of RAM). A typical time step at resolution of 512^3 (1024^3) grid points on the 512 threads machine takes ~10 (~102) seconds. For the resolution of 512^3 grid points, reaching a statistically steady state takes ~24 hours for the non-magnetic, and ~48 hours for the magnetic case. After the statistically steady state was achieved, all the computed turbulence properties were averaged over a period of at least 10 turnover times, which takes between 1 to 2 weeks (for the resolution of 512^3 grid points), depending on the magnetic field strength. Therefore, because of the limitations of the computer resources, part of the DNSs were performed with 512^3 grid points.

2.2 Code verification

In the case of three-dimensional, homogeneous, isotropic turbulence, the turbulence characteristics are well known. Thus, we use them to verify the code. We also compared our results with those obtained by Gotoh *et al*. (2002), who performed high-resolution DNS of homogeneous isotropic turbulence using pseudo-spectral code with up to 1024^3 grid points. The governing equation in their study is identical to equation (2.3) (for the case of $B_0=0$). The forcing in their simulations is white noise in time, solenoidal Gaussian random function with the correlator (2.4). The time integration was performed using the fourth order RKG method, as in our DNS.

Gotoh *et al*. (2002) studied the velocity field statistics in the inertial to dissipation range, at Taylor microscales Reynolds number, Re_λ, between 38 and 460. At such relatively high values of Re_λ, the inertial range of the turbulence field is sufficiently long to investigate the turbulence characteristics. Our non-magnetic computations which were used for the comparison were done with up to 1024^3 grid

points, and Taylor microscales Reynolds number up to 381. We compared the total turbulent energy, energy dissipation rate, integral length scale $L = (3\pi / 4\int_0^\infty k^{-1}E(k)dk) / E$, Taylor microscale, λ, and the Kolmogorov microscale $l_{diss}=1/k_{diss}$. In addition to the above parameters, the three and one-dimensional energy spectra, and the second and third order velocity structure functions were compared. Table 2.1 summarizes the characteristic parameters used for comparison. The physical properties were computed by averaging over more than ten large eddy turnover times to achieve sufficient statistics. The values that appear in brackets in the table correspond to results obtained by Gotoh *et al*. (2002). At all Re_λ, the total energy is almost identical with a maximal relative error of $\Delta E_E = (E_{\mathrm{DNS}} - E_{\mathrm{Gotoh}}) / E_{\mathrm{DNS}}$ = 0.7%. The largest difference is in the integral length scale, with a relative error of ΔE_L = 14% at Re_λ=381. This difference could be explained by a shorter averaging time (4 turn-over times) in Gotoh's simulations.

An example of the energy evolution in time for Re_λ=284 is shown in Figure 2.1. The time is normalized by the large eddy turnover time, $t^* = t / \tau_{tu}$. The computation comprises 35 turnover times, and at least 20 of them are at steady state to ensure sufficient average at statistically steady state. After the steady state is reached, the total energy fluctuates around the average value given in Table 2.1. All the runs used for the verification, except the run with Re_λ=381, started from zero initial velocity field. The Re_λ=381 run was performed on 1024^3 grid points. To save the run time, the steady state velocity field from the run with 512^3 grid points was interpolated to 1024^3 grid and used to start the Re_λ=381 case.

Table 2.1. Comparison of statistical properties in our DNS vs. Gotoh *et al.* (2002) shown in the brackets.

n	Re_λ	$\nu\times10^{-4}$	Forcing range	E	ε	L	λ	$l_{diss}\times10^{-2}$
128^3	38	150	$\sqrt{3}\le k\le\sqrt{12}$	2.00 (1.99)	1.250 (1.190)	0.950 (0.891)	0.500 (0.501)	4.05 (4.10)
256^3	54	70	$\sqrt{3}\le k\le\sqrt{12}$	1.40 (1.39)	0.652 (0.627)	0.847 (0.829)	0.388 (0.393)	2.70 (2.72)
512^3	284	6	$\sqrt{1}\le k\le\sqrt{6}$	1.97 (1.96)	0.539 (0.530)	1.256 (1.246)	0.148 (0.149)	0.456 (0.449)
1024^3	381	2.8	$\sqrt{1}\le k\le\sqrt{6}$	1.74 (1.74)	0.504 (0.499)	1.317 (1.139)	0.098 (0.099)	0.257 (0.258)

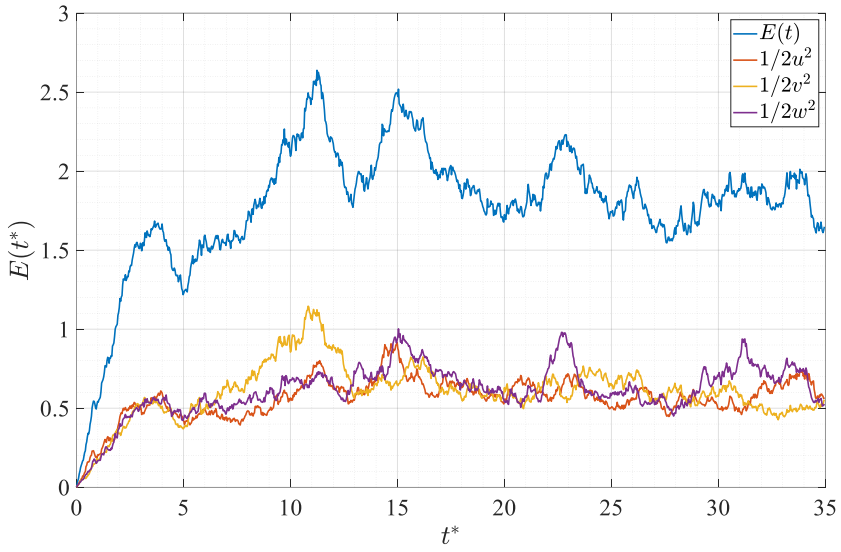

Figure 2.1. Time development of total and componential energies. The run time is normalized by the large eddy turnover time.

The three-dimensional energy spectra for the runs listed in Table 2.1 are shown in Figure 2.2 (a). The figure also contains the spectra from Gotoh *et al.* (2002). The energy spectra are normalized by the Kolmogorov spectrum (i.e., $\varepsilon^{-2/3}k^{5/3}$) to

obtain the Kolmogorov coefficient. The wave number, k, is multiplied by the Kolmogorov microscale l_{diss}. According to Gotoh *et al*. (2002), the obtained Kolmogorov constant C_K is in the range of 1.64 ± 0.04. Thus, a horizontal line with a value of 1.64 is added to emphasize the Kolmogorov constant.

An excellent agreement is achieved between the compared DNSs spectra, at all the Re_λ. As expected, with the increasing Re_λ, the spectra extend toward lower normalized wave numbers. For $\mathrm{Re}_\lambda \geq 284$, the normalized spectra contain a flat range that merges with the horizontal line and agrees with the theoretical spectrum, $E(k) = C_K \varepsilon^{2/3} k^{-5/3}$. At the end of the inertial range, the spectrum exhibits a foreseen bump between $0.04 < k l_{diss} < 0.3$, which is consistent with previous experimental and numerical observations (Saddoughi and Veeravalli, 1994; Yeung and Zhou, 1997).

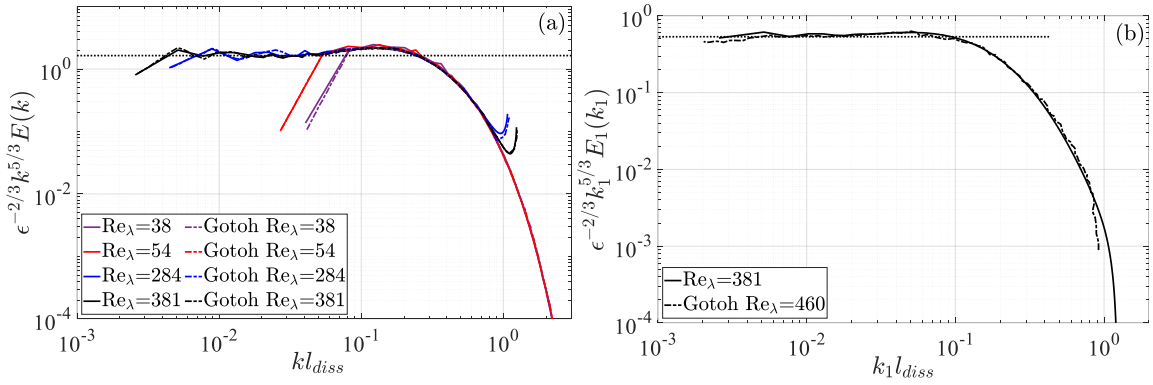

Figure 2.2. Compensated energy spectra (a) three-dimensional, $\varepsilon^{-2/3}k^{5/3}E(k)$, and (b) one-dimensional, $\varepsilon^{-2/3}k_1^{5/3}E_1(k_1)$. Solid lines: present DNS, dash-dotted lines: Gotoh *et al*. (2002) DNS. The horizontal dotted lines emphasize the corresponding theoretical constants.

Figure 2.2 (b) shows the compensated one-dimensional energy spectra, $\varepsilon^{-2/3}k_1^{5/3}E_1(k_1)$, obtained from the current DNS and the one computed by Gotoh *et al*. (2002). Also, a horizontal line is added to emphasize the theoretical coefficient value $18/55 C_K$. The achieved curve is flat in the range of $3\times10^{-3} < k_1 l_{diss} < 2\times10^{-2}$,

and good fitting to the theoretical value is obtained. Moreover, the agreement between the current DNS spectrum to this obtained in (Gotoh *et al.,* 2002) is very good.

In addition, the K41 theory was used to examine the degree of field isotropy by comparing with theoretical relations of the second order longitudinal ($S_2^{(L)}$) and transverse velocity ($S_2^{(T)}$) structure functions (Kolmogorov, 1941b):

$$S_2^{(T)}(r) = S_2^{(L)}(r) + \frac{r}{2}\frac{dS_2^{(L)}(r)}{dr}, \tag{2.14}$$

where:

$$\begin{aligned} S_p^{(L)}(r) &= \left\langle (\Delta u(x,r))^p \right\rangle, \ \Delta u(x,r) = (\mathrm{u(x+r)} - \mathrm{u(x)}) \cdot \mathrm{r} \,/\, r, \\ S_p^{(T)}(r) &= \left\langle (\Delta u(x,r_\perp))^p \right\rangle, \ \Delta u(x,r_\perp) = (\mathrm{u(x+r)} - \mathrm{u(x)}) \cdot (\mathrm{I} - \mathrm{r} \cdot \mathrm{r} \,/\, r^2) \cdot \mathrm{e}_\perp, \end{aligned} \tag{2.15}$$

$\mathrm{e}_\perp$ is the unit vector perpendicular to r, and I is the unit tensor. Figure 2.3 (a) shows a comparison between the two sides of the above relation divided by $r^{2/3}$, for Re_λ=284 and Re_λ=381. The solid curves represent the right-hand side, and the dash-dotted curves the left-hand side, both normalized by $r^{2/3}$. The $r^{2/3}$ scaling is another result of the K41 theory, which states that the *p*-order structure function is proportional to $r^{p/3}$. The isotropy relation for both Re_λ is excellent at separations smaller than ~$L/2l_{diss}$. At larger separation distances, the inertial range Kolmogorov relation does not hold.

The Kármán–Howarth–Kolmogorov equation provides an additional examination of isotropy (Kolmogorov, 1941a). For steady turbulence, the equation is as follows:

$$\frac{4}{5}\varepsilon r = -S_3^{(L)}(r) + 6\nu\frac{\partial S_3^{(L)}(r)}{\partial r} + \Theta(r), \tag{2.16}$$

where $\Theta(r)$ denotes contribution due to external force, and $S_3^{(L)}$ is the third order longitudinal structure function. In their study, Gotoh *et al*. (2002) showed that the external force effect decays quickly with the decreasing of the separation distance, while the viscous term effect grows gradually. In the inertial range, the forcing and viscosity terms are negligible, and the Kolmogorov's $4/5$ law takes place. Figure 2.3 (b) shows the compensated longitudinal third-order structure function, $-S_3^{(L)}(r) / \varepsilon r$, for Re_λ=284 (dash lines) and Re_λ=381 (solid lines). The dash horizontal line indicates the Kolmogorov value of 4/5. A good agreement is observed between the compared DNSs results at the range of small to intermediate separation distances. For both Re_λ, there is a small flat range, where the computed values are close to the theoretical 4/5 value. The maximum values of the curves are: 0.789 and 0.784, or 1.4% and 2% less than the 4/5 value, for Re_λ=284 and Re_λ=381, respectively.

In this section, several turbulent properties were compared with the theory and simulations by Gotoh *et al*. (2002) to ensure code verification. All the compared results showed a convincing agreement. Additionally, isotropic relations were examined and found to be realized as well. Therefore, we conclude that the present DNS code was successfully verified and suitable for turbulence calculations, and particularly for QS-MHD turbulence.

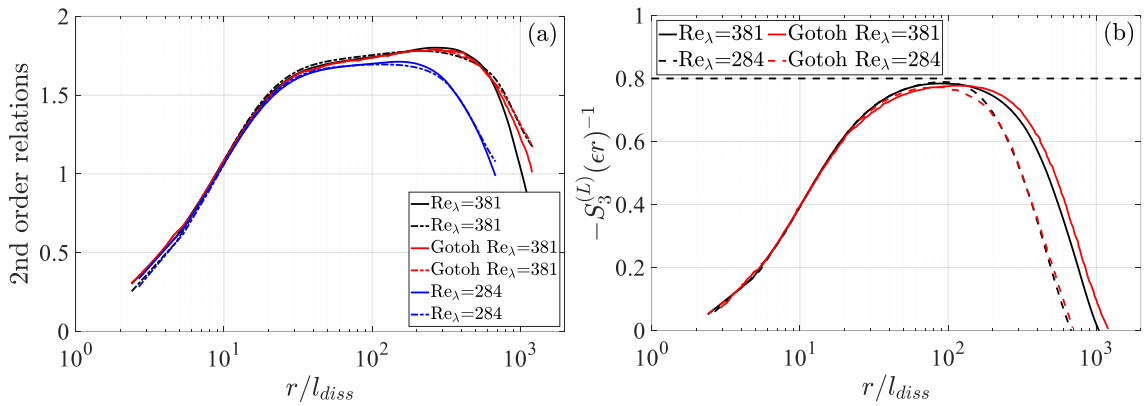

Figure 2.3. (a) Second order isotropy relation. Solid and dash-dotted lines represent $(S_2^{(L)}(r)+(r/2)(dS_2^{(L)}/dr))r^{-2/3}$ and $S_2^{(T)}(r)r^{-2/3}$, respectively. (b) Normalized third order longitudinal structure function, $-S_3^{(L)}/(\varepsilon r)$. Black, red, and dashed horizontal lines correspond to present DNS, Gotoh *et al*. (2002) DNS and Kolmogorov's 4/5 law, respectively.

2.3 Two-parametric eddy viscosity

Computations with a weak magnetic field were used to examine the effect of the magnetic field strength on the progressive turbulence anisotropization and validate the QNSE predictions. The highest resolution in this study, 1024^3, was insufficient to clearly reveal the transition from the $k^{-7/3}$ to the $k^{-5/3}$ part of the spectrum. Thus, the two-parametric eddy viscosity (TPEV) $\nu(k|k_c)$ was employed to extend the Kolmogorov inertial range.

Kraichnan, in his noted paper (Kraichnan, 1976), clarified the limitations on the use of the customary eddy viscosity to represent the dynamic effects of small-scale turbulence. The classical concept of eddy viscosity implies that small scales act on other scales as if to augment the impact of thermal molecular motion. The effect of thermal agitation is represented by a molecular viscosity, which is independent of the fluid motion due to the large separation between the spatial and temporal scales of molecular and fluid motions. The analogy between subgrid scales of turbulence

and thermal agitation is flawed because turbulence displays a continuous distribution of scale sizes, with no separation between subgrid and resolvable scales. Kraichnan explained that the correct representation of the effect of scales with $k>k_c$ on any mode $k<k_c$ should account for the energy transfer $T(k|k_c)$ from mode k to all modes $k>k_c$. Then, an effective eddy viscosity, acting on a mode k due to dynamic interactions with subgrid scales $k>k_c$, may be defined by:

$$\nu(k|k_c) = -T(k|k_c) / \left[2k^2 E(k)\right] \tag{2.17}$$

with the energy transfer function $T(k|k_c)$ given by the integral of the triad (k, p, q) interactions:

$$T(k|k_c) = \iint_{\Delta} T(k,p,q)dpdq, \quad k < k_c\,, \tag{2.18}$$

where

$$T(k,p,q) = -\frac{i}{2} P_{\alpha\beta\gamma}(\mathrm{k})\left\langle u_\alpha(-\mathrm{k}) u_\beta(\mathrm{p}) u_\gamma(\mathrm{q})\right\rangle \tag{2.19}$$

and the integral $\iint_{\Delta}$ is taken over all the wavenumber triads $\mathrm{k}+\mathrm{p}+\mathrm{q}=0$ with p and/or $q>k_c$. For isotropic 3D or 2D turbulence, the energy transfer function $T(k|k_c)$ can be computed using one of the quasi-normal approximations (McComb, 2014). In the 3D case, the function $T(k, p, q)$ is given by:

$$T(k,p,q) = 4\pi^2 k^3 b_3(k,p,q) pq\theta_{k,p,q}[U(p) - U(k)]U(q), \tag{2.20}$$

in which

$$b_3(k,p,q) = \frac{1}{2} k^{-4} \sin^2\alpha[(k^2 - q^2)(p^2 - q^2 + k^2 p^2)], \tag{2.21}$$

α is the angle opposite k in the triad (k, p, q) and $\theta_{k,p,q}$ is the characteristic time of the triad interaction. The latter can be determined by using the QNSE-derived eddy viscosity $\nu_n(k) \approx 0.5\varepsilon^{1/3}k^{-2/3}$ (equation (1.36)) as:

$$\theta_{k,p,q} = [\nu_n(k)k^2 + \nu_n(p)p^2 + \nu_n(q)q^2]^{-1}. \quad (2.22)$$

This result was first obtained by Dannevik *et al*. (1987) employing the RNG theory. It was adapted for 2D isotropic and anisotropic turbulence in Refs. (Chekhlov *et al.,* 1994) and (Chekhlov *et al.,* 1996), respectively.

The analytically derived TPEV $\nu(k|k_c)$ was tested by DNS. The velocity field was computed by solving equation (2.3) with $B_0 = 0$ using 1024^3 Fourier modes. Next, we calculated the energy transfer function $T(k|k_c)$ by computing the third-order velocity cumulant (2.19) from the DNS results and substituting it into the integral (2.18). We set $k_c = 50$ well inside the inertial subrange. The DNS-inferred normalized TPEV $\nu(k|k_c) / \nu(0|k_c)$ is plotted in Figure 2.4 (a), along with the QNSE-based analytical prediction. A similar comparison of the DNS and the analytical TPEV in two dimensions taken from Ref. (Chekhlov *et al.,* 1994) is plotted in Figure 2.4 (b). The agreement between the DNS-based and the analytical results is good up to the wavenumbers close to k_c, where the DNS data saturate, while the analytical curves exhibit a sharp cusp. The physics underlying this cusp was explained by Chekhlov *et al*. (1994) as follows: the closer k approaches to k_c, the more elongated triads, with either p or $q << k_c$, become involved in the energy exchange between the mode k and the subgrid scale modes. The contribution from triads with small p or q brings about the cusp behavior of the theoretical TPEV. In a finite box DNS, the energy of small wavenumber modes is low. As a result, instead of growing sharply, the TPEV saturates as k approaches k_c. This effect decreases as the cut-off wavenumber k_c increases, and the TPEV approaches the theoretical curve, as was verified by the DNS with k_c set to 20, 30 and 40 (not shown here).

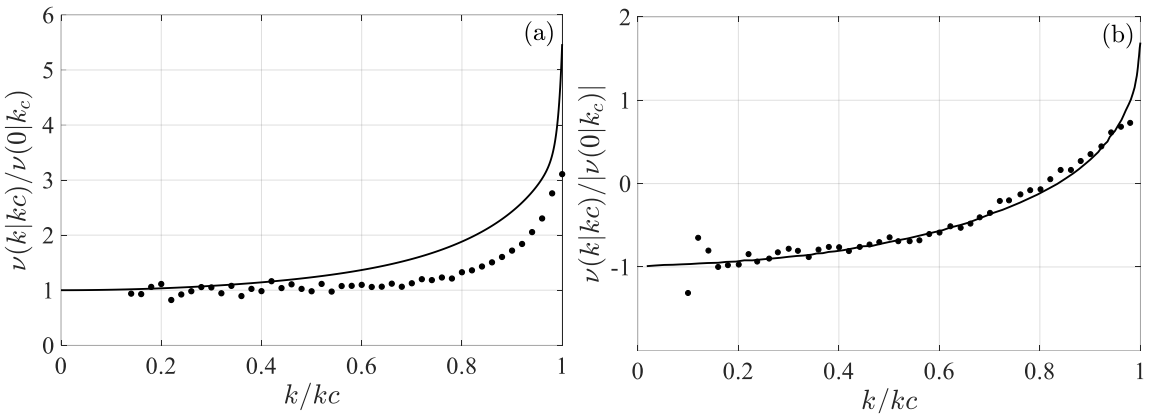

Figure 2.4. Two-parametric eddy viscosity $\nu(k \mid k_c)$ normalized by $\nu(0 \mid k_c)$ for 3D geometry (left panel) and 2D geometry (right panel). The 2D results are taken from Ref. (Chekhlov *et al.,* 1994). The solid line represents theoretical curves, and the dots are the DNS results.

Finally, we ran 1024^3-resolution simulations with the TPEV in which k_c was set to 483, the maximal resolvable wavenumber after the de-aliasing truncation. The energy spectrum shown in Figure 2.5 (a) exhibits almost perfect -5/3 scaling over a wide range of scales. In simulations with constant viscosity, the Kolmogorov inertial range extends from the forcing scale to $k \approx 25$, and it increases by more than twofold when the TPEV is employed. A bulge typical of the near dissipation region of the energy cascade range appears at the high wavenumbers end of the spectrum (Falkovich, 1994; Frisch *et al.,* 2008; Donzis and Sreenivasan, 2010). The compensated spectrum presented in Figure 2.5 (b) shows the Kolmogorov constant $C_K \approx 1.6$, which is in the range of 1.62 ± 0.17 that was established in (Sreenivasan, 1995), based upon numerous experiments and observations.

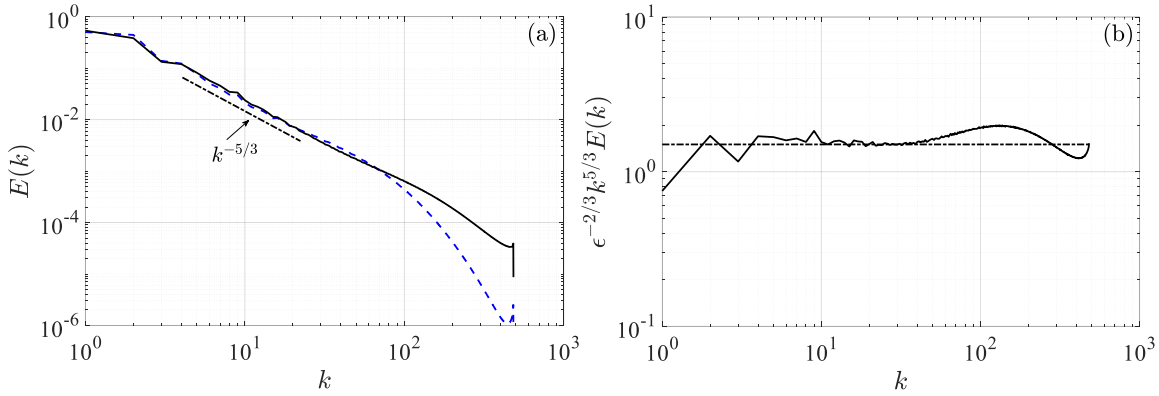

Figure 2.5. (a) 3D energy spectrum in 1024^3-grid point simulations with constant viscosity (dashed blue line) and TPEV (solid black line), (b) compensated energy spectrum obtained with TPEV.

Chapter 3

Results of QS-MHD Simulations

The numerical study of turbulence anisotropization of QS-MHD by increasing magnetic field is presented in this chapter. Previous studies related to the anisotropy of QS-MHD are described in section 1.4. The numerical simulations were performed for various interaction parameters, N_0, in the range 0 to 806. The details of the simulation method and the forcing used to maintain statistically steady state turbulence are described in section 2.1. During the simulations, all the turbulence computed properties, i.e., energy spectra, energy and enstrophy fluxes, energy dissipation rate, etc., were saved and then time averaged during more than ten turn-over times to achieve the statistically steady state properties.

The parameters and the computed physical quantities of the simulations are summarized in Table 3.1. The runs are completely characterized by two dimensionless parameters presented in the table: N_0 and $R_0 = \tau_\nu / \tau_{tu}$, where the "viscous dissipation" time τ_ν was defined as:

$$\tau_\nu = L_0^2 / \nu . \tag{3.1}$$

R_0 was chosen instead of the microscale Reynolds number Re_λ due to ambiguity in definition of the microscale caused by the flow anisotropy.

Table 3.1. Parameters of the simulations: n is the grid size, $N_0 = \tau_{tu} / \tau_J$ is the interaction parameter, $R_0 = \tau_\nu / \tau_{tu}$ is the Reynolds number, $\tau_J^{-1} = (\sigma B_0^2) / \rho$ is the characteristic time of Joule dissipation, ν is the kinematic viscosity, ε_{inj} is the total energy injection rate, and ε is the viscous energy dissipation rate.

n	N_0	R_0	τ_J^{-1}	ν	ε_{inj}	ε
512^3	0	1770	0	6×10^{-4}	0.44	0.44
512^3	1.5	1870	1	6×10^{-4}	0.52	8.5×10^{-2}
512^3	9.4	1750	6	6×10^{-4}	0.43	2.6×10^{-2}
512^3	16	1740	10	6×10^{-4}	0.42	5×10^{-2}
512^3	62	1770	40	6×10^{-4}	0.44	7.4×10^{-2}
512^3	95	1730	60	6×10^{-4}	0.41	7.3×10^{-2}
512^3	127	1730	80	6×10^{-4}	0.41	8×10^{-2}
512^3	254	1730	160	6×10^{-4}	0.41	8.8×10^{-2}
1024^3	0	3950	0	2.8×10^{-4}	0.5	0.5
1024^3	1.5	3840	1	2.8×10^{-4}	0.46	6.4×10^{-2}
1024^3	4.9	10000	3	1×10^{-4}	0.37	9.6×10^{-3}
1024^3	252	5220	160	2×10^{-4}	0.42	7.7×10^{-2}
1024^3	806	5100	500	2×10^{-4}	0.39	7.2×10^{-2}
1024^3	0	-	0	TPEV	0.6	0.6
1024^3	1.5	-	1	TPEV	0.54	7.7×10^{-2}
1024^3	2.2	-	1.5	TPEV	0.52	4×10^{-2}

3.1 Energy spectra

3.1.1 Modification of the energy spectra by a weak magnetic field

The results presented in the previous chapter indicate that the TPEV is an efficient device, allowing maximal extension of the inertial range up to the highest resolvable wavenumber, which is effectively equivalent to increasing the Reynolds number. This extension is important for identification of different slopes in the kinetic energy spectrum, as predicted by the QNSE theory, namely, the –7/3 slope, imposed by the magnetic field effect at the lower end of the spectrum, and the residual Kolmogorov -5/3 slope at the higher end of the inertial range. Modification of the spectrum $E(k)$ (equation (2.11)) by a relatively weak magnetic field ($N_0 = 1.5$) is presented in Figure 3.1 for simulations with 512^3 and 1024^3 grid points. The -7/3 power law is clearly seen at low wavenumbers. As the magnetic field increases, the -7/3 range propagates toward higher wavenumbers, where it changes to the -5/3 power law. A relatively short inertial range in simulations with constant ("molecular") viscosity makes it difficult to conclusively identify the transition. Only at the highest resolution is the transition from the $k^{-7/3}$ to the $k^{-5/3}$ spectrum evident. The transition is clearly seen in the simulations with 1024^3 grid points and especially with TPEV.

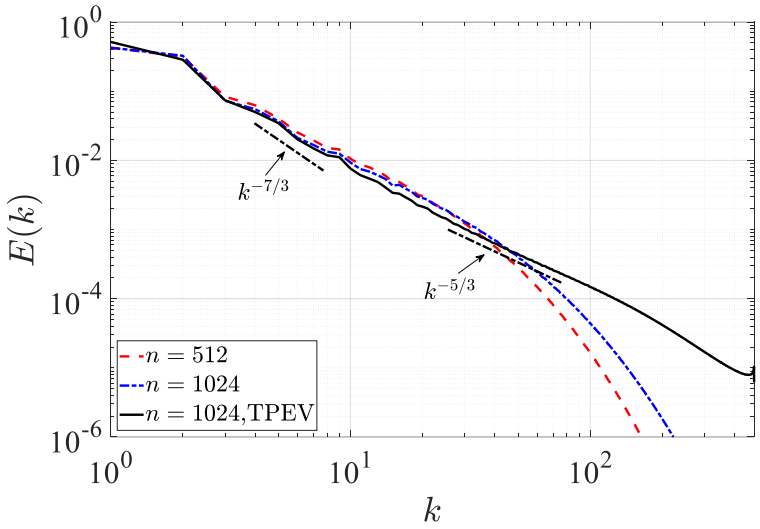

Figure 3.1. 3D energy spectrum computed with constant viscosity (dashed red and dash-dotted blue lines, which correspond to 512^3 and 1024^3 resolutions, respectively) and TPEV (solid black line) at $N_0 = 1.5$.

It is important to evaluate the extension of the spectral region affected by the magnetic field and to determine the boundary of the -7/3 spectral range propagation toward higher wavenumbers with increasing field strength. Figure 3.2 shows the 3D energy spectra obtained in simulations with 1024^3 grid points and with either the TPEV (Figure 3.2 (a)) or constant viscosity (Figure 3.2 (b)). The spectra shown in Figure 3.2 (a) correspond to three different values of the interaction parameter, $N_0 = 0$, $N_0 = 1.5$, and $N_0 = 2.2$, while the spectrum in Figure 3.2 (b) corresponds to $N_0 = 4.9$. The two slopes exist in nonzero field simulations with TPEV. The transitional wavenumber moves from $k_{tr} \approx 10$ at $N_0 = 1.5$ to $k_{tr} \approx 15$ at $N_0 = 2.2$. With an increasing field, at $N_0 = 4.9$, the -7/3 power law extends to the whole range of scales not affected by viscous dissipation, as may be seen in Figure 3.2 (b). At such a field strength, the isotropic equations (2.20) – (2.22) are not valid for computations of two-parametric viscosity, and therefore constant viscosity was used in the DNS.

The computed value of k_J is 53, indicating that the transition occurs inside the dissipation range and cannot be seen on the spectrum.

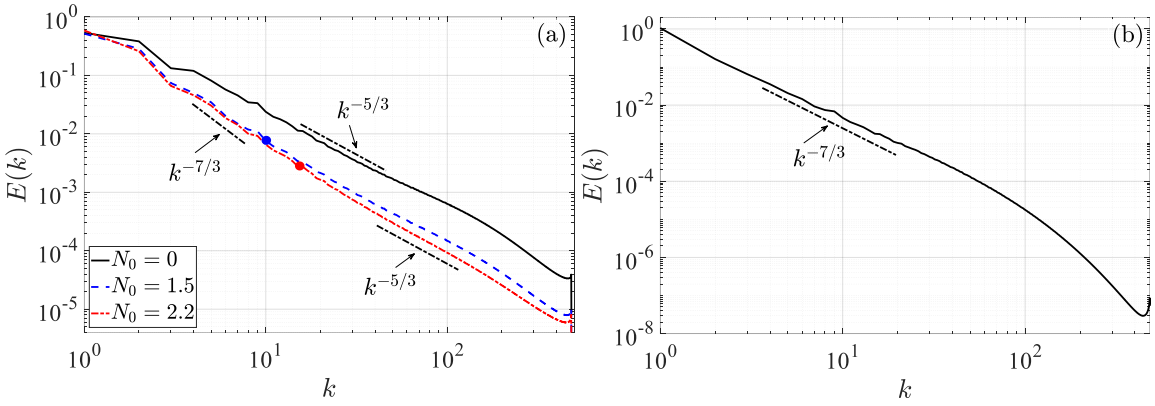

Figure 3.2. 3D energy spectra for different values of the interaction parameter (a) $N_0 = 0$ (black solid line), 1.5 (dashed blue line), and 2.2 (red dash-dotted line), and (b) $N_0 = 4.9$.

3.1.2 Detailed comparison of DNS with the QNSE theory: 3D and 1D energy spectra

The QNSE theory predicts 3D and all 1D longitudinal and transverse energy spectra. The 1D energy spectra, $E_i(k_j)$, were calculated as follows:

$$E_i(k_j) = \left\langle \iint \left|u_i(\mathrm{k})\right|^2 \frac{dk_l dk_m}{(2\pi)^2} \right\rangle, \tag{3.2}$$

where i, j, l, m = 1, 2, 3 and $j \neq l$, m.

The QNSE theory not only predicts development of the -7/3 power scaling spectral range and its propagation to higher wavenumbers with an increasing magnetic field, but also determines the spectral amplitudes. The QNSE-derived spectra were verified by comparison with the DNS results. Figure 3.3 (a)-(f) shows 3D and 1D energy spectra at various strengths of the magnetic field, divided by the corresponding theoretical spectra (1.38) – (1.39). At the relatively small interaction parameters, N_0 = 1.5 and N_0 = 2.2, these ratios are close to 1 over the whole range of

resolvable scales, with the exception of the near dissipation cut-off region. In that region, the 3D spectrum exhibits the foreseen "bump," while the 1D spectra decay quickly. This decay may be explained by the use of the TPEV, which was designed to emulate the dissipative effect of all scales $k > k_c$, while the theoretical 1D spectra $E_i(k_j)$ contain contributions from wave-vectors k whose amplitude is larger than k_c [recall that $E_i(k_j)$ is computed by integration of $|u_i(\mathrm{k})|^2$ over the plane orthogonal to the j-axis (Sukoriansky and Zemach, 2016)]. The good agreement obtained between the theoretical 1D spectra and the DNS results is especially important, since 1D spectra provide detailed information on the development of anisotropy due to the impact of the magnetic field.

At a stronger field, $N_0 = 4.9$, constant viscosity was used, and the scales with $k > 30$ were suppressed by viscous dissipation. On larger, not suppressed, scales, the agreement of the 3D spectrum $E(k)$ and 1D spectrum $E_3(k_3)$ with the QNSE theory remains good, but all other 1D theoretical spectra, except the transverse spectrum of the velocity component parallel to the field, $E_3(k_1)$, are greater than the DNS spectra. Recall that the QNSE theory was developed on the assumption of a weak magnetic field. The DNS results determine the limit of this approximation, which is valid at least up to $N_0 = 2.2$, but becomes inaccurate at $N_0 > 4$.

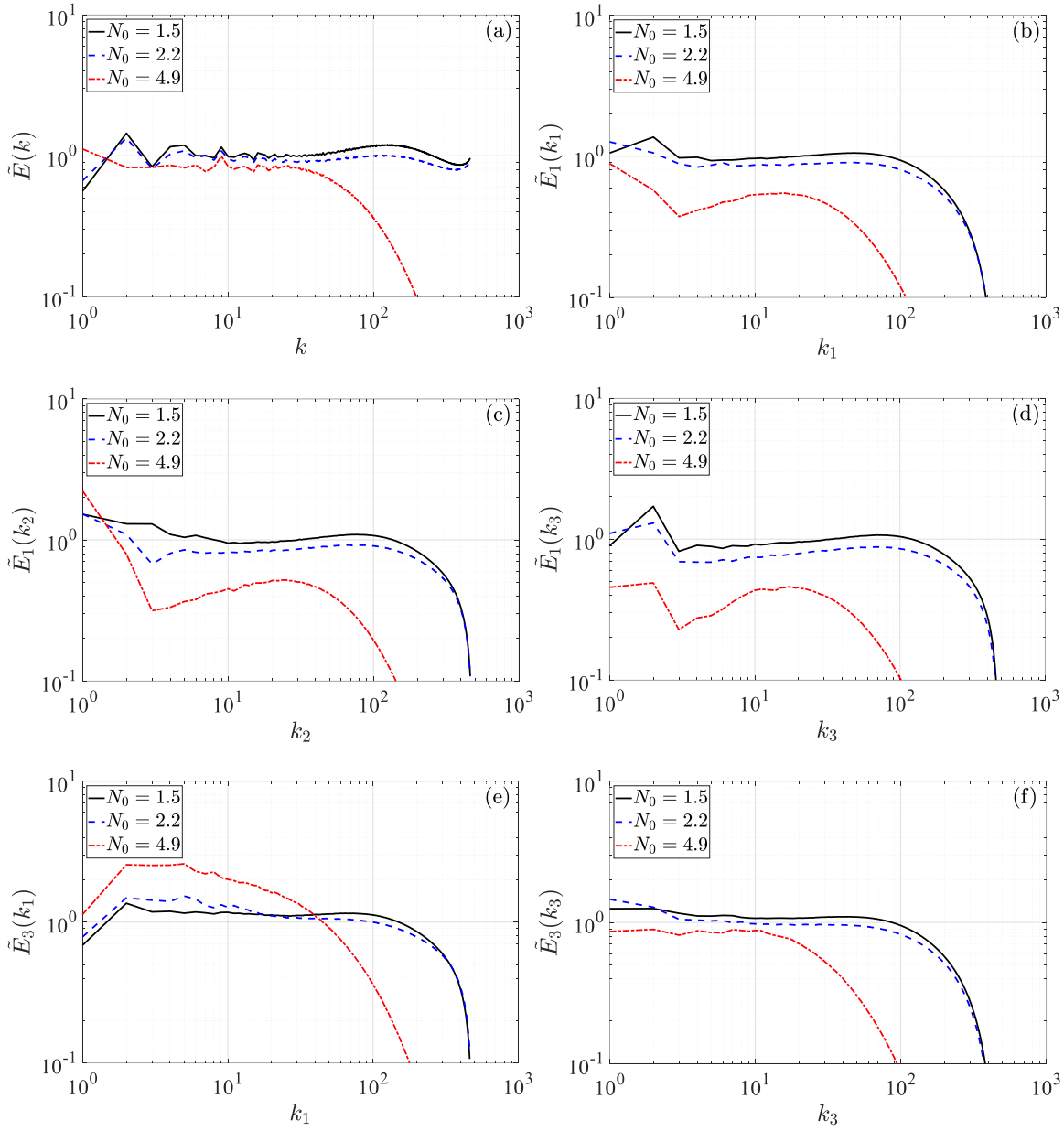

Figure 3.3. Comparison of the DNS-derived energy spectra with the QNSE prediction. (a) normalized 3D spectrum $\tilde{E}(k) = E(k)_{DNS} \,/\, E(k)_{QNSE}$, (b)-(f) normalized 1D spectra $\tilde{E}_i(k_j) = E_i(k_j)_{DNS} \,/\, E_i(k_j)_{QNSE}$. Solid black dashed blue and dash-dotted lines correspond to $N_0 = 1.5$, $N_0 = 2.2$ and $N_0 = 4.9$, respectively.

3.1.3 Quasi static MHD turbulence in intermediate and strong magnetic fields: Transition to quasi-2D turbulence

Since the application of the QNSE theory to QS-MHD, which is based on a weak magnetic field approximation, is inaccurate at $N_0 > 4$, the turbulence anisotropization at stronger fields was studied numerically. DNSs were performed with a progressively increasing interaction parameter whose value was set to 9.4, 16, 62, 95, 127 and 254. To save run time, most of the simulations in this range were performed with 512^3 grid points. Modification of the 3D spectrum with an increasing field is shown in Figure 3.4. At $N_0 = 9.4$, the spectrum still obeys the -7/3 power law. This scaling disappears with increasing field strength, and the spectrum becomes shallower.

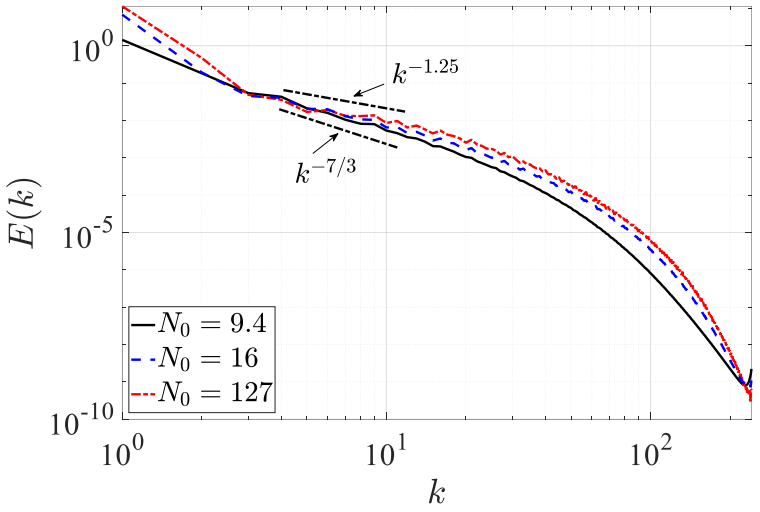

Figure 3.4. 3D energy spectra at different magnetic field strengths: $N_0 = 9.4$ solid black line; $N_0 = 16$ dashed blue line; $N_0 = 127$ dash-dotted red line.

Due to turbulence anisotropy in a strong magnetic field, the 3D spectrum becomes less informative as it mixes energies of parallel and perpendicular flow components and scale directions. In addition, Figure 3.4 indicates that it is doubtful whether $E(k)$ obeys a universal scaling. The 1D and 2D spectra are far more informative since they shed light on the turbulence anisotropization and the

modification of turbulence dynamics. The modification of the transverse and longitudinal 1D spectra, $E_1(k_3)$ and $E_3(k_3)$, with an increasing magnetic field is shown in Figure 3.5. As expected, the fluctuations in the direction of the magnetic field ($k_3 \equiv k_\parallel$) degenerate as the interaction parameter increases. All scales are suppressed by several orders of magnitude, with the smallest scales being completely smoothed out.

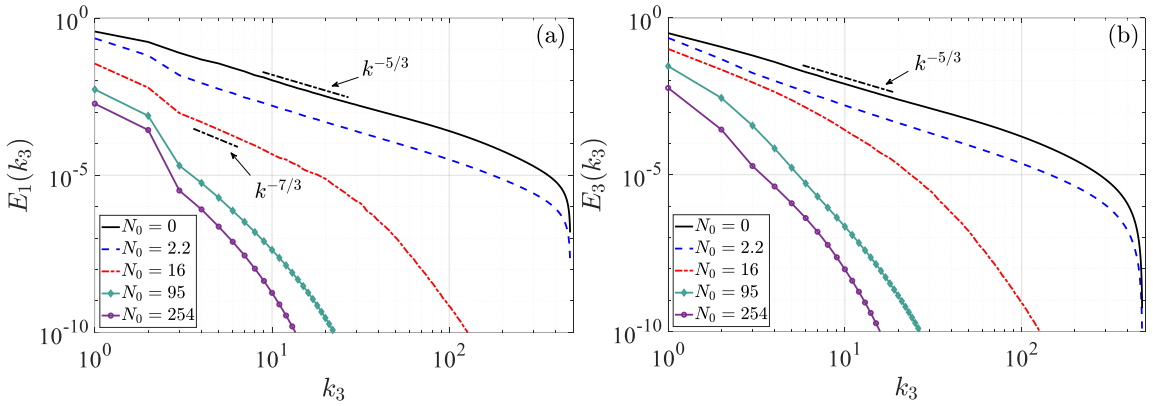

Figure 3.5. Modification of the transverse $E_1(k_3)$ and longitudinal $E_3(k_3)$ spectra with an increasing magnetic field.

Most interesting are the 2D energy spectra of the velocity field in the plane normal to B,

$$E_\perp(k_\perp) = \frac{1}{2} \iint_{S(k_\perp)} \left\langle \left|u_1(\mathrm{k})\right|^2 + \left|u_2(\mathrm{k})\right|^2 \right\rangle \frac{d\sigma}{(2\pi)^3} \tag{3.3}$$

and the velocity component parallel to B,

$$E_\parallel(k_\perp) = \frac{1}{2} \iint_{S(k_\perp)} \left\langle \left|u_3(\mathrm{k})\right|^2 \right\rangle \frac{d\sigma}{(2\pi)^3} \tag{3.4}$$

as functions of the perpendicular wavenumber $k_\perp = \sqrt{k_1^2 + k_2^2}$. Here $S(k_\perp)$ is a cylindrical shell of radius $k_\perp$. With increasing magnetic field strength, these spectra undergo significant changes, indicating a transition to quasi-2D turbulence. Spectra $E_\perp(k_\perp)$ and $E_\parallel(k_\perp)$ at intermediate values of N_0 are shown in Figure 3.6 (a) and (b),

respectively. Both spectra obey the -7/3 scaling power law at N_0 = 9.4 between the forcing and viscous dissipation ranges. The perpendicular spectrum $E_\perp(k_\perp)$ almost does not change with increasing N_0, and the -7/3 power law remains intact up to N_0 = 62. In this range of the interaction parameter and beyond, the parallel spectrum $E_\parallel(k_\perp)$ gradually becomes less steep.

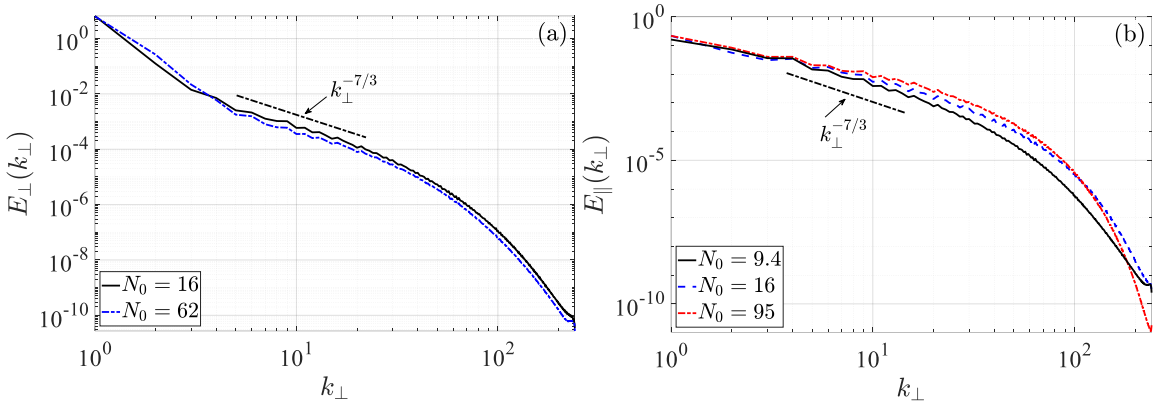

Figure 3.6. Perpendicular and parallel energy spectra at intermediate values of the interaction parameter.

A dramatic change occurs at N_0 = 95. At this value of the interaction parameter, the perpendicular spectrum $E_\perp(k_\perp)$ becomes proportional to k^{-3} in a wide range of scales (see Figure 3.7 (a)), while the parallel spectrum $E_\parallel(k_\perp)$ scales as k^{-1} (Figure 3.7 (b)). Both spectra remain unchanged with further increases in the strength of the magnetic field. This lack of sensitivity of the spectra to Joule friction implies that the velocity field has become completely smoothed in the direction of the magnetic field (a claim supported by Figure 3.5). In other words, at such interaction parameters, the turbulence reaches the 2D-3C state as previously claimed in (Favier *et al.,* 2010; Reddy and Verma, 2014).

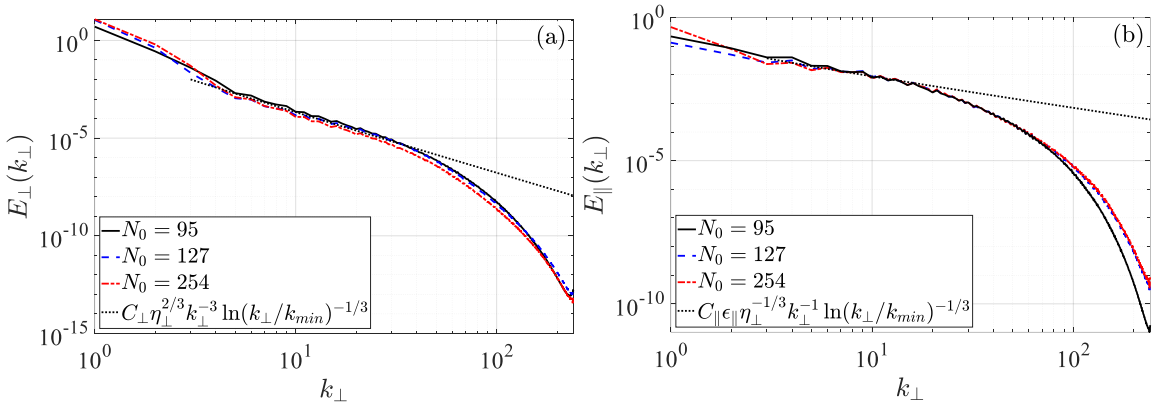

Figure 3.7. Perpendicular and parallel energy spectra at large values of the interaction parameter.

We now reexamine the action of Joule friction on turbulence. In a weak magnetic field, the dominant effect of Joule friction is seen in decreasing gradients in the direction of the magnetic field. This, in turn, leads to suppression of nonlinear interactions between the perpendicular and the parallel flow components. Eventually, the parallel component becomes passive scalar steered and advected by the 2D perpendicular flow field.

So far, we have analyzed spectral powers. The -3 power spectrum in 2D is commonly associated with a direct enstrophy cascade (Kraichnan, 1967; Batchelor, 1969). However, QS-MHD is an anisotropic 3D phenomenon, with an additional governing dimensional parameter, τ_J. Although it is known that the spectral slopes in a strong magnetic field correspond to isotropic 2D turbulence, additional information is necessary to clarify the underlying physics. Energy and enstrophy fluxes together with spectral amplitudes will provide the required information.

3.2 Energy and enstrophy fluxes

In anisotropic turbulence, the fluxes – also being anisotropic – have to be considered separately for different flow components and in different spectral directions. Most interesting are the fluxes of perpendicular and parallel energy $\Pi_{E\perp}(k_\perp)$, $\Pi_{E\parallel}(k_\perp)$ and enstrophy $\Pi_{Z\perp}(k_\perp)$, $\Pi_{Z\parallel}(k_\perp)$ from the spectral region inside a cylinder of radius $k_\perp$ outward. The flux is negative if it is directed inward. An efficient method for computation of the energy or enstrophy fluxes is to compute the nonlinear term in the corresponding momentum or vorticity equation in physical space, Fourier transform it, and multiply it by filtered velocity or vorticity with all Fourier modes $k_1^2 + k_2^2 > k_\perp^2$ set to 0. The filtered velocity is defined as:

$$\mathrm{u}(\mathrm{k},t\,|k_\perp) = \mathrm{u}(\mathrm{k},t)H(k_\perp - \sqrt{k_1^2 + k_2^2}), \tag{3.5}$$

where H is a Heaviside step function. The real part of the result is integrated over the cylinder and time averaged. To be more precise, the energy fluxes are:

$$\Pi_{E\perp}(k_\perp) = -\Re\left\langle \iiint_{V(k_\perp)} u_i^*(\mathrm{k},t\,|\,k_\perp)\mathcal{F}\left(u_j\frac{\partial u_i}{\partial x_j}\right)\frac{d\mathrm{k}}{(2\pi)^3}\right\rangle,\ \ i \neq 3\,, \tag{3.6}$$

$$\Pi_{E\parallel}(k_\perp) = -\Re\left\langle \iiint_{V(k_\perp)} u_3^*(\mathrm{k},t\,|\,k_\perp)\mathcal{F}\left(u_j\frac{\partial u_3}{\partial x_j}\right)\frac{d\mathrm{k}}{(2\pi)^3}\right\rangle, \tag{3.7}$$

where the symbols $\Re$ and * denote the real part and the complex conjugate, respectively. The integral is computed over a cylindrical volume of radius $k_\perp$, $V(k_\perp)$. The summation over repeating indexes is implied, whereas the summation in (3.6) involves only i equal 1 and 2.

Similar formulas are used for the computation of enstrophy fluxes based on the vorticity equation. Note, that the "perpendicular" enstrophy is the mean square

vorticity of the 2D velocity field perpendicular to B. In other words, if $\boldsymbol{\omega}=\nabla\times\mathbf{u}$ is vorticity, then $Z_\perp=\left\langle|\omega_3|^2\right\rangle$:

$$\Pi_{Z\perp}(k_\perp)=-\Re\left\langle\iiint_{V(k_\perp)}\omega_3^*(\mathrm{k},t\,|\,k_\perp)\mathcal{F}\left(u_j\frac{\partial\omega_3}{\partial x_j}\right)\frac{d\mathrm{k}}{(2\pi)^3}\right\rangle, \tag{3.8}$$

$$\Pi_{Z\parallel}(k_\perp)=-\Re\left\langle\iiint_{V(k_\perp)}\omega_i^*(\mathrm{k},t\,|\,k_\perp)\mathcal{F}\left(u_j\frac{\partial\omega_i}{\partial x_j}\right)\frac{d\mathrm{k}}{(2\pi)^3}\right\rangle,\ i\neq 3. \tag{3.9}$$

Energy and enstrophy fluxes at zero field are shown in Figure 3.8. As expected, the energy flux is constant in the inertial range. In this region, the enstrophy fluxes grow proportionally with k^2. The perpendicular flux $\Pi_{E\perp}(k_\perp)$ is twice as large as the parallel flux $\Pi_{E\parallel}(k_\perp)$.

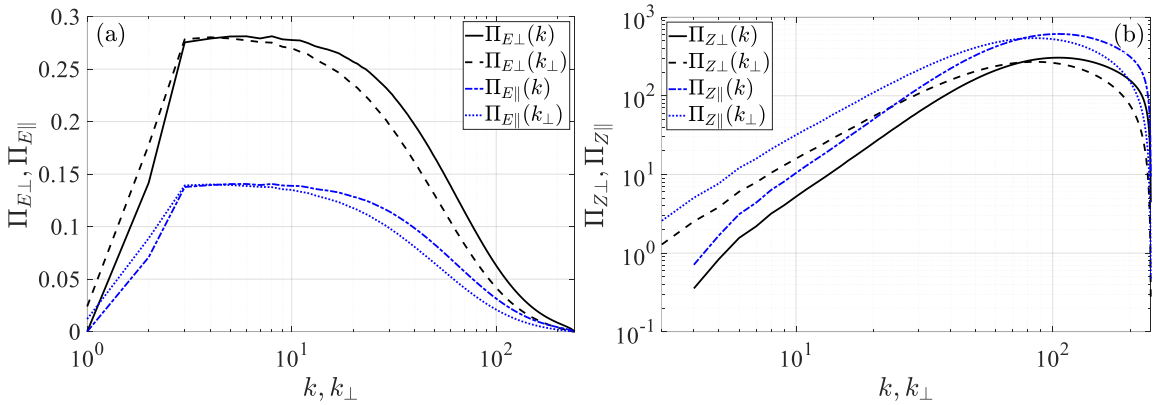

Figure 3.8. Perpendicular and parallel components of the energy (a) and enstrophy (b) fluxes at $N_0 = 0$.

The fluxes change radically as the magnetic field strength increases, as shown in Figure 3.9. The changes are caused partially by Joule friction, which dissipates part of the energy injected into the flow. In a weak magnetic field, $N_0 = 1.5$, the parallel and perpendicular energy fluxes remain closely comparable. Marked anisotropization of the energy flux occurs in stronger fields of $N_0 \geq 9.4$. At these values

of the interaction parameter, the flux in the plane normal to B completely degenerates outside of the energy injection region and becomes negative inside this region. The parallel flux changes more gradually, eventually reaching a constant value $\varepsilon_{\parallel}$ in the "inertial" range between the forcing and dissipation ranges. At first sight, the latter result appears peculiar, but it can be explained in terms of quasi-2D dynamics. We will verify that u_3 becomes a 2D passive scalar and explore the origin of $\varepsilon_{\parallel}$ later, but first, we examine the enstrophy fluxes.

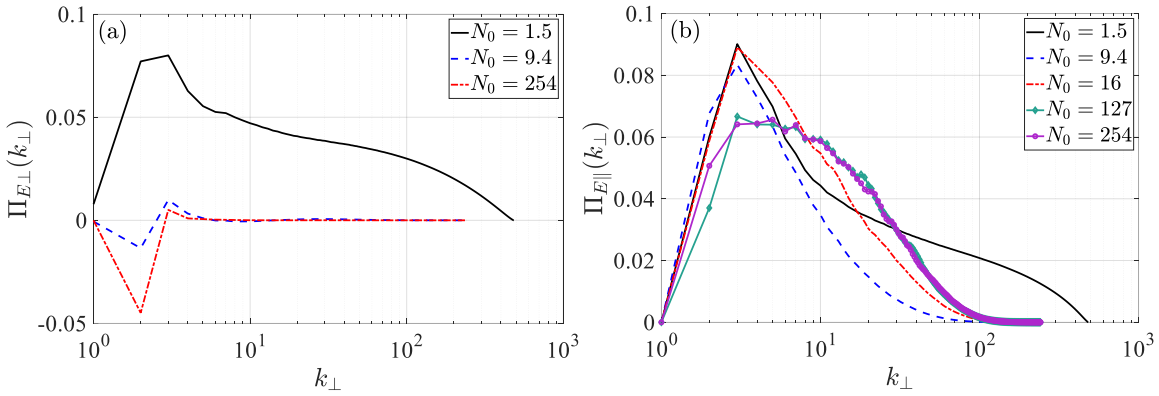

Figure 3.9. Modification of perpendicular (a) and parallel (b) components of the energy flux with increasing magnetic field strength.

Modification of enstrophy fluxes by a magnetic field is presented in Figure 3.10. The parallel flux $\Pi_{Z\parallel}(k_\perp)$ grows proportionally with $k_\perp^2$ in the region of constant energy flux. The flux in the plane normal to B, $\Pi_{Z\perp}(k_\perp)$, decreases with an increasing magnetic field until it levels off at a constant value $\eta_\perp$ in the inertial range at $N_0 \gtrsim 120$. The flux does not change any further at higher values of the interaction parameter. Recall that at such values of N_0 the energy flux in the normal plane is close to 0 and the spectrum $E_\perp(k_\perp)$ is proportional to $k_\perp^{-3}$. A constant enstrophy flux combined with a zero energy flux and a -3 power spectrum indicate a direct enstrophy cascade of 2D turbulence. The spectral amplitude provides ultimate evidence of such a cascade.

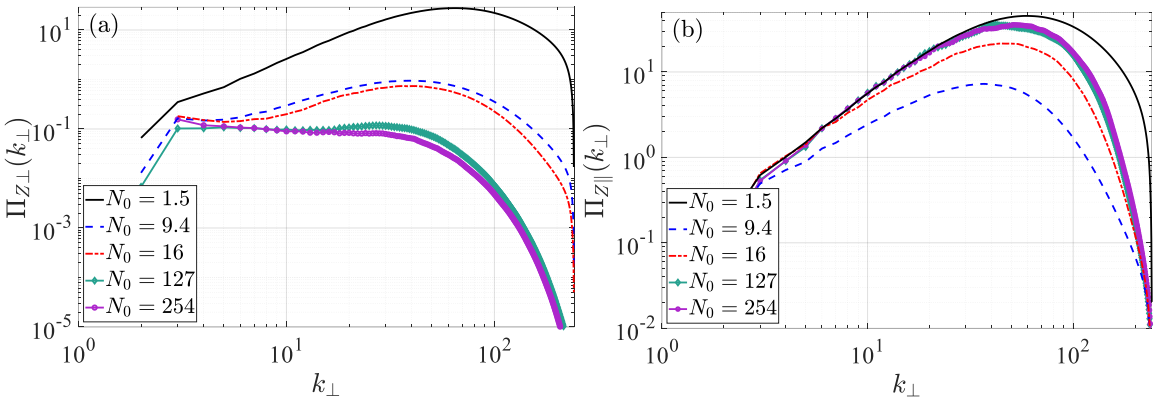

Figure 3.10. Perpendicular (a) and parallel (b) components of the enstrophy flux as function of $k_\perp$ for the range of the interaction parameter from low, $N_0 = 1.5$, to high $N_0 = 254$.

3.3 Energy spectra in strong magnetic fields and comparison with 2D turbulence

Kraichnan (1971) has shown that the k^{-3} energy spectrum in the enstrophy cascade range should have a logarithmic correction. Using our notations of the 2D spectrum in the normal plane, the corrected form is:

$$E_\perp(k_\perp) = C_\perp \eta_\perp^{2/3} k^{-3} \ln(k_\perp / k_{min})^{-1/3}, \qquad (3.10)$$

where $C_\perp$ is a dimensionless constant, $\eta_\perp$ is the rate of enstrophy transfer, and $k_{min}=1$ marks the bottom of the range where energy is injected. Using the mean value of the enstrophy flux in the range $3 \le k \le 20$ where $\Pi_{Z\perp}(k_\perp)$ is nearly constant, we found that the best fit of the DNS-derived spectrum to the form (3.10) is obtained with $C_\perp \simeq 1$ (see Figure 3.7(a)). The Lagrangian renormalized approximation (LRA) model yields $C_\perp \simeq 1.44$ (Kaneda, 1987), which is quite close to our estimate. Gotoh (1998) found from DNS that $C_\perp$ is of the order of 1 but increases with the microscale Reynolds number. Summarizing all the above results, i.e., perfect fit of the spectrum $E_\perp(k_\perp)$ to the theoretical form (3.10), correct spectral amplitude, nearly constant enstrophy

flux, and zero energy flux in the normal plane, it can be concluded that in a strong field ($N_0 \sim 120$ and higher) the turbulence attains a quasi-2D state.

In the remainder of this section, we verify that the properties of u_3, the velocity component parallel to B, are consistent with quasi-2D dynamics. At large N_0, the turbulent field is almost independent of the vertical coordinate, i.e., $\partial/\partial z = 0$. Consequently, equation (1.27) for u_3 turns into the equation of a passive scalar advected by the perpendicular flow components $\mathrm{u}_\perp = (u_1, u_2)$, as follows:

$$\frac{\partial u_3}{\partial t} + \mathrm{u}_\perp \cdot \nabla_\perp u_3 = \nu \nabla_\perp^2 u_3 , \tag{3.11}$$

where $\nabla_\perp$ and $\nabla_\perp^2$ are the perpendicular gradient and Laplacian, respectively. It is known that for the enstrophy cascade of 2D turbulence, the spectrum of scalar variance in the inertial-convective range follows a k^{-1} law (Lesieur and Herring, 1985; Gotoh, 1989). We compare this spectrum with the 2D energy spectrum of u_3, $E_{\|}(k_\perp)$, at $N_0 \geq 127$. The theoretical spectrum in our notations is:

$$E_{||}(k_\perp) = C_{||} \varepsilon_{||} \eta_\perp^{-1/3} k_\perp^{-1} \ln(k_\perp / k_{min})^{-1/3}, \tag{3.12}$$

where $\varepsilon_{\|}$ is the rate of energy flux $\Pi_{E\|}(k_\perp)$ in the range of scales where it is nearly constant (see Figure 3.9 (b)). The dimensionless constant $C_{\|}$ was set to 0.85, and good agreement with (3.12) was obtained (Figure 3.7 (b)). Gotoh (1989) studied passive scalar diffusion in 2D turbulence using the LRA model and found $C_{\|} = 0.561$, a value consistent with our estimate.

3.4 Viscous and Joule energy dissipation rates

In this section, the viscous and Joule dissipation rates of the perpendicular (horizontal) and parallel (vertical) velocity components are discussed. The viscous energy dissipation rates of the perpendicular ($\varepsilon_{h\nu}(k)$) and parallel ($\varepsilon_{3\nu}(k)$) velocity components in the interval of scales (k, ∞) are defined as follows:

$$\varepsilon_{h\nu}(k) = \nu \left\langle \int_k^\infty dq \iint_{S(q)} \left(\left|u_1(\mathrm{q})\right|^2 + \left|u_2(\mathrm{q})\right|^2 \right) q^2 \frac{d\sigma}{(2\pi)^3} \right\rangle, \tag{3.13}$$

$$\varepsilon_{3\nu}(k) = \nu \left\langle \int_k^\infty dq \iint_{S(q)} \left|u_3(\mathrm{q})\right|^2 q^2 \frac{d\sigma}{(2\pi)^3} \right\rangle, \tag{3.14}$$

where $S(q)$ is a spherical shell of radius q. The Joule energy dissipation rate for the perpendicular ($\varepsilon_{hJ}(k)$) and parallel ($\varepsilon_{3J}(k)$) components are:

$$\varepsilon_{hJ}(k) = \tau_J^{-1} \left\langle \int_k^\infty dq \iint_{S(q)} \left(\left|u_1(\mathrm{q})\right|^2 + \left|u_2(\mathrm{q})\right|^2 \right) \frac{q_z^{\,2}}{q^2} \frac{d\sigma}{(2\pi)^3} \right\rangle, \tag{3.15}$$

$$\varepsilon_{3J}(k) = \tau_J^{-1} \left\langle \int_k^\infty dq \iint_{S(q)} \left|u_3(\mathrm{q})\right|^2 \frac{q_z^{\,2}}{q^2} \frac{d\sigma}{(2\pi)^3} \right\rangle. \tag{3.16}$$

The Joule dissipation acts most strongly in the region near the Joule cone axis k_z, where $\cos^2(\theta) = (k_z/k)^2 \approx 1$ (supported as well by Figure 3.5). The Joule dissipation is zero at $\theta = \pi/2$. Thus, unlike the previous analysis that was done in terms of the perpendicular wavenumber $k_\perp$, in this section, the dissipation components are investigated in terms of the spherical wavenumber k. The dissipation dependency on the angle θ is discussed in section 3.9.

Modifications of the viscous and Joule energy dissipation rates by the magnetic field are presented in Figure 3.11. As expected, the Joule dissipation acts

most strongly in the range of large scales (Figure 3.11 (c) and (d)), where the contribution of small θ is dominant. In a weak magnetic field, $N_0 = 1.5$, the Joule dissipation is twice larger than the viscous one for every velocity component, perpendicular (Figure 3.11 (a) and (c)) and parallel (Figure 3.11 (b) and (d)). Considerable anisotropization occurs at higher interaction parameters, $N_0 \geq 9.4$. The viscous and Joule dissipations of u_1 and u_2 monotonically decrease with increasing N_0, whereas the dissipations of u_3 vary with the field non monotonically. The viscous dissipation of u_3 decreases when N_0 grows from 1.5 to 9.4, and then monotonically increases with further amplification of the magnetic field. The behavior of Joule dissipation of u_3 is opposite: it increases when N_0 goes from 1.5 to 9.4, and then monotonically decreases with increasing field. At high interaction parameters, $N_0 \geq 127$, the perpendicular viscous dissipation and the perpendicular and parallel Joule dissipations become negligible. Recall, that at such a magnetic field strength the flow is quasi-2D, and the energy flux in the normal plane completely degenerates (Figure 3.9 (a)); therefore, no energy dissipation can occur in the perpendicular component. The parallel component becomes a passive scalar with a direct energy cascade; hence, the viscous dissipation must occur in this component. In quasi-2D turbulence, most of the energy is concentrated in the perpendicular plane, where $\theta = \pi/2$, and thus the viscous dissipation overwhelms the Joule one (Figure 3.11 (b) and (d)).

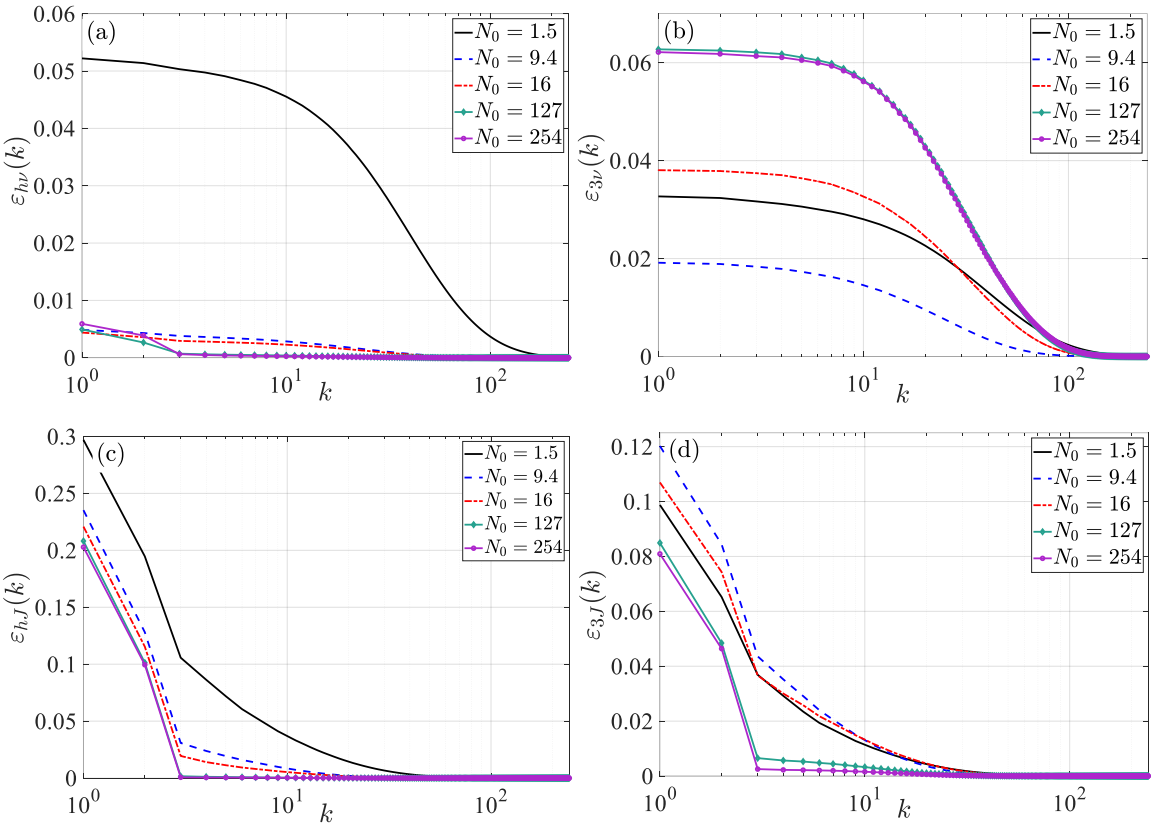

Figure 3.11. Modification of viscous and Joule components of horizontal ((a) and (c)) and vertical ((b) and (d)) energy dissipation rates with increasing magnetic field strength. Top panel - viscous dissipation; bottom panel - Joule dissipation.

3.5 Enstrophy dissipation rate

Similarly to the energy dissipation rate, the viscous and Joule parts of enstrophy dissipation rates of the vertical and horizontal vorticity components are defined as follows:

$$\eta_{3\nu}(k) = \nu \left\langle \int_k^\infty dq \iint_{S(q)} \left|\omega_3(\mathrm{q})\right|^2 q^2 \frac{d\sigma}{(2\pi)^3} \right\rangle, \tag{3.17}$$

$$\eta_{1\nu}(k) = \eta_{2\nu}(k) = \nu \left\langle \int_k^\infty dq \iint_{S(q)} \left|\omega_1(\mathrm{q})\right|^2 q^2 \frac{d\sigma}{(2\pi)^3} \right\rangle, \tag{3.18}$$

$$\eta_{3J}(k) = \tau_J^{-1} \left\langle \int_k^\infty dq \iint_{S(q)} \left|\omega_3(\mathrm{q})\right|^2 \frac{q_z^{\,2}}{q^2} \frac{d\sigma}{(2\pi)^3} \right\rangle, \tag{3.19}$$

$$\eta_{1J}(k) = \eta_{2J}(k) = \tau_J^{-1} \left\langle \int_k^\infty dq \iint_{S(q)} \left|\omega_1(\mathrm{q})\right|^2 \frac{q_z^{\,2}}{q^2} \frac{d\sigma}{(2\pi)^3} \right\rangle. \tag{3.20}$$

Note, that at large N_0 the vertical and horizontal enstrophy components are $Z_3 = \left|\omega_3\right|^2 = \left|\frac{\partial u_2}{\partial x} - \frac{\partial u_1}{\partial y}\right|^2$ and $Z_h = \left|\nabla_h u_3\right|^2$ respectively. The enstrophy dissipation components for various values of the interaction parameters are shown in Figure 3.12 (a) – (d). While the dissipations of $|\omega_3|^2$, viscous and Joule, and the horizontal Joule dissipation $\eta_{hJ}(k) \equiv \eta_{1J}(k) + \eta_{2J}(k)$ decrease with increasing magnetic field, the horizontal viscous dissipation $\eta_{h\nu}(k) \equiv \eta_{1\nu}(k) + \eta_{2\nu}(k)$ behaves non monotonically, decreases with N_0 in the interval (1.5, 9.4) but grows with N_0 at N_0>9.4.

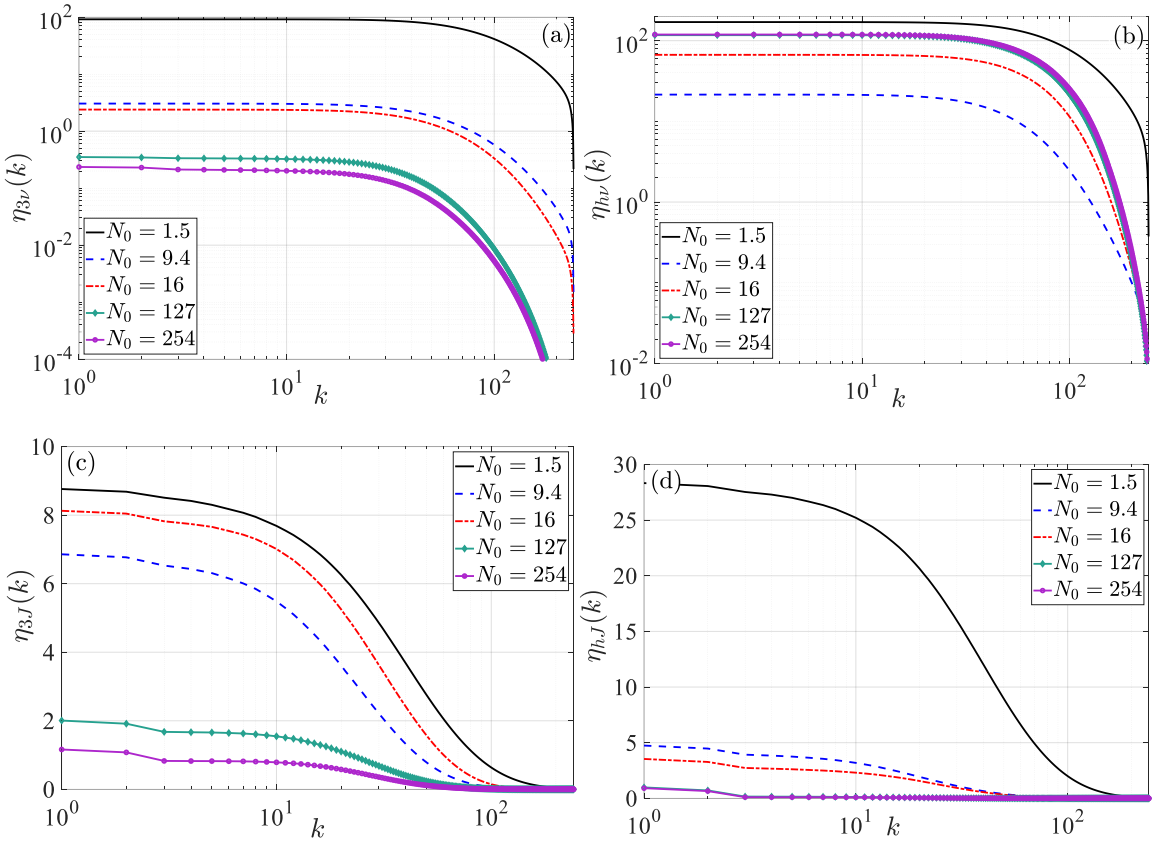

Figure 3.12. Modification of viscous and Joule components of vertical ((a) and (c)) and horizontal ((b) and (d)) enstrophy dissipation rates with increasing magnetic field strength. Top panel - viscous dissipation; bottom panel - Joule dissipation.

3.6 Enstrophy production

As shown in section 3.2, the perpendicular enstrophy flux $\eta_\perp$ at strong magnetic fields, at $N_0 \gtrsim 120$, is constant in the inertial range (Figure 3.10 (a)). The vertical enstrophy dissipation at this N_0 is almost negligible (Figure 3.12 (a) and (c)), thus the enstrophy production is also expected to be negligible, in accord with 2D dynamics of the flow. The horizontal enstrophy production $\mathcal{P}_h(k)$ in the interval (0, k) is given by the following expression,

$$\mathscr{P}_h(k) = -\Re\left\langle \iiint_{V(k)} \omega_3^*(\mathrm{k}, t \mid k)\mathcal{F}\left(\omega_j \frac{\partial u_3}{\partial x_j}\right)\frac{d\mathrm{k}}{(2\pi)^3}\right\rangle, \tag{3.21}$$

and is shown in Figure 3.13 (a). As expected, the horizontal enstrophy production decreases with increasing magnetic field strength, becoming negligibly small at $N_0 \gtrsim 120$.

The vertical enstrophy production $\mathscr{P}_3(k)$ in the interval (0, k) is given by the following expression,

$$\mathscr{P}_3(k) = -\Re\left\langle \iiint_{V(k)} \omega_i^*(\mathrm{k}, t \mid k)\mathcal{F}\left(\omega_j \frac{\partial u_i}{\partial x_j}\right)\frac{d\mathrm{k}}{(2\pi)^3}\right\rangle, \quad i \neq 3, \tag{3.22}$$

and is presented in Figure 3.13 (b), which shows that $\mathscr{P}_3(k)$ increases with k at all values of N_0. The dependence on N_0 is not monotonic, similarly to the behavior of the horizontal viscous enstrophy dissipation. At large N_0, $\mathscr{P}_3(k)$ and the parallel enstrophy flux $\eta_{\parallel}(k_{\perp})$ are linked to the passive scalar u_3. Both quantities increase in the convective-inertial range, while the horizontal viscous $\eta_{hv}(0) - \eta_{hv}(k)$ and Joule $\eta_{hJ}(0) - \eta_{hJ}(k)$ dissipations are negligibly small in this range (Figure 3.12 (b) and (d)). This implies that the flux $\eta_{\parallel}(k_{\perp})$ is balanced by the production $\mathscr{P}_3(k)$. Note that at a strong field, the dominant contribution to $\mathscr{P}_3(k)$ comes from the region of $\theta \approx \pi/2$, which allows one to consider the balance between $\eta_{\parallel}(k_{\perp})$ and $\mathscr{P}_3(k)$.

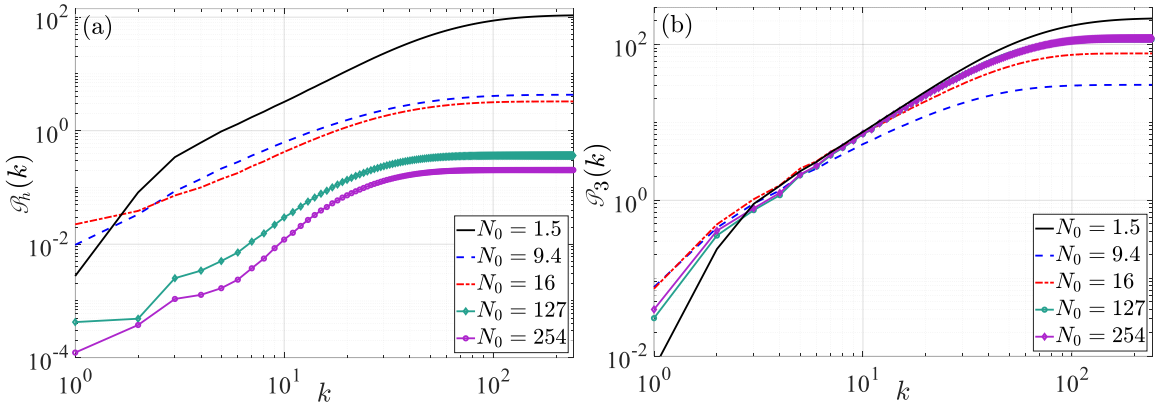

Figure 3.13. Modification of horizontal (a) and vertical (b) components of the enstrophy production with increasing magnetic field strength.

Our analyses show that in a strong magnetic field turbulent motion in the normal plane corresponds to the 2D enstrophy cascade, while the parallel fluctuations resemble turbulent diffusion of a passive scalar. This resemblance raises questions regarding the energy source for the scalar flux and the mechanism of energy transfer to the parallel velocity component.

3.7 Source of the parallel energy flux

3.7.1 Role of parallel pressure flux

Pressure, as a 'guardian' of flow incompressibility, causes a redistribution of energy between the velocity components and may thus be a possible source of the parallel energy flux. Another possibility is that there is a direct injection of energy $\varepsilon_{\parallel}$ by an external stirring force. The magnitude of the transfer to the parallel component via pressure, $\Pi_{P\parallel}(k_\perp)$, from the spectral region inside the cylinder of radius $k_\perp$ outward, is given by the following integral:

$$\Pi_{P_\parallel}(k_\perp) = -\Im\left\langle \iiint_{V(k_\perp)} u_3^*(\mathrm{k},t \mid k_\perp) k_3 P(\mathrm{k},t) \frac{d\mathrm{k}}{(2\pi)^3} \right\rangle, \tag{3.23}$$

where the symbol $\Im$ designates the imaginary part of the expression. Utilizing the incompressibility equation, the pressure is computed as:

$$P(k,t) = \frac{-ik_i}{k^2}\mathcal{F}\left(u_j(\mathrm{x},t)\frac{\partial u_i(\mathrm{x},t)}{\partial x_j}\right). \tag{3.24}$$

Modification of $\Pi_{P\|}(k_\perp)$ by magnetic friction is shown in Figure 3.14. Suppression of flow derivatives in the direction of the magnetic field with increasing field strength leads to degeneration of $\Pi_{P\|}(k_\perp)$. In a strong field, N_0 = 254, its maximal value is close to 5×10^{-4}, which is smaller than the energy flux $\varepsilon_\|$ = 0.065 (see Figure 3.9 (b)) by two orders of magnitude. Therefore, the pressure flux cannot be a meaningful source of the energy supplied to the parallel flow component. This leaves a direct injection of energy by an external force as the only possible source of energy.

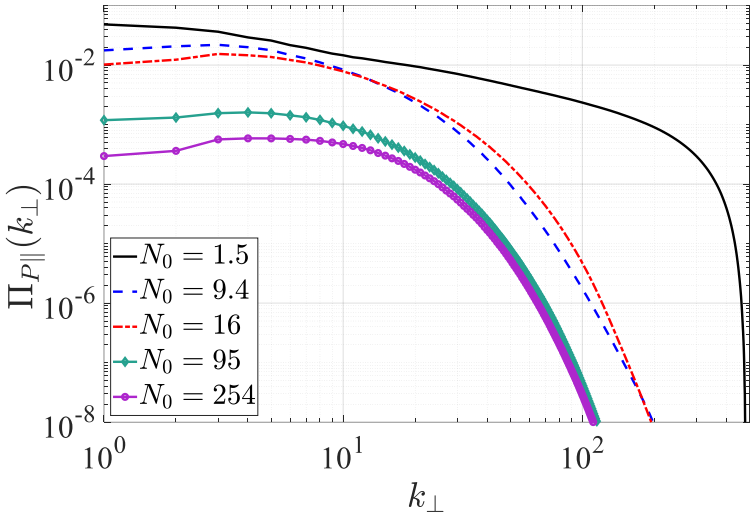

Figure 3.14. Modification of the pressure flux $\Pi_{P\|}(k_\perp)$ with increasing magnetic field strength.

3.7.2 Role of an external force in generating the parallel energy flux

The last result is not surprising, since the equation for u_3 approaches a passive scalar equation not containing pressure as the magnetic field strength increases (see

equation (3.11)). A more interesting result is that the turbulent state in a strong field depends on the anisotropy of external forcing and, thus, is not universal. To illustrate this point, we conducted simulations with pure 2D two component (2D-2C) forcing and 3D two component (3D-2C) forcing. It is obvious that without any 3D disturbance, the 2D-2C simulations result in a pure 2D turbulent field. Thus, a small amplitude 3D-2C initial field was generated. Non-magnetic simulations with 2D-2C forcing quickly evolve into 3D turbulence characterized by an isotropic Kolmogorov -5/3 inertial range, independent of the forcing details and the initial conditions. However, if a strong magnetic field is applied, the simulations result in a quasi-2D turbulent field with a small parallel velocity component that does not adhere to a well-defined power scaling as seen in Figure 3.15.

Comparing the energy spectra shown in Figure 3.7 and Figure 3.15, we conclude that the perpendicular spectra in 3D-3C, 3D-2C, and 2D-2C simulations are nearly identical, but the parallel spectra in simulations with two-componential forcing are smaller by a few orders of magnitude than those with 3D-3C forcing.

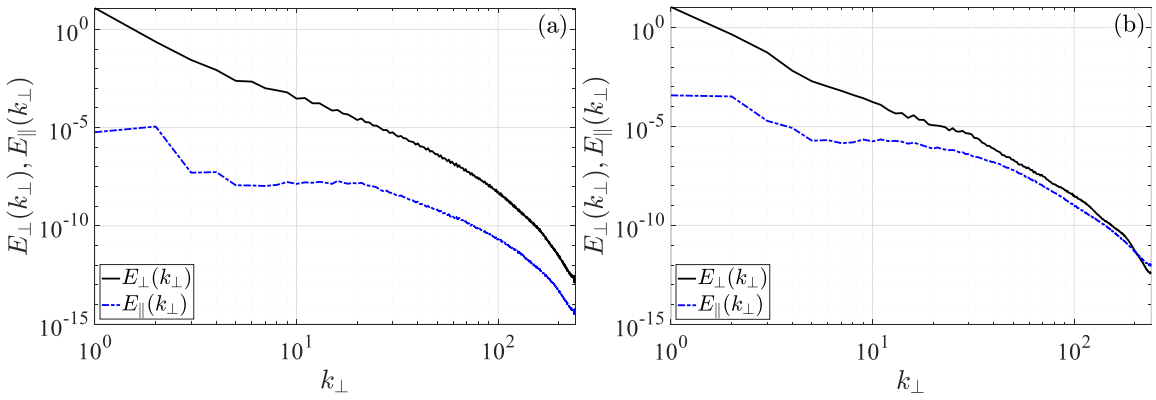

Figure 3.15. Perpendicular and parallel energy spectra in simulations with (a) 2D-2C and (b) 3D-2C forcing in a strong magnetic field.

3.8 Dependence on the Reynolds number

As shown in the previous sections, at large values of the interaction parameter, the flow becomes quasi-2D and turbulence characteristics do not change with further increases of the magnetic field. However, what happens if the interaction parameter is kept constant while the Reynolds number is increased? With increasing R_0, smaller turbulence scales are excited. These scales may have shorter characteristic times and are thus less susceptible to the anisotropization effect of the Lorentz force. Will the quasi-2D state remain stable under these conditions? To answer this question, an additional DNS was conducted with the same interaction parameter N_0=254 as that in the previous experiment but with a higher resolution of 1024^3. Under these conditions, the viscosity decreased by factor of 3, leading to a corresponding increase in R_0 from 1730 to 5220. The spectrum obtained in the perpendicular plane is shown in Figure 3.16 together with the spectrum at R_0 = 1730. With increasing R_0, the power scaling changed from -3 to -7/3. The spectrum of the parallel component $E_{\parallel}(k_{\perp})$ retained its form (3.12) (not shown).

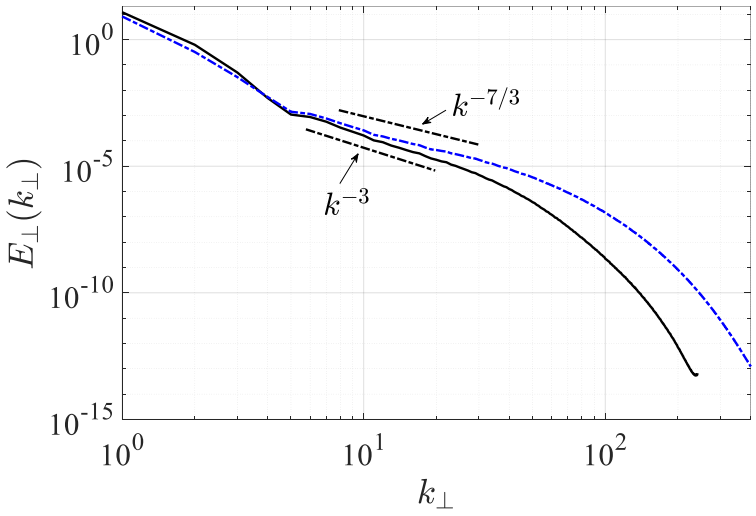

Figure 3.16. Perpendicular energy spectra at N_0=254 at two values of R_0: R_0 = 1730 (solid black line) and R_0 = 5220 (dash-dotted blue line).

We now ask: what is the physics behind the -7/3 scaling in this experiment? The -7/3 spectrum is often associated with helicity cascade (Branover *et al.,* 1994; Golbraikh *et al.,* 1998). Helicity is zero in pure 2D turbulence where the vorticity vector is perpendicular to the velocity field. However, in the 2D-3C case considered here, the vorticity has a non-zero horizontal projection due to the dependence of u_3 on x_1 and x_2, which may cause helicity flux in the normal plane. Examination of spectral amplitudes may clarify the physical mechanism governing dynamical processes leading to the -7/3 slope. If the flux of helicity Π_H is responsible for the observed spectrum, then it may be expected that the amplitude of the spectrum will be proportional to $\Pi_H^{2/3}$.

The fluxes of helicity in the perpendicular plane $\Pi_{H\perp}(k_\perp)$ and along the magnetic field $\Pi_{H\parallel}(k_\perp)$ were computed for two simulations with different settings of N_0 and R_0, namely, N_0=62, R_0=1770 and N_0=252, R_0=5220. Both simulations gave the -7/3 perpendicular and -1 parallel spectra. The fluxes were computed using the following formulas:

$$\Pi_{H\perp}(k_\perp) = -\Re\left\langle \iiint_{V(k_\perp)} \omega_i^*(\mathrm{k},t \mid k_\perp)\mathcal{F}\left(u_j \frac{\partial u_i}{\partial x_j}\right)\frac{d\mathrm{k}}{(2\pi)^3}\right\rangle,\ i \neq 3, \tag{3.25}$$

$$\Pi_{H\parallel}(k_\perp) = -\Re\left\langle \iiint_{V(k_\perp)} \omega_3^*(\mathrm{k},t \mid k_\perp)\mathcal{F}\left(u_j \frac{\partial u_3}{\partial x_j}\right)\frac{d\mathrm{k}}{(2\pi)^3}\right\rangle. \tag{3.26}$$

The results presented in Figure 3.17 (a) indicate that the fluxes in the two simulations are significantly different, but in each simulation their values are nearly constant over a wide range of scales. Notably, the perpendicular and parallel fluxes have opposite signs but almost the same magnitudes; thus, they nearly compensate for one another in the total helicity flux. This result is not surprising, since the external forcing in our simulations does not inject helicity. The energy spectra

compensated by $\Pi_H^{2/3} k^{-7/3}$ are shown in Figure 3.17 (b). The compensated spectra are nearly constant in the range of scales between forcing and dissipation. The dimensionless constants in both simulations are close to one another, thus supporting our conjecture of a helicity cascade.

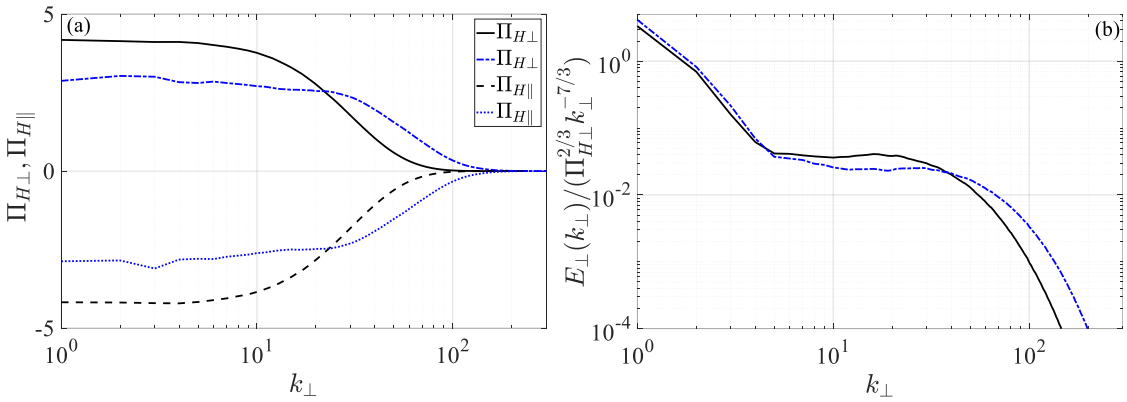

Figure 3.17. (a) Perpendicular and parallel helicity fluxes and (b) compensated energy spectra for N_0=62 with n=512^3 (solid and dashed black lines) and N_0=252 with n=1024^3 (dash-dotted and dotted blue lines).

Finally, we verified that by further increasing magnetic field at constant R_0 the enstrophy cascade range with scaling (3.10) can be restored, replacing the helicity cascade. Figure 3.18 shows the compensated energy spectrum $\tilde{E}_\perp(k_\perp) = E_\perp(k_\perp) \,/\, \left(\eta_\perp^{\,2/3} k^{-3} \ln(k_\perp \,/\, k_{min})^{-1/3}\right)$ for two simulations with different settings of N_0 and R_0: N_0=254, R_0=1730 and N_0=806, R_0=5100 respectively. Both spectra are nearly constant in the inertial range, and the dimensionless constant $C_\perp$ is close to 1 in both simulations.

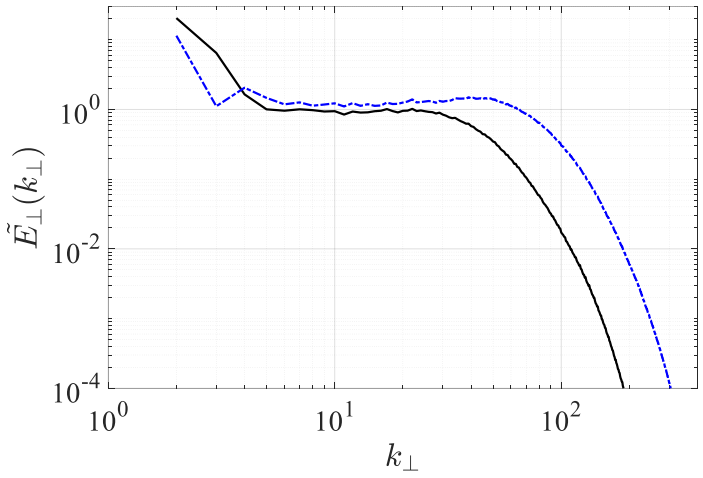

Figure 3.18. Compensated energy spectrum for N_0=254 with n=512³ (solid black line) and N_0=806 with n=1024³ (dash-dotted blue line).

3.9 Angular distribution of energy and energy dissipation rate

The anisotropy of QS-MHD turbulence increases with increasing magnetic field strength. $E_\perp(k_\perp)$ and $E_\parallel(k_\perp)$ spectra describe anisotropic spectral behavior at the strongest field when the flow attends the quasi-2D state. The transition to this state could be viewed in terms of angular energy distribution. The process of angular energy redistribution with increasing field could be traced using θ-dependent energy spectra $E_h(k_\perp,k_\parallel)$ and $E_3(k_\perp,k_\parallel)$ obtained by averaging of energy densities $\left|u_1(k_\perp,k_\parallel,\varphi)\right|^2+\left|u_2(k_\perp,k_\parallel,\varphi)\right|^2$ and $\left|u_3(k_\perp,k_\parallel,\varphi)\right|^2$, respectively, over thin spherical rings with radius k and polar angle θ (see Figure 3.19). Statistical independence of the energies of azimuthal angle φ was taken into account.

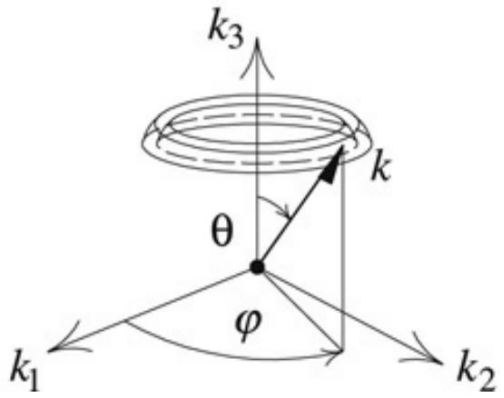

Figure 3.19. One spherical ring in cartesian and polar spherical coordinate systems (reproduced from Burattini *et al.* (2008b)).

The modifications of $E_h(k_\perp,k_\parallel)$ and $E_3(k_\perp,k_\parallel)$ for various interaction parameters are shown in Figure 3.20. $E_3(k_\perp,k_\parallel)$ (right panel) is zero at $k_\perp = 0$ for any $k_\parallel$. This result is due to the continuity equation since $k_\perp = 0$ brings about $k_3 u_3 = 0$. In a weak magnetic field, $N_0 = 1.5$, the energy distribution is almost isotropic, and the directional anisotropization is barely noticeable (Figure 3.20 (a)). With increasing magnetic field, at $N_0 \geq 16$, the energy of the modes with large k_3 is depleted due to the Joule friction (Figure 3.20 (c)-(f)). At $N_0 = 16$, the energy spans anisotropically over 3D space and is not concentrated on the plane normal to B. The gradients in the $k_\perp$ direction become sharp, while the contours of constant energy are shaped into approximately cylindrical structures with the k_3 axis. Finally, at $N_0 = 127$, the energy is almost completely concentrated in the normal plane ($\theta = \pi/2$), i.e., the turbulence becomes quasi-2D. A similar trend of the spectral distribution was obtained in previous studies (Burattini *et al.,* 2008b; Reddy *et al.,* 2014).

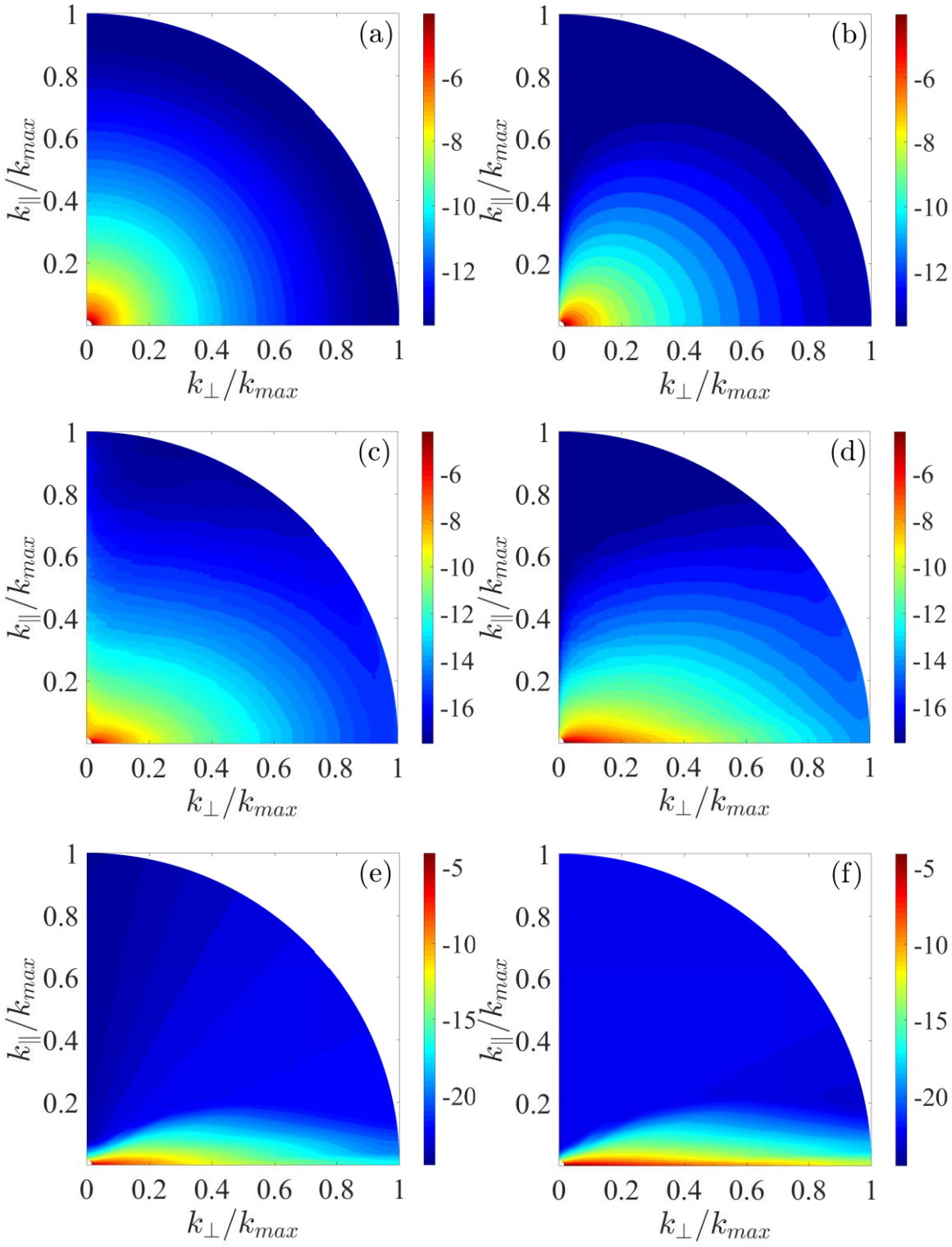

Figure 3.20. Angular distribution of $\log(E_h(k_\perp,k_\parallel))$ (left panels) and $\log(E_3(k_\perp,k_\parallel))$ (right panels) for: N_0=1.5 (a) and (b); N_0=16 (c) and (d); N_0=127 (f) and (e).

The results shown in Figure 3.20 provide an essential information on the energy distribution in the Fourier space. The anisotropy development is due to Joule dissipation, which depends on θ explicitly, due to the factor $\cos^2(\theta)$, and implicitly, due to anisotropic energy distribution. The viscous energy dissipation is proportional to the energy distribution and thus implicitly depends on θ. The angular distributions of the Joule dissipation components are:

$$\varepsilon_{hJ}(k_\perp, k_\parallel) = 2\tau_J^{-1} E_h(k_\perp, k_\parallel)\cos^2\theta, \tag{3.27}$$

$$\varepsilon_{3J}(k_\perp, k_\parallel) = 2\tau_J^{-1} E_3(k_\perp, k_\parallel)\cos^2\theta. \tag{3.28}$$

These distributions are shown in Figure 3.21 for N_0 = 1.5, 16, and 127. Anisotropy of Joule dissipation is evident even in a weak magnetic field, N_0 = 1.5, at which the energy distribution was nearly isotropic, but the dissipation concentrates near the k_3 axis (θ = 0) due to the factor $\cos^2(\theta)$. At higher interaction parameters, $N_0 \geq 16$, $\varepsilon_{hJ}(k_\perp, k_\parallel)$ and $\varepsilon_{3J}(k_\perp, k_\parallel)$ are identically zero at $\theta = \pi/2$ due to the factor $\cos^2(\theta)$ but are maximal in the vicinity of this angle. Note, that the energy distributions $E_h(k_\perp, k_\parallel)$ and $E_3(k_\perp, k_\parallel)$ are maximal at $\theta = \pi/2$.

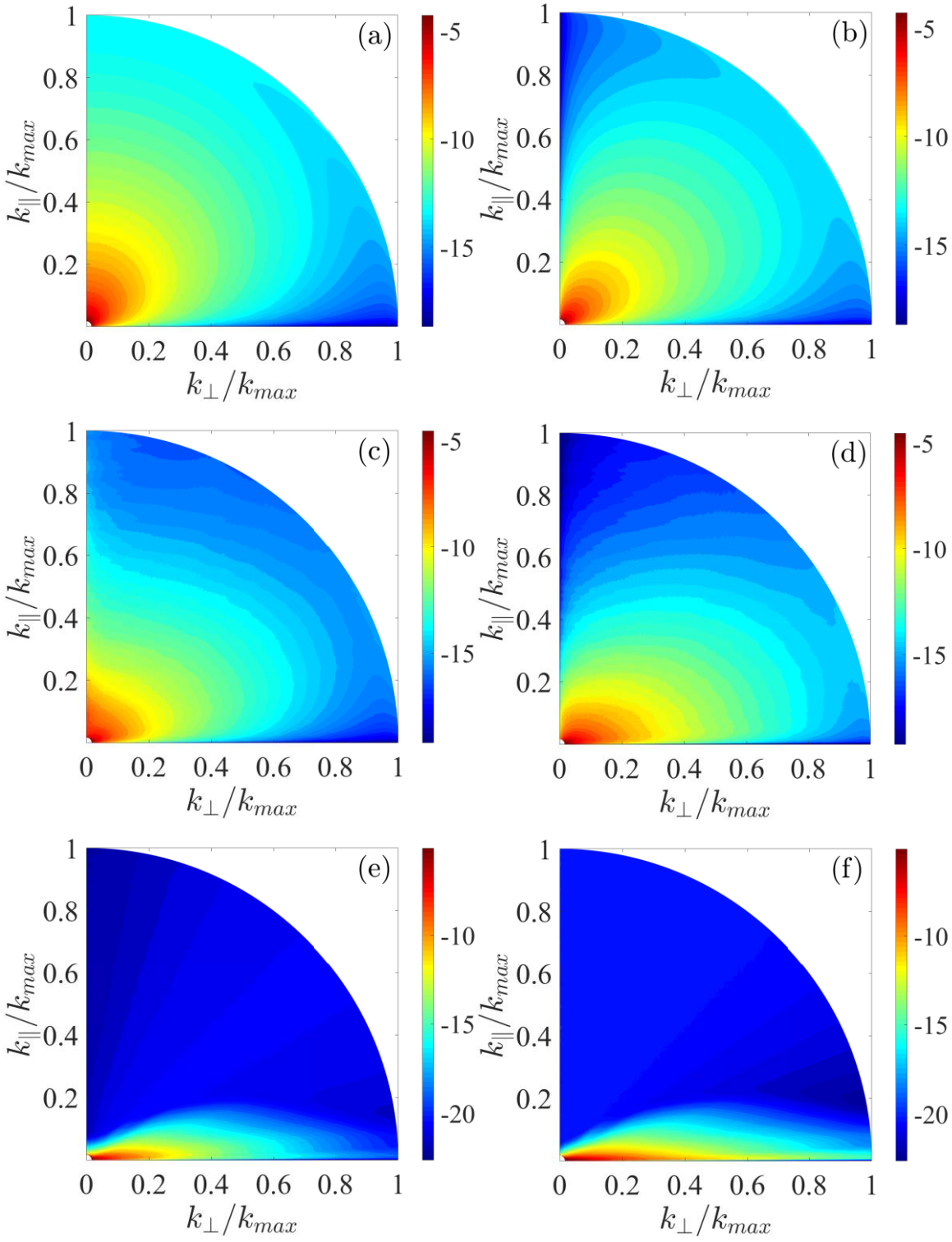

Figure 3.21. Angular distribution of $\log(\varepsilon_{hJ}(k_\perp,k_\parallel))$ (left panels) and $\log(\varepsilon_{3J}(k_\perp,k_\parallel))$ (right panels) for: N_0=1.5 (a) and (b); N_0=16 (c) and (d); N_0=127 (f) and (e).

3.10 Skewness of the longitudinal velocity derivative

So far, turbulence anisotropization was studied in spectral space by computing 3D, 2D and 1D energy spectra, energy and enstrophy fluxes and dissipations. In the remainder of this chapter, turbulence properties in physical space, that may shed additional light on the anisotropization development, will be investigated.

The skewness of the longitudinal velocity derivative S_0 is defined as follows:

$$S_0 = \frac{\left\langle \left(\partial u_1 / \partial x_1 \right)^3 \right\rangle}{\left\langle \left(\partial u_1 / \partial x_1 \right)^2 \right\rangle^{3/2}}. \tag{3.29}$$

The subscript "0" indicates that all scales are accounted for in the computation of skewness. S_0 is an important parameter, most relevant to small turbulence scales. For random noise, $S_0 = 0$, while for homogeneous and isotropic turbulence, the values of $-S_0$ were measured in the range $0.3 - 0.5$ in laboratory experiments and computer simulations at low Re, rising to about 0.7 for high Re (see for example (Frisch, 1995; Gotoh *et al.,* 2002) and references therein).

An important property of S_0 is that in homogeneous and isotropic turbulence it represents a nondimensional measure of the rate of enstrophy production due to vortex stretching (Batchelor and Townsend, 1947):

$$\left\langle \omega_i \omega_j \frac{\partial u_i}{\partial x_j} \right\rangle = -\frac{35}{2} S_0 \left(\frac{\varepsilon}{15\nu} \right)^{3/2}. \tag{3.30}$$

Since the vortex stretching term vanishes in two-dimensional turbulence, the skewness is expected to be zero.

In high Re flows, the measurement of S_0 is difficult because the viscous subrange must be fully and accurately resolved. A more easily measurable parameter

is the skewness of velocity derivatives of fluctuations larger than those in the dissipation range. First attempts to derive the skewness of fluctuations belonging to the inertial range were based on the normalized longitudinal third-order structure function $S_3^{(L)}(r) / \left(S_2^{(L)}(r)\right)^{3/2}$ computed at large separation r (Garg and Warhaft, 1998; Shen and Warhaft, 2000). However, computations with large r do not accurately represent the derivatives of the inertial range scales. A more precise approach suggests filtering off the dissipation range scales followed by an exact computation of the longitudinal derivative of the remaining velocity field (Sukoriansky *et al.,* 2018). This approach is flexible as it allows selecting the subrange scales of interest. The effect of the magnetic field on the skewness of different scales is presented in the following subsections. The computations are based on the method suggested by Sukoriansky *et al.* (2018).

3.10.1 Scale-dependent skewness of velocity derivative at zero magnetic field

For any cutoff wave number k_c Sukoriansky *et al.* (2018) defined the filtered velocity $\mathrm{u}\left(\mathrm{x},t \mid k_c\right)$ as the physical space velocity with all Fourier modes $|\mathrm{k}|>k_c$ set to 0:

$$\mathrm{u}\left(\mathrm{x},t \mid k_c\right) = \mathscr{F}^{-1}\left(\mathrm{u}\left(\mathrm{k},t\right) H\left(k_c - |\mathrm{k}|\right)\right). \tag{3.31}$$

In the anisotropic case more information is acquired using the one-directional longitudinal filtering of velocity component u_i (i=1,2,3) by setting to 0 all Fourier modes $|k_i|>k_{1c}$:

$$u_i\left(x_i,t \mid k_{1c}\right) = \mathscr{F}^{-1}\left(u_i\left(\mathrm{k},t\right) H\left(k_{1c} - |k_i|\right)\right). \tag{3.32}$$

We denote the scale-dependent skewness of each velocity component u, v, w as $S_{kc}^u, S_{kc}^v, S_{kc}^w$, respectively. Similar notations $S_{1c}^u, S_{1c}^v, S_{1c}^w$ are used for the one-directional

scale-dependent skewness. According to (3.29), S_{kc}^{u} and S_{1c}^{u} are defined with the original velocity replaced by the filtered velocities, (3.31) and (3.32):

$$S_{kc}^{u} = \frac{\left\langle \left(\partial u_1 \left(\mathrm{x}, t \middle| k_c \right) / \partial x_1 \right)^3 \right\rangle}{\left\langle \left(\partial u_1 \left(\mathrm{x}, t \middle| k_c \right) / \partial x_1 \right)^2 \right\rangle^{3/2}}, \qquad S_{1c}^{u} = \frac{\left\langle \left(\partial u_1 \left(\mathrm{x}, t \middle| k_{1c} \right) / \partial x_1 \right)^3 \right\rangle}{\left\langle \left(\partial u_1 \left(\mathrm{x}, t \middle| k_{1c} \right) / \partial x_1 \right)^2 \right\rangle^{3/2}} \tag{3.33}$$

S_{kc}^{v}, S_{kc}^{w} are defined similarly with u_1 replaced by u_2 and u_3, respectively.

Scale-dependent values of S_{kc}^{u} and S_{1c}^{u} at zero magnetic field for simulations with 1024^3 grid points are shown in Figure 3.22. Since the turbulence is isotropic, the skewness of other velocity components is the same. In the inertial range, the obtained values $-S_{kc}^{u} \approx 0.33$ and $-S_{1c}^{u} \approx 0.2$ are very close to the theoretical predictions and the results of atmospheric measurements presented in (Sukoriansky *et al.,* 2018). These inertial range values correspond to the filter scale larger than 10, while the energy spectrum inertial range starts at $k \gtrsim 4$ (Figure 3.1 dash-dotted blue line). This result was explained in Sukoriansky *et al.* (2018) by the fact that skewness is not a local parameter such that at least one decade of larger scales contributes to its value at the filter scale. Thus, a sizeable inertial range is required for skewness computations. In the dissipation range, when all the turbulent scales are resolved (i.e., S_{kc}^{u} and S_{1c}^{u} are equal to S_0), the skewness value is 0.56. This value is consistent with published experimental and numerical results.

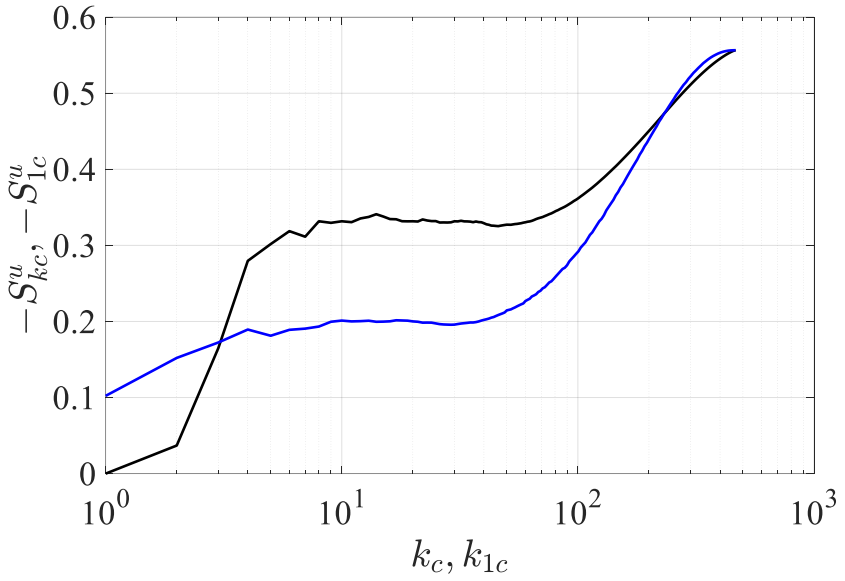

Figure 3.22. Scale-dependent skewness S^u_{kc} (black) and S^u_{1c} (blue) at $N_0 = 0$.

3.10.2 Anisotropization of scale-dependent skewness of velocity derivative by a magnetic field

The scale-dependent skewness of the perpendicular velocity component S^u_{kc} and S^u_{1c}, and the parallel velocity component S^w_{kc} and S^w_{1c} are shown in Figure 3.23 (the sign is reversed for convenience). The change of S^u_{kc} and S^u_{1c}, with the increasing magnetic field, is not monotonic. At a weak magnetic field, N_0=1.5, $-S^u_{kc}$ rises above the non-magnetic values, reaching the maximal value of 0.7 at the dissipation scale. With increasing magnetic field, at $N_0 \geq 9.4$, the trend changes, and $-S^u_{kc}$, $-S^u_{1c}$ decrease, whereas the values at large scales (small filtering wave number) decrease first and strongest. In a strong magnetic field, $N_0 \geq 127$, S^u_{kc} and S^u_{1c} approach zero at all scales as expected for quasi-2D turbulence (Boffetta and Ecke, 2012). The skewness of the parallel component $-S^w_{kc}$, as well as $-S^w_{1c}$, show a tendency of monotonic decrease with increasing magnetic field, becoming negative at high interaction parameter, $N_0 \geq 127$.

We did not find published results on the skewness of 2D passive scalar. DNS verification of the sign and values of this quantity is an appealing task for future research.

An interesting question arises: Does equation (3.30) hold for anisotropic QS-MHD turbulence? To answer this question, we computed the ratio of two sides of the equation as applied to the perpendicular velocity component:

$$C_S^u = \frac{\mathscr{P}_h \big/ S_0^u}{-\frac{35}{2}\left(\frac{\varepsilon_{h\nu}}{15\nu}\right)^{3/2}}. \tag{3.34}$$

Table 3.2 summarizes the computed values of C_s^u for various N_0. For the non-magnetic case, C_s^u is very close to 1 as expected for isotropic 3D turbulence. The values of C_s^u change non-monotonically with increasing magnetic field but remain $O(1)$ up to N_0=16 at least. At larger N_0, when the flow becomes quasi-2D, C_s^u is negative, approaching -2.8 at the highest N_0. Recall that the enstrophy production at the strong field is very small, such that $C_s^u = -2.8$ represents the ratio of infinitesimally small values.

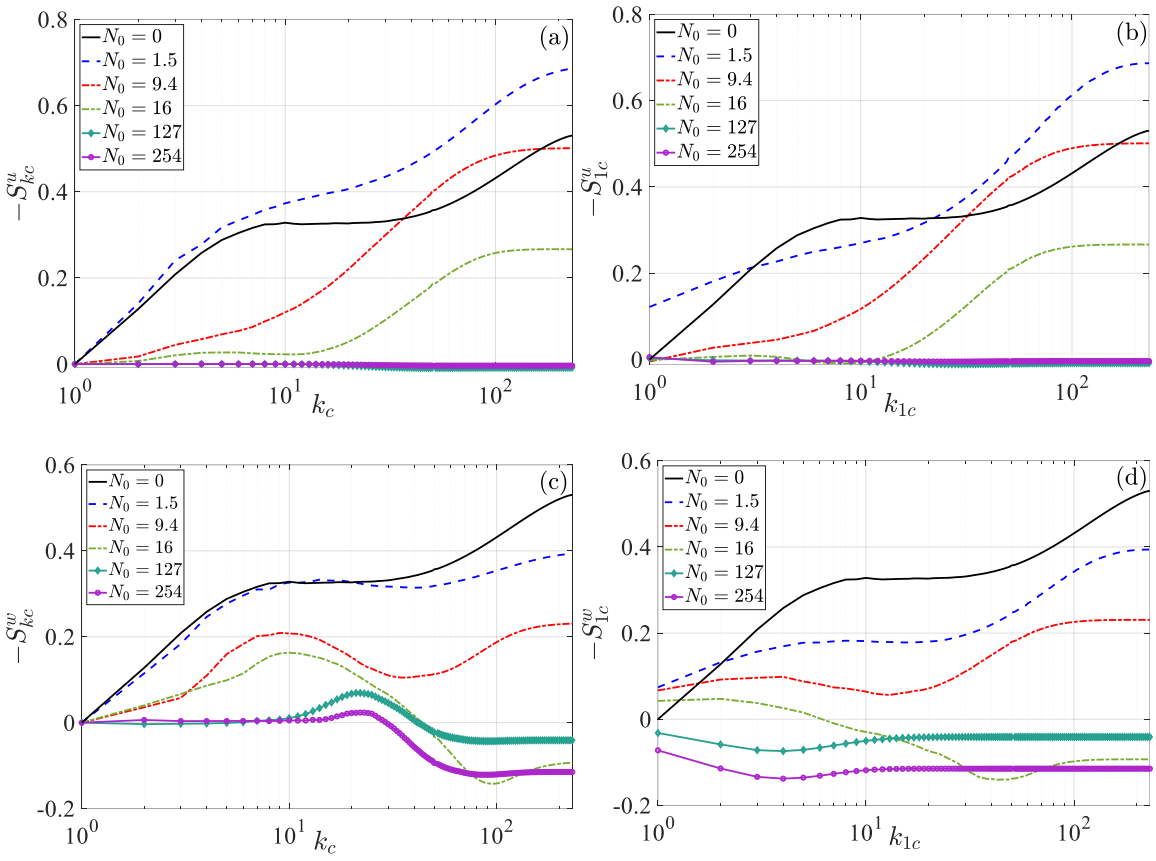

Figure 3.23. Longitudinal scale-dependent skewness for the perpendicular velocity component (a) and (b), and for the parallel velocity component (c) and (d), at various values of the interaction parameters.

Table 3.2. C_S^u and physical quantities in equation (3.34) at different values of N_0.

N_0	ε_{hv}	$\mathscr{P}_h$	S_0^u	C_s^u
0	0.44 (ε_v)	3178 ($\mathscr{P}$)	-0.53 (S_0)	1.002 (C_S)
1.5	5.23×10^{-2}	107.7	-0.687	0.639
9.4	6.2×10^{-3}	4.3	-0.501	0.858
16	5.96×10^{-3}	3.3	-0.267	1.31
127	8.6×10^{-3}	0.365	8.6×10^{-3}	-2.59
254	9.88×10^{-3}	0.203	3.6×10^{-3}	-2.8

3.11 Second and third order longitudinal velocity structure functions

Based on the self-similarity hypothesis (SSH) of Kolmogorov for homogeneous isotropic turbulence, the longitudinal structure function $S_p^{(L)}$ is proportional to $(r\varepsilon)^{p/3}$ in the inertial range (Kolmogorov, 1941b). The SSH is not applicable to anisotropic turbulence affected by external body force.

In chapter 2, the Kolmogorov relations for the second- and third-order structure functions (equations (2.14) and (2.16)) were used to examine the isotropy in the non-magnetic case. The structure functions could also be used to study the turbulence anisotropy (deviation from the K41 hypothesis) and two-dimensionality. For this purpose, the longitudinal second ($S_{u,2}^{(L)}$) and third order ($S_{u,3}^{(L)}$) structure functions of the perpendicular velocity component, defined by equation (2.15), are used.

3.11.1 Anisotropic second order structure function

Modification by a magnetic field of the normalized second order longitudinal structure function $S_{u,2}^{(L)} / (\varepsilon r)^{2/3}$ is shown in Figure 3.24. For the non-magnetic case, the plot of $S_{u,2}^{(L)} / (\varepsilon r)^{2/3}$ has a plateau with the value of ~2 over a wide range of separations rk_{diss}, as predicted by the Kolmogorov hypotheses (Kolmogorov, 1941b). This value agrees with numerous experimental observations and DNS results (see e.g., (Saddoughi and Veeravalli, 1994; Ni and Xia, 2013)).

At a weak magnetic field, $N_0 = 1.5$, $S_{u,2}^{(L)}$ becomes anisotropic in the region of large separations. At $rk_{diss}<10$, the values of $S_{u,2}^{(L)}$ merge almost perfectly with the

non-magnetic values, indicating a return to isotropy on these scales. This result is consistent with the transition from the QS-MHD -7/3 power law spectrum to the isotropic 3D spectrum at large k (Figure 3.2(a)). At higher interaction parameters, the anisotropy propagates to larger scales, and in a strong field, $N_0 \geq 127$, $S_{u,2}^{(L)} / (\varepsilon r)^{2/3}$ scales as $\sim r^{1.3}$, i.e., $S_{u,2}^{(L)} \propto r^2$ in the whole range of turbulence scales.

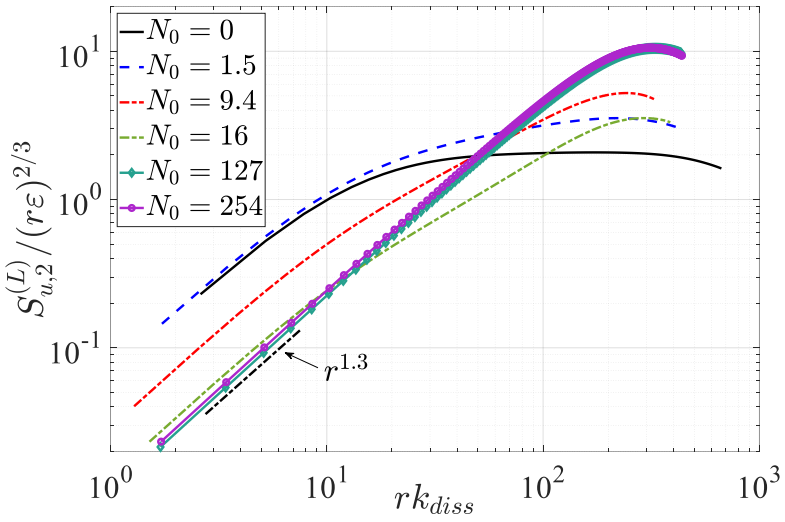

Figure 3.24. Compensated second order longitudinal struction function for various strengths of magnetic field.

To identify the modification of the scaling exponent more precisely at a weak magnetic field, we used DNS with a higher resolution of 1024^3 grid points (Figure 3.25 (a)). At large rk_{diss}, the amplification of the magnetic field strength leads to an increase of the scaling exponent from 0 at zero field to 0.26 at N_0 = 1.5, to 0.5 at N_0 = 4.9. Concurrently, at small rk_{diss}, the scaling exponent of 1.22 is observed at all field strengths.

At high interaction parameter, $N_0 \geq 127$, when $S_{u,2}^{(L)} \propto r^2$, the turbulence is quasi-2D with no energy flux in the normal plane, but with enstrophy flux $\eta_\perp$. Thus, based on dimensional considerations, $S_{u,2}^{(L)}$ was normalized by $(r^3\eta_\perp)^{2/3}$ to obtain non-

dimensional values (Figure 3.25 (b)). At small rk_{diss}, plateaus with values of 6.7 and 7.5, for $N_0 = 127$ and $N_0 = 254$, respectively, were obtained. At larger separations, the logarithmic dependence on rk_{diss} in the form $a - b\ln(rk_{diss})$ appears. The coefficients $a \approx 23.3$ and $b \approx 3.5$ for $N_0 = 127$, and $a \approx 27.5$ and $b \approx 4.2$ for $N_0 = 254$, are the best fit at large rk_{diss} (see Figure 3.25 (b)). This result agrees with the analytically derived 2nd order structure function $S_{u,2}^{(L)} = (a - b\ln(r \cdot k_{diss}))(r^3\eta_\perp)^{2/3}$ in the enstrophy cascade range (Lindborg, 1999).

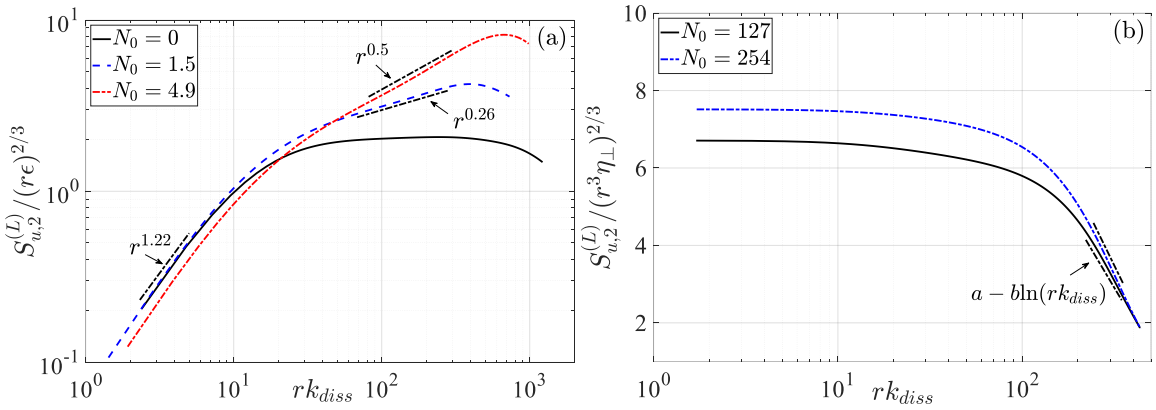

Figure 3.25. Compensated second order longitudinal structure function for weak (a) and strong (b) magnetic field.

3.11.2 Anisotropic third order structure function

Compensated third order structure function $-S_{u,3}^{(L)} / r\varepsilon$ for weak and strong magnetic fields are shown in Figure 3.26 (a) and (b), respectively. At zero field, the value 0.78, obtained in the inertial range, is close to the celebrated Kolmogorov 4/5 value (Kolmogorov, 1941a). The deviation from the 4/5 law could be explained by insufficient averaging time or shortness of the inertial range. Weak magnetic fields, N_0=1.5 and N_0=4.9, alter the Kolmogorov inertial range, overturning the 4/5 law, while the small scales values of $-S_{u,3}^{(L)}$ remain intact.

At strong magnetic fields, $N_0 \geq 127$ (Figure 3.26 (b)), the third order structure function change sign to positive. At these values of N_0, the turbulence is quasi-2D with enstrophy cascade in the normal plane. Thus, $S_{u,3}^{(L)}$ is normalized by $r^3\eta_\perp$. At $rk_{diss}<10$, $S_{u,3}^{(L)} / r^3\eta_\perp$ is constant, equal to 0.127 and 0.09, for $N_0 = 127$ and $N_0 = 254$, respectively. These values are consistent with the +1/8 law of the normalized third order structure function in the direct enstrophy cascade range (Bernard, 1999; Lindborg, 1999). At $rk_{diss}>20$, the logarithmic correction to the r^3 scaling is obtained, i.e., $S_{u,3}^{(L)} = (a - b\ln(r \cdot k_{diss}))(r^3\eta_\perp)$ with $a \approx 0.42$, $b \approx 0.104$ for $N_0 = 127$, and $a \approx 0.346$, $b \approx 0.092$ for $N_0 = 254$.

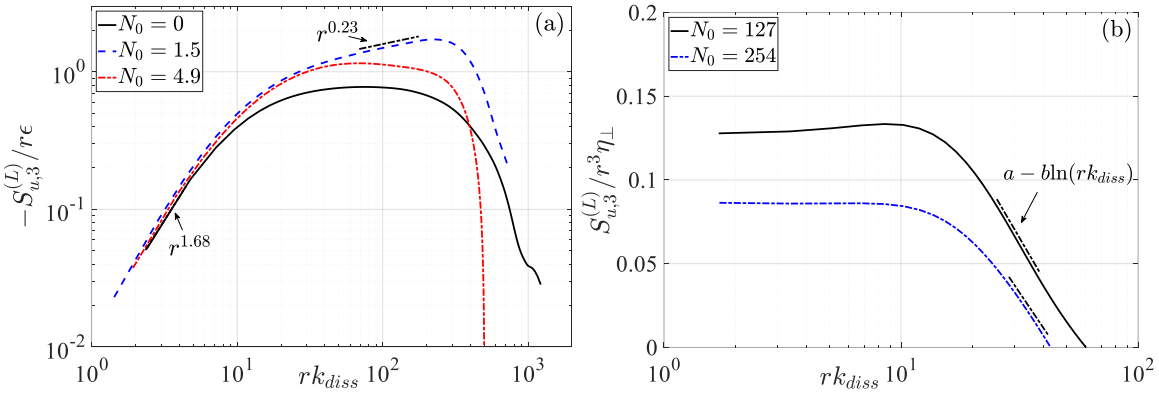

Figure 3.26. Compensated third order longitudinal structure function for weak (a) and strong (b) magnetic field.

Chapter 4

Conclusions

External body forces render turbulence anisotropic, strongly modifying its properties. QS-MHD is considered a useful means to study anisotropization of turbulent flows by external body forces. Laboratory experiments with electro-conductive liquids in the presence of a magnetic field provide important information on this phenomenon: By changing the magnetic field induction, the process of turbulence anisotropization, and hence modification of the energy spectra and turbulent transport, can be investigated in detail in easily controlled experiments. However, laboratory MHD experiments have a severe limitation in that highly conductive fluids, like liquid metals, are needed to reach large interaction parameter values. Liquid metals are not transparent, which makes it virtually impossible to collect complete data on the velocity field. Thus, the only means to comprehensively investigate turbulence anisotropization under the impact of a magnetic field remain high-resolution DNS and analytical theories.

Anisotropy induced by external forces substantially complicates the analytical investigation of turbulent flows. It is, however, possible to apply the QNSE theory to study turbulence anisotropization by solid body rotation (Sukoriansky and Galperin, 2016), stable stratification (Sukoriansky *et al.,* 2005), or Joule friction (Sukoriansky and Zemach, 2016). One of the goals of this study was to compare the results of the QNSE theory with DNS data and to determine at which magnetic fields it is valid.

We studied QS-MHD turbulence by performing high-resolution DNS with a resolution of up to 1024^3 grid points. The interaction parameter was varied in a wide range from $N_0=0$ to $N_0=806$ to study the effect of the magnetic field strength on the turbulence properties in the steady state. Due to anisotropy, the properties of different flow components and in different space directions were investigated.

The results of QNSE analyses of QS-MHD turbulence were compared with those obtained by DNS. The theory derived for small values of the interaction parameter predicts that -7/3 power spectra develop in the lower band of wavenumbers, while at larger k, for which the local interaction parameter $N(k) << 1$ the spectra return to the Kolmogorov -5/3 form. The -7/3 range expands to higher wavenumbers as the strength of the magnetic field increases. The transitional wavenumber k_{tr} that separates these two domains is located in the region where $N(k) \approx 1$. Both spectral laws are seen in the 1024^3 DNS with $N_0 \approx 1.5$, but the proximity of the -5/3 range to the dissipation range at this resolution makes it impossible to clearly show the transition. Much higher resolution is needed for this purpose; a resolution that allows about one decade for each of the power laws. Our simulations indicate that the intermediate range will also take close to one decade. Three decades of inertial range, undisturbed by viscous dissipation and spectral de-aliasing, is currently inaccessible to us. Thus, Kraichnan's two-parametric eddy viscosity, (TPEV) $\nu(k|k_c)$, was employed to extend the Kolmogorov inertial range while still running on 1024^3 grid. Both spectral powers with theoretically predicted spectral amplitudes and the transitional wavenumber were clearly observed in the runs with TPEV.

The theoretically derived TPEV emulates the dynamic effects of small-scale (sub-grid) turbulence on resolvable scales without distorting the downscale energy

cascade. Utilizing TPEV allows an extension of the inertial range up to the largest resolvable wavenumber k_c. With our maximal resolution of 1024^3 grid points, k_c = 483. As far as we know, this is the first practical implementation of Kraichnan's idea. On $1K^3$ grid points, using TPEV, one can get results that otherwise need a DNS with more than $16K^3$ grid points. The TPEV was developed for isotropic turbulence, which does not hold for QS-MHD turbulence where the magnetic field induces anisotropy through the Lorentz force. However, the characteristic frequency of this action is scale-independent, while the characteristic frequency of turbulent scales increases with k (for a spectrum shallower than k^{-3}). Thus, the local interaction parameter $N(k)$ decreases with k. In simulations with N_0=2.2, which is the strongest field where we used TPEV, $N(k_c)$=0.058. This implies that sub-grid scales (SGS) are only weakly affected by the field (see also Ishida and Kaneda (2007)). We did not use TPEV in simulations with $N_0 > 2.2$ exactly because we want to keep SGS isotropic. We conducted a short study of "return to isotropy" on scales with small $N(k)$ and found that 1D energy spectra of all velocity components were almost identical on scales whose interaction parameter $N(k)<0.07$ (see Figure 4.1).

The -7/3 power law corresponds to the lowest order correction to the Kolmogorov spectrum (Sukoriansky and Zemach, 2016). The amplitude of this correction is proportional to τ_J^{-1}. Agreement remains good at values of the interaction parameter higher than those for which the theory was developed. With further increases of the magnetic field, the accuracy of the analytical spectra deteriorates, indicating that higher order terms must be accounted for. Dimensional analysis suggests that if τ_J^{-1} remains the governing parameter, the second-order correction would be proportional to $\tau_J^{-2}k^{-3}$. The actual picture is, however, more complicated and informative. Both directional and componential anisotropization

grow with the increasing strength of the magnetic field. At large values of the interaction parameter, the spectra of different velocity components and in different directions become drastically different. Turbulent fluctuations in the direction of the magnetic field are suppressed by the field, whereas turbulent characteristics in the normal plane become independent of the field.

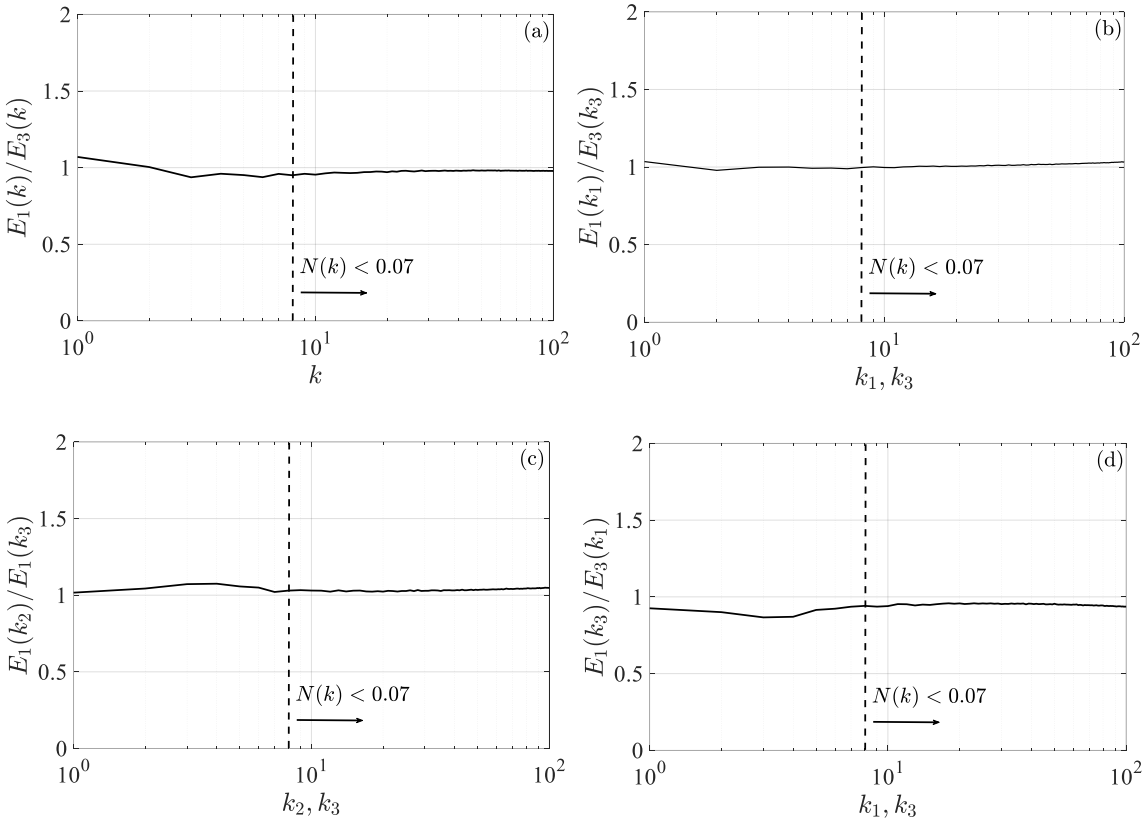

Figure 4.1. Normalized 3D (a) and 1D (b)-(d) energy spectra at small interaction parameter.

Under these conditions, only the 2D energy spectra of the velocity components normal to B and the velocity components parallel to B, $E_\perp(k_\perp)$ and $E_\parallel(k_\perp)$, provide meaningful characterization of the velocity field. Simulations with large N_0 and constant R_0 show that in a strong field, $E_\perp(k_\perp)$ has the form (3.10), which is identical to the 2D enstrophy cascade spectrum. The enstrophy cascade rate $\eta_\perp$ is nearly

constant in the range of wavenumbers between the forcing and dissipation ranges and does not change with increasing N_0. Concurrently, $E_{\parallel}(k_{\perp})$ attains the exact form of a 2D passive scalar spectrum in the inertial-convective range (3.12) with a constant rate of the scalar dissipation $\varepsilon_{\parallel}$. The dimensionless constants in both spectra were found to be close to those obtained in the DNS of 2D turbulence. It, therefore, appears that the QS-MHD turbulence becomes 2D-3C at these values of the interaction parameter. The final state is independent of B, as expected of 2D turbulence in the normal plane since the Lorentz force acting on the flow becomes potential.

With increasing R_0 at constant N_0 the enstrophy cascade becomes unstable and is replaced by helicity cascade with the -7/3 power energy spectrum. The enstrophy cascade is restored with an increase of N_0. It is reasonable to assume that 2D-3C state will become unstable if R_0 is increased beyond the values pertinent to the helicity cascade, the -5/3 energy cascade range will develop on scales with $N(k)<1$, while the energy flux from component u_3 being redistributed between all 3 component. DNS with resolution much higher than 1024^3 available to us is needed to verify this hypothesis.

The final 2D-3C state was also obtained by Favier *et al.* (2010) and Reddy and Verma (2014). However, the exponential behavior of the 3D energy spectrum at large N_0 obtained by Reddy and Verma (2014) differs from the 3D spectrum obtained in our simulations. The differences could be due either to the low 256^3 resolution in their simulations or to the different type of forcing used by them (Reddy and Verma, 2014). Our simulations show that at large N_0 Joule dissipation acts only on the scales of energy injection (if the forcing is 3D), and angular energy transfer degenerates.

Degeneration of the angular transfer at large N_0 was also reported by Reddy *et al.* (2014).

Next, we examined the source of energy supplied to the parallel velocity component. In 3D flows, the pressure causes a redistribution of the energy between the components. With the collapse of velocity derivatives in the direction of the magnetic field, the flow becomes incompressible in the normal plane, and the pressure energy flux to u_3 degenerates. The direct supply of energy by an external 3D force remains the only source of $\varepsilon_{\parallel}$, as was confirmed by simulations with 3D-3C, 3D-2C, and 2D-2C forcing.

Finally, physical space properties, that shed additional light on the turbulence anisotropization, were investigated. The skewness of the longitudinal velocity derivative for the perpendicular (S^u_{kc},S^u_{1c}) and parallel (S^w_{kc},S^w_{1c}) components, and the second and third-order longitudinal velocity structure functions $S^{(L)}_{u,2}$ and $S^{(L)}_{u,3}$ were computed and used to analyze the turbulence characteristics. The skewness S^u_{kc} and S^u_{1c} decrease with increasing magnetic field, approaching zero at the strongest field, in agreement with 2D dynamics. In the non-magnetic case, the p^{th} order structure function $S^{(L)}_{u,p}$ (for p=2,3) scales as $(\varepsilon r)^{p/3}$. Anisotropy, induced by magnetic fields, modifies this scaling. At strong fields, $N_0 \geq 127$, $S^{(L)}_{u,p}$ scales as $(r^3\eta_{\perp})^{p/3}$. Our DNSs results show that at large separations, $S^{(L)}_{u,2}$, and $S^{(L)}_{u,3}$ have logarithmic correction, predicted by Lindborg (1999). The third order structure function agrees with the +1/8 law of the enstrophy cascade, as reported by Lindborg (1999) and Bernard (1999).

References

Alemany, A., Moreau, R., Sulem, P. L. and Frisch, U. 1979 Influence of an external magnetic field on homogeneous MHD turbulence. *J. Méc.* 18 (2), 277-313.

Barami, E., Mikhailovich, B., Shukrun, T., Sukoriansky, S. and Zemach, E. 2017 Heat transfer enhancement in liquid metal by rotating magnetic field. *Magnetohydrodynamics (0024-998X)* 53 (1).

Batchelor, G. K., 1969 Computation of the energy spectrum in homogeneous two-dimensional turbulence. *Phys. Fluids* 12 (12), II-233.

Batchelor, G. K. and Townsend, A. A. 1947 Decay of vorticity in isotropic turbulence. *Proceedings of the Royal Society of London.Series A.Mathematical and Physical Sciences* 190 (1023), 534-550.

Bernard, D., 1999 Three-point velocity correlation functions in two-dimensional forced turbulence. *Physical Review E* 60 (5), 6184.

Blumenau, L., Branover, H., El-Boher, A., Spero, E., Sukoriansky, S., Talmage, G. and Greenspan, E. 1986 Liquid metal MHD energy conversion in fusion reactors. *Fusion Technol* 10 (3P2A), 914-921.

Boffetta, G. and Ecke, R. E. 2012 Two-dimensional turbulence. *Annu. Rev. Fluid Mech.* 44, 427-451.

Bourgoin, M., Marié, L., Pétrélis, F., Gasquet, C., Guigon, A., Luciani, J., Moulin, M., Namer, F., Burguete, J. and Chiffaudel, A. 2002 Magnetohydrodynamics measurements in the von Kármán sodium experiment. *Phys. Fluids* 14 (9), 3046-3058.

Branover, H., 1978 *Magnetohydrodynamic Flow in Ducts*. New York: Wiley.

Branover, H., Eidelman, A., Nagorny, M. and Kireev, M. 1994 Magnetohydrodynamic simulation of quasi-two-dimensional geophysical turbulence. *Progress in Turbulence Research (ed. H. Branover & Y. Unger)* 162, 64.

Branover, H. and Gershon, P. 1979 Experimental investigation of the origin of residual disturbances in turbulent MHD flows after laminarization. *J. Fluid Mech.* 94 (4), 629-647.

Branover, H., Sukorianksy, S., Talmage, G. and Greenspan, E. 1986 Turbulence and the feasibility of self-cooled liquid metal blankets for fusion reactors. *Fusion Technol* 10 (3P2A), 822-829.

Burattini, P., Kinet, M., Carati, D. and Knaepen, B. 2008a Anisotropy of velocity spectra in quasistatic magnetohydrodynamic turbulence. *Phys. Fluids* 20 (6), 065110.

Burattini, P., Kinet, M., Carati, D. and Knaepen, B. 2008b Spectral energetics of quasi-static MHD turbulence. *Physica D* 237 (14-17), 2062-2066.

Cambon, C., 1993 Homogeneous MHD turbulence at weak magnetic Reynolds numbers: approach to angular-dependent spectra. *Prog. Astronaut. Aeronaut.* 149 (AIAA), 131.

Cambon, C. and Godeferd, F. S. 1994 Inertial transfers in freely decaying, rotating, stably stratified, and magnetohydrodynamic turbulence. *Prog. Astronaut. Aeronaut.* 162 (AIAA), 150-168.

Canuto, V. M. and Dubovikov, M. S. 1996 A dynamical model for turbulence. I. General formalism. *Phys. Fluids* 8 (2), 571-586.

Caperan, P. and Alemany, A. 1985 Turbulence homogène MHD à faible nombre de Reynolds magnétique. Etude de la transition vers la phase quasi bidimensionnelle et caractérisation de son anisotropie. *J. Méc. Théor. Appl.* 4 (2), 175-200.

Chekhlov, A., Orszag, S. A., Sukoriansky, S., Galperin, B. and Staroselsky, I. 1996 The effect of small-scale forcing on large-scale structures in two-dimensional flows. *Physica D* 98 (2-4), 321-334.

Chekhlov, A., Orszag, S. A., Sukoriansky, S., Galperin, B. and Staroselsky, I. 1994 Direct numerical simulation tests of eddy viscosity in two dimensions. *Phys. Fluids* 6 (7), 2548-2550.

Claessens, M., 2020 *ITER: The Giant Fusion Reactor* Springer.

Dannevik, W. P., Yakhot, V. and Orszag, S. A. 1987 Analytical theories of turbulence and the ε expansion. *Phys. Fluids* 30 (7), 2021-2029.

Davidson, P. A., 2002 *An Introduction to Magnetohydrodynamics*. Cambridge: Cambridge University Press.

Dold, P. and Benz, K. W. 1999 Rotating magnetic fields: fluid flow and crystal growth applications. *Progress in Crystal Growth and Characterization of Materials* 38 (1-4), 39-58.

Donzis, D. A. and Sreenivasan, K. R. 2010 The bottleneck effect and the Kolmogorov constant in isotropic turbulence. *J. Fluid Mech.* 657, 171-188.

Eswaran, V. and Pope, S. B. 1988 An examination of forcing in direct numerical simulations of turbulence. *Comput. Fluids* 16 (3), 257-278.

Falkovich, G., 1994 Bottleneck phenomenon in developed turbulence. *Phys. Fluids* 6 (4), 1411-1414.

Favier, B. F. N., Godeferd, F. S., Cambon, C. and Delache, A. 2010 On the two-dimensionalization of quasistatic magnetohydrodynamic turbulence. *Phys. Fluids* 22 (7), 075104.

Favier, B. F. N., Godeferd, F. S., Cambon, C., Delache, A. and Bos, W. J. 2011 Quasi-static magnetohydrodynamic turbulence at high Reynolds number. *J. Fluid Mech.* 681, 434-461.

Fox-Kemper, B., Bachman, S., Pearson, B. and Reckinger, S. 2014 Principles and advances in subgrid modelling for eddy-rich simulations. *Clivar Exchanges* 19 (2), 42-46.

Frigo, M. and Johnson, S. G. 2005 The design and implementation of FFTW3. *Proc IEEE* 93 (2), 216-231.

Frisch, U., 1995 *Turbulence: The Legacy of AN Kolmogorov* Cambridge university press.

Frisch, U., Kurien, S., Pandit, R., Pauls, W., Ray, S. S., Wirth, A. and Zhu, J. 2008 Hyperviscosity, Galerkin truncation, and bottlenecks in turbulence. *Phys. Rev. Lett.* 101 (14), 144501.

Galperin, B. and Sukoriansky, S. 2020 Quasinormal scale elimination theory of the anisotropic energy spectra of atmospheric and oceanic turbulence. *Phys. Rev. Fluids* 5 (6), 063803.

Garg, S. and Warhaft, Z. 1998 On the small scale structure of simple shear flow. *Phys. Fluids* 10 (3), 662-673.

Gill, S., 1951 A process for the step-by-step integration of differential equations in an automatic digital computing machine. (1), 96-108.

Golbraikh, E., Chkhetiani, O. G. and Moiseev, S. S. 1998 The role of helicity in turbulent MHD flows. *Journal of Experimental and Theoretical Physics* 87 (1), 95-100.

Gotoh, T., 1998 Energy spectrum in the inertial and dissipation ranges of two-dimensional steady turbulence. *Phys. Rev. E* 57 (3), 2984.

Gotoh, T., 1989 Passive scalar diffusion in two dimensional turbulence in the Lagrangian renormalized approximation. *J. Phys. Soc. Japan* 58 (7), 2365-2379.

Gotoh, T., Fukayama, D. and Nakano, T. 2002 Velocity field statistics in homogeneous steady turbulence obtained using a high-resolution direct numerical simulation. *Phys. Fluids* 14 (3), 1065-1081.

Hunt, J., 1992 *Rapid Distortion Theory. Lecture Notes for the ERCOFTAC Summer School*. Cambridge: Cambridge University Press.

Ishida, T. and Kaneda, Y. 2007 Small-scale anisotropy in magnetohydrodynamic turbulence under a strong uniform magnetic field. *Phys. Fluids* 19 (7), 075104.

Kaneda, Y., 1987 Inertial range of two-dimensional turbulence in a Lagrangian renormalized approximation. *Phys. Fluids* 30 (9), 2672-2675.

Kit, L. G. and Tsinober, A. B. 1971 Possibility of generating and investigating two-dimensional turbulence in a strong magnetic field (Two dimensional MHD turbulent flow generation in strong magnetic field). *Magn. Girodin.* 7, 27-34.

Knaepen, B. and Moreau, R. 2008 Magnetohydrodynamic turbulence at low magnetic Reynolds number. *Annu. Rev. Fluid Mech.* 40, 25-45.

Kolesnikov, Y. B. and Tsinober, A. B. 1974 Experimental investigation of two-dimensional turbulence behind a grid. *Fluid Dyn.* 9 (4), 621-624.

Kolesnikov, Y. B. and Tsinober, A. B. 1972 Two-dimensional turbulent flow behind a circular cylinder. *Magn. Girodin.* 3, 23.

Kolmogorov, A. N., 1941a Dissipation of energy in local isotropic turbulence. *Dokl. Akad. Nauk SSSR* 32, 19-21; (see also *Proc. R. Soc. Lond. A* (1991), 434, 15-17).

Kolmogorov, A. N., 1941b The local structure of turbulence in incompressible viscous fluid for very large Reynolds numbers. *Dokl. Akad. Nauk SSSR* 30, 301–305; (see also *Proc. R. Soc. Lond. A* (1991), 434, 9-13).

Kraichnan, R. H., 1976 Eddy viscosity in two and three dimensions. *J. Atmos. Sci.* 33 (8), 1521-1536.

Kraichnan, R. H., 1971 Inertial-range transfer in two-and three-dimensional turbulence. *J. Fluid Mech.* 47 (3), 525-535.

Kraichnan, R. H., 1967 Inertial ranges in two-dimensional turbulence. *Phys. Fluids* 10 (7), 1417-1423.

Lesieur, M. and Herring, J. 1985 Diffusion of a passive scalar in two-dimensional turbulence. *J. Fluid Mech.* 161, 77-95.

Lindborg, E., 1999 Can the atmospheric kinetic energy spectrum be explained by two-dimensional turbulence? *J. Fluid Mech.* 388, 259-288.

McComb, W. D., 2014 *Homogeneous, Isotropic Turbulence: Phenomenology, Renormalization and Statistical Closures*. Oxford: Oxford University Press.

McComb, W. D., 1995 Theory of turbulence. *Rep. Prog. Phys.* 58 (10), 1117-1205.

McComb, W. D., 1990 *The Physics of Fluid Turbulence*. Oxford: Oxford University Press.

Montgomery, D. and Turner, L. 1982 Two-and-a-half-dimensional magnetohydrodynamic turbulence. *Phys. Fluids* 25 (2), 345-349.

Moreau, R. and Alemany, A. 1976 MHD Flows and Turbulence. *Proc. Bat-Sheva Intern. Seminar* , 49.

Ni, R. and Xia, K. 2013 Kolmogorov constants for the second-order structure function and the energy spectrum. *Physical Review E* 87 (2), 023002.

Orszag, S. A., 1977 Lectures on the statistical theory of turbulence. *Proc.of the 1973 Les Houches Summer School of Theoretical Physics, R.Balian & JL Peube, ed.Gordon and Breach* , 237-374.

Patterson, G. S. and Orszag, S. A. 1971 Spectral calculations of isotropic turbulence: Efficient removal of aliasing interactions. *Phys. Fluids* 14 (11), 2538-2541.

REDDY, K.S., 2015 *Anisotropic energy spectrum, flux and transfers in quasi-static magnetohydrodynamic turbulence,* Ph.D. Thesis IIT Kanpur.

Reddy, K. S., Kumar, R. and Verma, M. K. 2014 Anisotropic energy transfers in quasi-static magnetohydrodynamic turbulence. *Phys. Plasmas* 21 (10), 102310.

Reddy, K. S. and Verma, M. K. 2014 Strong anisotropy in quasi-static magnetohydrodynamic turbulence for high interaction parameters. *Phys. Fluids* 26 (2), 025109.

Roberts, P. H., 1967 *An Introduction to Magnetohydrodynamics*. London: Longmans.

Rogallo, R. S., 1981 *Numerical Experiments in Homogeneous Turbulence* NASA.

Saddoughi, S. G. and Veeravalli, S. V. 1994 Local isotropy in turbulent boundary layers at high Reynolds number. *J. Fluid Mech.* 268, 333-372.

Sagaut, P. and Cambon, C., 2008 *Homogeneous Turbulence Dynamics*. Cambridge: Cambridge University Press.

Shen, X. and Warhaft, Z. 2000 The anisotropy of the small scale structure in high Reynolds number (R $\lambda \sim$ 1000) turbulent shear flow. *Phys. Fluids* 12 (11), 2976-2989.

Sommeria, J., 1986 Experimental study of the two-dimensional inverse energy cascade in a square box. *J. Fluid Mech.* 170, 139-168.

Sommeria, J. and Moreau, R. 1982 Why, how, and when, MHD turbulence becomes two-dimensional. *J. Fluid Mech.* 118 (1), 507-518.

Sreenivasan, K. R., 1995 On the universality of the Kolmogorov constant. *Phys. Fluids* 7 (11), 2778-2784.

Sukoriansky, S. and Branover, H. 1985 Modification of Turbulence Structure and Transfer Properties in Electroconductive Fluids under Influence of Magnetic Fields. *5th Symposium on Turbulent Shear Flows*.

Sukoriansky, S. and Galperin, B. 2016 QNSE theory of turbulence anisotropization and onset of the inverse energy cascade by solid body rotation. *J. Fluid Mech.* 805, 384-421.

Sukoriansky, S., Galperin, B. and Staroselsky, I. 2005 A quasinormal scale elimination model of turbulent flows with stable stratification. *Phys. Fluids* 17 (8), 085107.

Sukoriansky, S., Galperin, B. and Staroselsky, I. 2003 Cross-term and ε-expansion in RNG theory of turbulence. *Fluid Dyn. Res.* 33 (4), 319.

Sukoriansky, S., Kit, E., Zemach, E., Midya, S. and Fernando, H. 2018 Inertial range skewness of the longitudinal velocity derivative in locally isotropic turbulence. *Physical Review Fluids* 3 (11), 114605.

Sukoriansky, S., Klaiman, D., Branover, H. and Greenspan, E. 1989 MHD enhancement of heat transfer and its relevance to fusion reactor blanket design. *Fusion Eng. Des.* 8, 277-282.

Sukoriansky, S. and Zemach, E. 2016 Theoretical study of anisotropic MHD turbulence with low magnetic Reynolds number. *Phys. Scripta* 91 (3), 034001.

Sukoriansky, S., Zilberman, I. and Branover, H. 1986 Experimental studies of turbulence in mercury flows with transverse magnetic fields. *Exp. Fluids* 4 (1), 11-16.

Votsish, A. D. and Kolesnikov, Y. B. 1976 Investigation of transition from three-dimensional turbulence to two-dimensional under a magnetic field. *Magn. Girodin.* 3, 141-142.

Yakhot, V. and Orszag, S. A. 1986 Renormalization group analysis of turbulence. I. Basic theory. *J. Sci. Comput.* 1 (1), 3-51.

Yeung, P. K. and Zhou, Y. 1997 Universality of the Kolmogorov constant in numerical simulations of turbulence. *Physical Review E* 56 (2), 1746.

Zikanov, O., Krasnov, D., Boeck, T. and Sukoriansky, S. 2019 Decay of turbulence in a liquid metal duct flow with transverse magnetic field. *J. Fluid Mech.* 867, 661-690.

Zikanov, O. and Thess, A. 1998 Direct numerical simulation of forced MHD turbulence at low magnetic Reynolds number. *J. Fluid Mech.* 358, 299-333.

תקציר

זרימות מגנטו-הידרודינמיות של מתכות נוזליות נמצאות בשימוש ביישומים תעשייתיים רבים. בדרך כלל, במערכות כאלו, שדה מגנטי חיצוני חזק משפיע על הזרימה, משנה את מאפייני הטורבולנציה, וגורם לזרימה אנאיזוטרופית. זרימות מסוג זה אינן רק חיוניות ליישומים הנדסיים שונים, אלא גם מהוות מסגרת אטרקטיבית למחקרים של טורבולנציה מעין דו-ממדית עם מאפייני מעבר שעברו שינויים מהותיים.

למרות שנושא זה נחקר בהרחבה במשך יותר מחצי מאה, הבנה התופעה רחוקה מלהסתיים. לאחרונה, פותח תיאור חדשני לטורבולנציה מגנטו-הידרודינמית (MHD) מעין סטטית (quasi-static) על ידי יישום של התיאוריה "quasi normal scale elimination (QNSE)", לאזור בו פרמטרי האינטראקציה נמוכים (Sukoriansky and Zemach, 2016).

בעבודה זו, חקרנו אנאיזוטרופיזציה של טורבולנציה מגנטו-הידרודינמית הומוגנית במספרי ריינולדס מגנטים נמוכים בעזרת חישובים נומריים ישירים direct numerical simulations (DNS) ברזולוציה גבוהה עם עד 1024^3 נקודות רשת, כאשר הכוח המאלץ מוכנס בסקאלות הגדולות. תוצאות חישובי ה-DNS הושוו לאלו שהתקבלו מתיאוריית ה-QNSE. הסימולציות אימתו את התחזיות התיאורטיות לשדה מגנטי חלש, כולל יצירת טווח של $k^{-7/3}$ בספקטרום האנרגיה וההתפשטות של אזור זה למספרי גל (k) גבוהים יותר עם הגדלת עוצמת השדה המגנטי.

בשדה מגנטי חזק, הטורבולנציה מגיעה למצב מעין דו-ממדי עם קסקדת אנסטרופיה בטווח האינרציאלי לרכיבי הזרימה הניצבים במישור הניצב, ולסקלר פאסיבי בטווח האינרציאלי-קונבקטיבי לרכיב הזרימה המקביל. ספקטרומי האנרגיה האלו תואמים בצורה טובה את התחזיות התיאורטיות של Kraichnan כולל התיקון הלוגריתמי ל- k^{-3} ו-k^{-1}. יתר על כן, ניתוח של הסקיונס האורכי לנגזרות המהירות ושל פונקציות המבנה האורכיות מסדר שני ומסדר שלישי לרכיבי המהירות הניצבים לשדה המגנטי מצביעות שהטורבולנציה מגיעה למצב מעין דו-ממדי.

עם הגדלת מספר ריינולדס בשדה מגנטי קבוע, קסקדת האנסטרופיה הופכת ללא יציבה ומוחלפת בקסקדה של אליסיטי עם ספקטרום אנרגיה של $k^{-7/3}$. קסקדת האנסטרופיה משוחזרת עם העלאת עוצמת השדה המגנטי.

חקירה של מנגנון הכנסת האנרגיה לרכיב המקביל בשדה מגנטי חזק מעלה שהאנרגיה מסופקת ישירות על ידי הכוח החיצוני. הספקטרום של הרכיב המקביל תלוי באיזוטרופיות הכוח החיצוני, ולכן הוא אינו אוניברסלי.

העבודה נעשתה בהדרכת

פרופ' סמיון סוקוריאנסקי, ד"ר יורי פלדמן וד"ר אפי צמח

במחלקה להנדסת מכונות

בפקולטה להנדסה

אוניברסיטת בן גוריון בנגב
הפקולטה למדעי ההנדסה
המחלקה להנדסת מכונות

אנאיזוטרופיזציה של טורבולנציה מגנטוהידרודינמית מעין סטטית תחת הפעולה של שדה מגנטי סטטי

מחקר לשם מילוי חלקי של הדרישות לקבלת תואר **"דוקטור לפילוסופיה"**

מאת

אלי בראמי

הוגש לסינאט אוניברסיטת בן גוריון בנגב

אישור המנחים: _____

אישור דיקן בית הספר ללימודי מחקר מתקדמים ע"ש קרייטמן: _____

אוקטובר 2021

אוניברסיטת בן גוריון בנגב
הפקולטה למדעי ההנדסה
המחלקה להנדסת מכונות

אנאיזוטרופיזציה של טורבולנציה מגנטוהידרודינמית מעין סטטית תחת הפעולה של שדה מגנטי סטטי

מחקר לשם מילוי חלקי של הדרישות לקבלת תואר "**דוקטור לפילוסופיה**"

מאת

אלי בראמי

הוגש לסינאט אוניברסיטת בן גוריון בנגב

אוקטובר 2021